MODELING OF COUPLED NONLINEAR SHEAR AND FLEXURAL RESPONSES IN MEDIUM-RISE RC WALLS

by

Burak Horoz

B.S., Civil Engineering, Boğaziçi University, 2012

Submitted to the Institute for Graduate Studies in
Science and Engineering in partial fulfillment of
the requirements for the degree of
Master of Science

Graduate Program in Civil Engineering
Boğaziçi University

2015

MODELING OF COUPLED NONLINEAR SHEAR AND FLEXURAL RESPONSES IN MEDIUM-RISE RC WALLS

APPROVED BY:

Assoc. Prof. Kutay Orakçal .....
(Thesis Supervisor)

Assoc. Prof. Serdar Soyöz .....

Prof. Alper İlki .....

DATE OF APPROVAL: 11.08.2015

To my family,

ACKNOWLEDGEMENTS

This thesis would not have been possible without the support of Associate Prof. Kutay Orakçal. I would like to thank for his precious guidance and help during the preparation of the thesis. I would like to acknowledge his patience and his positive approach during the impasse moments of my studies.

I would like to express my special thanks to my colleague Selahattin Akalp for his support during the preparation of this thesis.

I would also like to express my thanks to my friends M.Fethi Güllü, Burakcan Timuçin, Mustafa Sekman, Simon Karabulut, and Oğuz Şenkardeşler for their help in the preparation of this thesis.

I would also like to thank Thien Tran and John W. Wallace from University of California Los Angeles, and Kristijan Kolozvari from California State University Fullerton for providing the experimental data.

Most of all, I would like to express my special thanks to my parents for their invaluable support and encouragement. I cannot compensate their self-sacrifice, patience, and love.

ABSTRACT

MODELING OF COUPLED NONLINEAR SHEAR AND FLEXURAL RESPONSES IN MEDIUM-RISE RC WALLS

A macroscopic finite element modeling approach was adopted in this study for simulating the in-plane hysteretic lateral load behavior of medium-rise reinforced concrete structural walls with moderate aspect ratios (1.5 and 2), with coupled nonlinear flexural and shear response components. The constitutive formulation of the model is based on a fixed-crack-angle modeling methodology. Improvements were made on the constitutive model formulation, for better representation of the shear-aggregate-interlock effects in concrete,and dowel action on reinforcing bars, constituting the shear stress transfer mechanisms across the cracks. The model formulation was implemented into Matlab and analyses were performed using a drift-controlled nonlinear analysis solution strategy. The model was extensively calibrated for five heavily-instrumented wall specimens with moderate aspect ratios (1.5 and 2), and model predictions were compared with experimentally-measured responses at both global and local response levels. Response comparisons revealed that the model provides reasonably accurate predictions of the lateral load capacity, stiffness degradation, hysteretic shape, ductility, and pinching characteristics of the wall specimens investigated. The model also provides reasonable estimates of the relative contribution of flexural and shear deformations to wall displacements, longitudinal strain profiles and rotations along the base of the wall, and crack orientations. Sensitivity studies were also conducted to evaluate the variation of the analytical results with model parameters. The modeling approach implemented in this study is believed to be a significant improvement towards reliable prediction of the coupled shear-flexural response of reinforced concrete walls under cyclic loading conditions.

ÖZET

DOĞRUSAL OLMAYAN EĞİLME VE KAYMA DAVRANIŞI GÖSTEREN ORTA YÜKSEKLİKLİ DUVARLARIN ANALİTİK MODELLENMESİ

Bu çalışmada orta narinlikteki (boy/en oranı 1.5 ve 2) betonarme perde duvarların çevrimsel yükleme koşullarında, doğrusal olmayan eğilme ve kayma deformasyonlarının etkileşimini kapsayan görece basit bir sonlu elemanlar modelleme yöntemi irdelenmiştir. Modelin çalışma prensibi kapsamında sabit yönlü çatlak modelleme yaklaşımı benimsenmiştir. Çatlak yüzeylerindeki kayma gerilmelerinin aktarımını temsil eden agrega kenetlenmesi ve kama etkisi mekanizmalarını daha iyi yansıtabilmek adına model formülasyonunda geliştirmeler yapılmıştır. Model Matlab yazılım ortamında geliştirilmiş, analizlerde yerdegiştirme kontrollü bir doğrusal olmayan çözüm tekniği uygulanmıştır. Analitik model kapsamlı bir şekilde kalibre edilmiş ve analiz sonuçları, 5 adet orta narinlikteki (boy/en oranı 1.5 ve 2) betonarme perde duvar numunesi için elde edilmiş olan deney sonuçları ile karşılaştırılmıştır. Karşılaştırmalardan gözlemlendiği üzere analitik model; yanal yük kapasitesi, rijitlik azalımı, histeretik eğrilerin şekli, süneklik ve orijin bölgesinde daralma gibi perde duvar davranış özelliklerini yeterli bir yaklaşıklıkla hesaplayabilmektedir. Eğilme ve kayma deformasyonlarının yanal yerdegiştirmelere olan göreceli etkileri, duvar tabanındaki dönme ve birim şekildeğiştirmeler ve çatlak yönleri de analitik model tarafından makul doğruluk düzeylerinde tahmin edilmiştir. Ayrıca, parametrik hassasiyet çalışmaları yürütülmüş ve model parametrelerinin analitik sonuçlara olan etkileri incelenmiştir. Çevrimsel yükleme koşulları altındaki betonarme perde duvarların etkileşim altındaki eğilme ve kayma davranışlarının güvenilir bir şekilde kestirilebilmesi için bu çalışmanın önemli bir aşama olduğu ve gelecek çalışmalara zemin hazırlayacağı düşünülmektedir.

TABLE OF CONTENTS

ACKNOWLEDGEMENTS iv
ABSTRACT v
ÖZET vi
LIST OF FIGURES x
LIST OF TABLES xviii
LIST OF SYMBOLS xix
LIST OF ACRONYMS/ABBREVIATIONS xxiii
1. INTRODUCTION 1
1.1. General 1
1.2. Literature Review 2
1.3. Objectives and Scope 14
1.4. Thesis Outline 15
2. MODEL DESCRIPTION 17
2.1. Overview 17
2.2. Constitutive Panel Model 18
2.3. Constitutive Material Models 21
2.3.1. Constitutive Model for Reinforcement 21
2.3.2. Constitutive Model for Concrete 22
2.3.3. Compression Softening Effect on Concrete 23
2.3.4. Tension Stiffening Effects on Concrete and Reinforcing Steel . . 24
2.3.5. Biaxial Damage Effect on Concrete 24
2.3.6. Constitutive Modeling of the Shear Aggregate Interlock Effect in Concrete 25
2.3.7. Constitutive Modeling of Dowel Action on Reinforcing Bars . . 27
2.4. Finite Element Modeling Methodology 31
2.4.1. 4 Nodes, 8 Degree of Freedom Rectangular Element 31
2.4.2. Finite Element Model Stiffness Assembly 36
2.4.3. Internal Force Vector Assembly 37
2.4.4. Support Conditions and Constraints 40

2.4.5. Nonlinear Analysis Solution Strategy 41
3. ANALYTICAL MODEL RESULTS AND PARAMETRIC SENSITIVITY STUDIES 43
3.1. General 43
3.2. Analytical Model Results 44
3.3. Sensitivity of Model Response to Wall Configurations and Model Parameters 48
3.3.1. Wall Aspect Ratio 48
3.3.2. Reinforcement Ratio 51
3.3.3. Axial Load 53
3.3.4. Shear Resisting Mechanism of RC Panel Model 53
3.3.5. Number of Model Elements 54
3.4. Overview 57
4. EXPERIMENTAL CALIBRATION OF THE MODEL 59
4.1. Description of the Wall Specimens 59
4.2. Test Setup and Instrumentation 62
4.3. Instrumentation and Data Acquisition 64
4.3.1. Total Displacement Calculation 66
4.3.2. Flexural Component of Lateral Displacement Calculation 67
4.3.3. Shear Component of Lateral Displacement Calculation 68
4.4. Material Properties 69
4.5. Calibration of the Model for the Wall Specimens 72
4.5.1. Calibration of Model Element Dimensions and Reinforcement Ratios 72
4.5.2. Calibration of Constitutive Material Parameters 73
4.5.2.1. Calibration of the Constitutive Model for Reinforcing Steel 73
4.5.2.2. Calibration of the Constitutive Model for Concrete . . 76
5. COMPARISON OF ANALYTICAL AND EXPERIMENTAL RESULTS . . 84
5.1. Lateral Load versus Top Displacement Response 84
5.1.1. Lateral Stiffness and Load Capacity 85
5.2. Failure Mechanisms 88

5.3. Shear and Flexural Components of Lateral Displacement 90
5.3.1. Lateral Load versus Flexural Displacement Relations 90
5.3.2. Lateral Load versus Shear Displacement Relations 94
5.4. Wall Vertical Growth 98
5.4.1. Vertical Growth versus Top Lateral Displacement Relations . . 98
5.5. Lateral Displacement Profiles 101
5.5.1. Total Displacement Profiles 101
5.5.2. Flexural Displacement Profiles 104
5.5.3. Shear Displacement Profiles 107
5.5.4. Contributions of Flexural and Shear Components to Top Lateral Displacement 110
5.6. Cracking Patterns 111
5.6.1. Specimen RW-A20-P10-S38 - Test 1 112
5.6.2. Specimen RW-A20-P10-S63 - Test 2 113
5.6.3. Specimen RW-A15-P10-S51 - Test 3 116
5.6.4. Specimen RW-A15-P10-S78 - Test 4 117
5.6.5. Specimen RW-A15-P2.5-S64 - Test 5 118
5.7. Local Responses 120
5.7.1. Vertical Strains 120
5.7.2. Base Rotations 122
5.8. Overview 125
6. SUMMARY AND CONCLUSIONS 127
6.1. Summary 127
6.2. Conclusions 128
6.3. Recommendations for Future Studies 129
REFERENCES 130

LIST OF FIGURES

Figure 1.1. Shear Spring with Shear Limit Curve (Elwood, 2002). 6

Figure 1.2. Multiple-Vertical-Line-Element Model (MVLEM) (Orakcal *et al.*, 2004). 6

Figure 1.3. Flexural Deformations of MVLEM Element (Orakcal *et al.*, 2004). 7

Figure 1.4. Implementation of Shear-Flexure Interaction (Zhang and Xu, 2010). 10

Figure 1.5. RC Wall and Wall Panel Truss Model Panagiotou *et al.*, 2012). . . 11

Figure 1.6. Coupled Compression-Tension Model for Diagonal Truss Elements. 12

Figure 1.7. Coupled Model Element (Massone *et al.*, 2006, 2009). 12

Figure 1.8. Element Models. 14

Figure 2.1. The Uncracked Behavior of Concrete in the Fixed Strut Angle Model (Orakcal *et al.*, 2012). 19

Figure 2.2. The Behavior of Concrete After the Formation of First Crack in the Fixed Strut Angle Model (Orakcal *et al.*, 2012). 20

Figure 2.3. The Behavior of Concrete after the Formation of Second Crack in the Fixed Strut Angle Model (Orakcal *et al.*, 2012). 21

Figure 2.4. The Hysteretic Constitutive Model for Reinforcing Steel (Menegotto and Pinto, 1973). 21

Figure 2.5. The Hysteretic Constitutive Model for Concrete (Chang and Mander, 1994). 22

Figure 2.6. Compression Softening Effects Implemented in the Panel Model (Ulugtekin, 2010). 23

Figure 2.7. a-) Friction Based Constitutive Model for Shear Aggregate Interlock (Orakcal *et al.*, 2012), b-) Shear Friction Mechanism along a Crack in ACI- 318. 26

Figure 2.8. Dowel action of a Reinforcement Bar Crossing a Crack (He and Kwan, 2001). 29

Figure 2.9. Cracked Concrete Elements Containing a Reinforcement Bar Running in the x&y-Directions Crossing the Cracks at Acute Angle. . 30

Figure 2.10. Dowel Action Model. 30

Figure 2.11. a-) Local Nodes and DOFs in a Rectangular Model Element, b-) Normalized Coordinates of a Rectangular Model Element. 32

Figure 2.12. Tangent Stiffness (Elasticity) Matrix Calculation Path. 34

Figure 2.13. a-) Numbering Technique Used for the FEM of a Rectangular Wall, b) Global and Local DOFs for a Wall Model. 37

Figure 2.14. Numbering of Internal Force Terms for a Model Element (Gullu, 2013). 38

Figure 2.15. Representation of the Nonlinear Analysis Solution Strategy for a Single Degree of Freedom System (Clarke and Hancock, 1990). . . 42

Figure 2.16. Iterative Strategy and Residual Displacements (Clarke and Hancock, 1990). 42

Figure 3.1. Lateral load vs. Top Displacement Response Predicted by the Model. 44

Figure 3.2. Load vs. Flexural Top Displacement Response Predicted by the Model. 45

Figure 3.3. Load vs. Shear Top Displacement Response Predicted by the Model. 46

Figure 3.4. Total Displacement Profiles. 47

Figure 3.5. Shear and Flexural Displacement Profiles with Contributions to Total Displacement. 47

Figure 3.6. Vertical Growth versus Lateral Displacement. 48

Figure 3.7. Sensitivity of Predicted Response to Wall Aspect Ratio (h_w/l_w). . 50

Figure 3.8. Contribution of Shear Deformation to Top Displacement, for Different Wall Aspect Ratios. 50

Figure 3.9. Sensitivity of Predicted Flexure Response to Wall Aspect Ratio (h_w/l_w). 51

Figure 3.10. Sensitivity of Predicted Shear Response to Wall Aspect Ratio (h_w/l_w). 51

Figure 3.11. Sensitivity of Predicted Response to Wall Reinforcement. 52

Figure 3.12. Sensitivity of Predicted Response to Axial Load Level. 53

Figure 3.13. Sensitivity of Predicted Response to Shear Aggregate Interlock Parameters. 54

Figure 3.14. Sensitivity of Predicted Response to Number of Model Elements. . 56

Figure 3.15. Vertical Strain Profiles for m=6 - n=9 and m=12 - n=18. 56

Figure 3.16. Vertical Strain Profiles for m=6 - n=9 and m=6 - n=18. 57

Figure 3.17. Vertical Strain Profiles for m=6 - n=9 and m=12 - n=9. 57

Figure 4.1. Typical Wall Cross-Section. 60

Figure 4.2. Wall Boundary Zone Detailing (Tran, 2012). 61

Figure 4.3. Scheme of Test Setup (Tran, 2012). 62

Figure 4.4. Loading Protocols. 63

Figure 4.5. Sensor Configuration for Specimens #1 and #2 (Tran, 2012). . . . 64

Figure 4.6. Sensor Configuration for Specimens #3, #4, and #5 (Tran, 2012). 65

Figure 4.7. Strain Gauge Location in Boundary Transverse Reinforcement. . . 65

Figure 4.8. Strain Gauge Location in Vertical and Horizontal Reinforcement (Tran, 2012). 66

Figure 4.9. Deformation of a Wall Segment (Tran, 2012). 67

Figure 4.10. Calculation of Flexural Deformation for a Wall Section in Experiment (Tran, 2012). 68

Figure 4.11. Deformations of Wall Segment. 68

Figure 4.12. Concrete Cylinder Stress-Strain Relationships for Tests 1 to 5. . . 69

Figure 4.13. Experimental Stress-Strain Relationships for Reinforcement. . . . 71

Figure 4.14. The Stress-Strain Behavior of Bare Rebar and Rebar Embedded in Concrete. 74

Figure 4.15. Stress-Strain Relationship by Belarbi and Hsu (1994) for the Bar in Concrete. 75

Figure 4.16. Compression and Tension Envelope Curves of the Model by Chang and Mander (1994). 78

Figure 4.17. Stress-Strain Curves for Confined and Unconfined Concrete in Compression for Specimen RW-A20-P10-S38. 79

Figure 4.18. Stress-Strain Relationship by Belarbi and Hsu (1994) for Concrete in Tension. 81

Figure 4.19. Stress-Strain Diagrams for Concrete in Tension for RW-A20-P10-S38. 83

Figure 5.1. Lateral Load-Displacement Response of Specimen RW-A20-P10-S38. 86

Figure 5.2. Lateral Load-Displacement Response of Specimen RW-A20-P10-S63. 86

Figure 5.3. Lateral Load-Displacement Response of Specimen RW-A15-P10-S51. 87

Figure 5.4. Lateral Load-Displacement Response of Specimen RW-A15-P10-S78. 87

Figure 5.5. Lateral Load-Displacement Response of Specimen RW-A15-P2.5-S64. 88

Figure 5.6. Load vs. Flexural Displacement for Specimen RW-A20-P10-S38. . 92

Figure 5.7. Load vs. Flexural Displacement for Specimen RW-A20-P10-S63. . 92

Figure 5.8. Load vs. Flexural Displacement for Specimen RW-A15-P10-S51. . 93

Figure 5.9. Load vs. Flexural Displacement for Specimen RW-A15-P10-S78. . 93

Figure 5.10. Load vs. Flexural Displacement for Specimen RW-A15-P2.5-S64. . 94

Figure 5.11. Load vs. Shear Displacement, Specimen RW-A20-P10-S38, Test 1. 95

Figure 5.12. Load vs. Shear Displacement, Specimen RW-A20-P10-S63, Test 2. 96

Figure 5.13. Load vs. Shear Displacement, Specimen RW-A15-P10-S51, Test 3. 96

Figure 5.14. Load vs. Shear Displacement, Specimen RW-A15-P10-S78, Test 4. 97

Figure 5.15. Load vs. Shear Displacement, Specimen RW-A15-P2.5-S64, Test 5. 97

Figure 5.16. Vertical Growth vs. Lateral Displacement for RW-A20-P10-S38. . 99

Figure 5.17. Vertical Growth vs. Lateral Displacement for RW-A20-P10-S63. . 99

Figure 5.18. Vertical growth vs. lateral displacement for RW-A15-P10-S51. . . 100

Figure 5.19. Vertical growth vs. lateral displacement for RW-A15-P10-S78. . . 100

Figure 5.20. Vertical growth vs. lateral displacement for RW-A15-P2.5-S64. . . 101

Figure 5.21. Total Lateral Displacement Profile for Specimen RW-A20-P10-S38. 102

Figure 5.22. Total Lateral Displacement Profile for Specimen RW-A20-P10-S63. 102

Figure 5.23. Total Lateral Displacement Profile for Specimen RW-A15-P10-S51. 103

Figure 5.24. Total Lateral Displacement Profile for Specimen RW-A15-P10-S78. 103

Figure 5.25. Total Lateral Displacement Profile for Specimen RW-A15-P2.5-S64. 104

Figure 5.26. Flexural Displacement Profile for Specimen RW-A20-P10-S38. . . 105

Figure 5.27. Flexural Displacement Profile for Specimen RW-A20-P10-S63. . . 106

Figure 5.28. Flexural Displacement Profile for Specimen RW-A15-P10-S51. . . 106

Figure 5.29. Flexural Displacement Profile for Specimen RW-A15-P10-S78. . . 107

Figure 5.30. Flexural Displacement Profile for Specimen RW-A15-P2.5-S64. . . 107

Figure 5.31. Shear Displacement Profile for Specimen RW-A20-P10-S38. 108

Figure 5.32. Shear Displacement Profile for Specimen RW-A20-P10-S63. 109

Figure 5.33. Shear Displacement Profile for Specimen RW-A15-P10-S51. 109

Figure 5.34. Shear Displacement Profile for Specimen RW-A15-P10-S78. 110

Figure 5.35. Shear Displacement Profile for Specimen RW-A15-P2.5-S64. . . . 110

Figure 5.36. Cracking Patterns for Specimen RW-A20-P10-S38, Test 1. 113

Figure 5.37. Cracking Patterns for Specimen RW-A20-P10-S63, Test 2. 115

Figure 5.38. Cracking Patterns for Specimen RW-A15-P10-S51, Test 3. 117

Figure 5.39. Cracking Patterns for Specimen RW-A15-P10-S78, Test 4. 118

Figure 5.40. Cracking Patterns for Specimen RW-A15-P2.5-S64, Test 5. 119

Figure 5.41. Vertical Strain Profiles for Specimen RW-A20-P10-S63, Test 2. . . 121

Figure 5.42. Vertical Strain Profiles for Specimen RW-A15-P10-S51, Test 3. . . 121

Figure 5.43. Vertical Strain Profiles for Specimen RW-A15-P10-S78, Test 4. . . 122

Figure 5.44. Vertical Strain Profiles for Specimen RW-A15-P2.5-S64, Test 5. . . 122

Figure 5.45. Base Rotations for Specimen RW-A20-P10-S63, Test 2. 123

Figure 5.46. Base Rotations for Specimen RW-A15-P10-S51, Test 3. 124

Figure 5.47. Base Rotations for Specimen RW-A15-P10-S78, Test 4. 124

Figure 5.48. Base Rotations for Specimen RW-A15-P2.5-S64, Test 5. 124

LIST OF TABLES

Table 4.1. Test Specimens Details. 60

Table 4.2. Wall Reinforcement Details. 61

Table 4.3. Average Compressive Strength of Concrete at the Day of Testing (Tran, 2012). 70

Table 4.4. Yield and Ultimate Strengths of Reinforcement. 71

Table 4.5. Wall Model Geometry Details. 73

Table 4.6. Calibrated Values of the Constitutive Parameters of Reinforcing Steel Bars for the Wall Specimens. 77

Table 4.7. Calibrated Values of the Constitutive Parameters for Concrete in Compression. 80

Table 4.8. Calibrated Values of the Constitutive Parameters for Concrete in Tension. 82

Table 5.1. Average Contributions of Flexural and Shear Deformations. 111

LIST OF SYMBOLS

A_g	Gross concrete cross-section area
A_{vf}	Shear friction reinforcing steel bar cross-sectional area
A_s	Sectional area of steel reinforcement bar
B	Tension stiffening parameter for reinforcing steel
b	Steel strain hardening ratio
[B]	Transformation matrix from displacement to deformation
b'	Strain hardening ratio for tension
{D}	Global displacement vector
d_b	Bar diameter
d_i	Local nodal displacement
E_0	Slope of elastic asymptote (Modulus of Elasticity)
E_1	Slope of yield asymptote
E_c	Elastic modulus for concrete
E_p	Plastic (strain hardening) modulus for bare steel bars
E_p*	Plastic (strain hardening) modulus for steel bars embedded in concrete
[E]	Elasticity matrix
f_c'	Peak concrete compressive strength
f_t	Peak concrete tensile stress
f_y	Yield strength of the bare reinforcing steel bars
{f}	Local internal force vector of one mesh
{F}	Global internal force vector
$[F_I]_i$	Reference vector
$\{F_{ext}\}$	External force vector
$\{F_{unb}\}$	Unbalanced force vector
[G]	Strain matrix
h_w	Height of the wall
K	Dowel stiffness of reinforcement bar crossing a crack
[K]	Global stiffness matrix

[k]	Local stiffness matrix of one mesh
$[K_I]_i$	Global tangent stiffness matrix
l_w	Length of the wall
m	Mesh number in horizontal direction
n	Mesh number in vertical direction
N_i	Shape function for finite element model
P_{ax}	Axial load at top level of rectangular wall
P_{lat}	Lateral load
r	Parameter defining shape of monotonic stress-strain curve for concrete
R_0	The value assigned to the parameter R for initial (or monotonic) loading
[T]	Transformation matrix for body constraint
t	Thickness of mesh
u	Generic displacement of mesh in x direction
v	Generic displacement of mesh in y direction
V_d	dowel force developed in reinforcement bar
V_{du}	dowel force developed in reinforcement bar at ultimate state
V_{dx}	dowel force developed in reinforcement bars running in x direction
V_{dy}	dowel force developed in reinforcement bars running in y direction
V_n	Shear force on the crack surface
w	Width of mesh
x_{crn}	Critical strain of concrete in compression
x_{crp}	Critical strain of concrete in tension
ε_0	Strain at the point of intersection of the two asymptotes
ε_1	Principal strain in direction 1
ε_2	Principal strain in direction 2
ε_c'	Strain at peak compressive strain
ε_{cr}	Concrete cracking strain

ε_r	Strain at the point of strain reversal
ε_t	Monotonic strain at peak concrete tensile stress
ε_x	Normal strain in x direction
ε_y	Normal strain in y direction
ε_x'	Arbitrary strain transformed to x' direction
ε_y'	Arbitrary strain transformed to y' direction
γ'_{xy}	Shear strain
ρ_x	Reinforcement ratios in x direction
ρ_y	Reinforcement ratios in y direction
σ_0	Stress at the point of intersection of the two asymptotes
σ_{c1}	Concrete stress in principal direction 1
σ_{c2}	Concrete stress in principal direction 2
σ_{cx}	Concrete normal stress in x direction
σ_{cy}	Concrete normal stress in y direction
σ_{cx}'	Concrete stress in x' direction
σ_{cy}'	Concrete stress in y' direction
σ_r	Stress at the point of strain reversal
σ_x	Normal stress in x direction
σ_y	Normal stress in y direction
τ_{cxy}	Concrete shear stress
τ_{xy}	Shear stress
τ_{12}^d	Dowel shear stress developed across the crack
τ_x^d	Dowel stresses developed by reinforcement bars running in x direction
τ_y^d	Dowel stresses developed by reinforcement bars running in y direction
θ_{cr}	Concrete Crack direction or Fixed Strut Angle
θ_{crA}	Concrete Crack direction A or Fixed Strut Angle A
θ_{crB}	Concrete Crack direction B or Fixed Strut Angle B
μ	Friction coefficient
α	Angle between shear friction reinforcement and shear plane
ζ	Normalized local coordinates of a mesh in x direction

η	Normalized local coordinates of a mesh in y direction
δ	Displacement increment
$\Delta\lambda$	The initial load increment
δ_n	The initial displacement increment
δ_R	Residual displacement increment
ℓ	length of reinforcement bar subjected to significant dowel action
ℓ_x	length of reinforcement bar running in x direction
ℓ_y	length of reinforcement bar running in y direction

LIST OF ACRONYMS/ABBREVIATIONS

ACI	American Concrete Institute
DOF	Degree of freedom
FEM	Finite element model
FSAM	Fixed strut angle model
LVDT	Linear variable differential transducers
MVLEM	Multiple-Vertical-Line-Element Model
RC	Reinforced Concrete
RW	Rectangular wall
SFI	Shear Flexure interaction

1. INTRODUCTION

1.1. General

Reinforced concrete (RC) structural walls provide significant contribution to resisting the earthquake effects on building-type structures. Under service earthquakes, they are expected to provide sufficient stiffness and lateral load capacity to limit the lateral displacement demand on buildings, without significant damage. Under severe (design or maximum considered) earthquake actions, walls are designed and detailed to possess the required ductility characteristics and dissipate hysteretic energy without significant reduction in the lateral load capacity of the structure. Since structural walls are utilized as the main lateral-load-resisting members in numerous building systems, vast amount of research has been conducted to characterize the seismic behavior of structural walls.

Structural walls are typically classified according to their aspect ratios. The behavior of squat structural walls with aspect ratios less than 1.0-1.5 are controlled by shear, whereas slender structural walls with aspect ratios exceeding 2.5-3.0 are predominantly controlled by flexural actions. For structural walls with moderate aspect ratios (between 1.5 and 2.5), both flexural yielding and nonlinear shear deformations (which are usually coupled) contribute to wall behavior. For such walls, nonlinear shear deformations can constitute up to 30% to 50% of lateral wall displacements, as investigated experimentally by Tran and Wallace (2012). Reliable behavioral modeling of such structural walls with predominant shear-flexure interaction behavior is of particular interest, especially because fiber-based modeling methodologies commonly used in practice for performance-based design of buildings typically consider uncoupled shear and flexural response components, which fails to represent the experimentally-observed response characteristics of walls on which shear demands are significant.

So far, the lateral load behavior of structural walls controlled by nonlinear flexural deformations has been investigated both experimentally and analytically by numerous

researchers. However, research focusing on the nonlinear shear behavior and interaction between nonlinear shear and flexural (SFI) responses of walls is relatively sparse. Most of the modeling approaches available in the literature on modeling of such wall behavior incorporate various assumptions and simplifications, and are subject to limitations. There is still a need for a reliable and generalized, yet relatively simple modeling approach that can simulate the coupled flexural and shear responses of walls with various geometries and aspect ratios. Therefore, the primary objective of this study was to provide a robust yet practical modeling approach for representing the nonlinear shear behavior as well as the interaction between nonlinear shear and flexural responses of walls.

Accordingly, the finite element modeling methodology proposed by Gullu (2013) was adopted in this study for simulating the response of medium-rise walls with coupled shear and flexural responses. The behavior of the constitutive panel elements in the finite element model formulation is described by a previously-developed constitutive relationship named as the Fixed-Strut-Angle Model (Ulugtekin, 2010). Improved constitutive models for shear aggregate interlock and dowel action models were implemented in the constitutive model formulation for simulating the transfer of shear stress across cracks. The finite element wall model with the improved constitutive formulation was calibrated for five wall specimens with moderate aspect ratios, where coupled flexural yielding and nonlinear shear deformations were observed, resulting in reduced lateral stiffness, strength and ductility. Model predictions were compared with test results at both global (load-displacement) and local (deformation) response levels. The modeling approach adopted in this study was found to adequately represent the influence of both nonlinear flexural and shear deformations on wall response, as well as their interaction.

1.2. Literature Review

In general sense, analytical modeling approaches for simulating the response of RC walls are classified as micro-modeling and macro-modeling approaches. These approaches incorporate certain advantages and disadvantages of their own, depending on

the objective. Macro-modeling approaches predict significant response characteristics with sufficient accuracy, and at recognizably reduced computational cost. However, this approach is somewhat "posteriori"; i.e., the behavior and failure modes need to be prescribed prior to the analysis, as stated by Vulcano et al. (1988). Although micro-modeling approaches with detailed three-dimensional finite element formulations come with robust and refined local response features, they may become problematic in terms of computational stability, efficiency, and interpretation of the results, especially for complicated wall systems.

The Multiple-Vertical-Line-Element (MVLE) model (Vulcano and Bertero, 1987) is one of the first macro modeling approaches that efficiently provides reasonably accurate hysteretic response predictions for slender walls, the responses of which are controlled by nonlinear flexural deformations. Although shear deformations are not neglected, shear and flexural components of the response are described independently in the model formulation. A predefined shear force vs. deformation relationship is used, and its parameters need to be calibrated in an ad-hoc manner. The original MVLE model was improved by incorporating nonlinear shear behavior by Colotti (1993). The interaction between axial and shear responses in this model were represented by a constitutive membrane (panel) model over a one-story model element. Uniaxial material models were used for modeling the flexural and axial components of the response. More accurate results were attained compared to prior macro-models. However, the predicted relative contributions of the shear and flexural deformations had some discrepancies with the experimental observations. Although the axial and shear responses were coupled in the model formulation, it remained to be incapable of incorporating the interaction between shear and flexural responses. Therefore, it brought unrealistic outcomes, such as the shear behavior being invariant along wall height (Massone and Wallace, 2004).

One of the standing approaches that implies the coupling of axial and shear responses in reinforced concrete panel elements (membranes subjected to uniform in-plane stresses) is the Fixed Angle Softened Truss Model (FA-STM) proposed by Pang and Hsu in 1996. In this model, it was assumed that the direction of the cracks coincides

with the fixed angle following the principal directions of the applied stresses. Consequently, the sliding shear stresses along crack surfaces were calculated by an updated shear modulus. Subsequently, the University of Houston launched a new experimental program to develop a set of reversed cyclic material models. Among 12 cyclic panel tests, three specimens were oriented at 90° angle relative to the testing equipment (the angle represents the orientation of reinforcing bars relative to panel edges), five specimens oriented at 45°, three at 68.2^o and one at 79.8^o. Proportionally-applied reversed cyclic load tests on three 45° panels were used as reference test specimens during the calibration of the model proposed in this study. Thereby a new model, the cyclic extension of FA-STM, was proposed together with new cyclic material relationships both for steel and concrete. (Mansour *et al.*, 2002)

The results of the experimental program were also used to calibrate the Cyclic Softened Membrane Model, which was an extension of the original SMM with cyclic constitutive material relationships implemented for both steel and concrete. However, a damage coefficient, which defines the effect of the compressive strain history in the perpendicular direction to a compressive strut, was also implemented into the model in addition to the cyclic material models (Mansour and Hsu 2005, Hsu and Mansour 2002).

The so-called Disturbed Stress Field Model (DSFM) was proposed by Vecchio in 2000. It was assumed that principal stress and strain directions deviate from each other, and the crack directions coincide with the principal stress direction. On the other hand, principal stress directions rotate relative to (depart from) principal strain directions with a fixed "lag", as a result of which shear strains along cracks are accepted as partially slipped deformations along cracks.

The Softened Membrane Model (SMM) was proposed by Hsu and Zhu in 2002. This model differentiated from the FA-STM only by including the Poisson's effect. Similarly to FA-STM, the influence of the "kinking effect" was regarded not as important as stated previously. Then, Mansour and Hsu proposed a cyclic version of the SMM in 2005, in which 12 panel specimens were tested under reversed cyclic loading

for development of the formulation of the proposed model, as well as for assessment of its prediction capabilities.

The implementation of "microplane" approach is suggested by Bazant *et al.*, in 1996 for constitutive modeling of RC panels. It defines the interaction between axial, transverse, and shear strain fields at the concrete and steel material levels based on basic uniaxial stress-strain relationships for steel and concrete. By observing the uniaxial stress-strain relationships on the microplanes, the structural response was determined. A typical discretization with eight microplanes in a concrete fiber that have the same uniaxial stress-strain relationships, namely isotropy was assumed. Longitudinal reinforcing bars were modeled using steel fibers in the directions of the reinforcement while transverse reinforcement at each cross-section were represented as a tributary reinforcement within the concrete fiber formulation. The stress-strain relationship for steel was idealized as a multilinear curve with a "gradual-softening" to take into account the Bauschinger effect. In modeling of the reinforcing steel, only the axial stresses and strains were considered, whereas dowel action on the reinforcement was neglected.

One approach to coupling flexural and shear responses in RC walls was proposed by Takayanagi *et al.*, (1979), which involves modeling of the shear force-displacement envelope relationship with the same yielding point (yielding force) required to reach flexural yielding. Another indirect approach to coupling flexure and shear responses was proposed by Elwood (2002), which used a limit state model. This model was based on an experimental study of columns exhibiting shear-critical and flexure-critical failures. In this experimental study, two limit states were used, one for the shear force and one for the axial load, both related to the total lateral displacement. As depicted in Figure 1.1, the total response was limited by the shear curve, via reducing the shear force at larger displacements to the shear limit state.

In order to experimentally validate the Multiple-Vertical-Line-Element Model (MVLEM) (Orakcal *et al.*, 2004) for relatively slender structural walls, Orakcal and Wallace (2006) conducted an analytical study. In this study, detailed material characteristics and important behavioral response features such as neutral axis migration,

tension-stiffening, progressive gap closure and nonlinear shear behavior were considered. Two approximately quarter-scale wall specimens, one of which had a rectangular cross section and the other had a T-shaped cross section, tested by Thomsen and Wallace (1995) were used for experimental validation of the model. Direct comparisons between the predicted and the measured flexural responses at various locations on the walls were presented. Overall, it was shown that for rectangular walls, discrepancies in the local compressive strains were observed, and the variation of the longitudinal tensile strains along the flange of T-shaped walls could not be captured by the model.

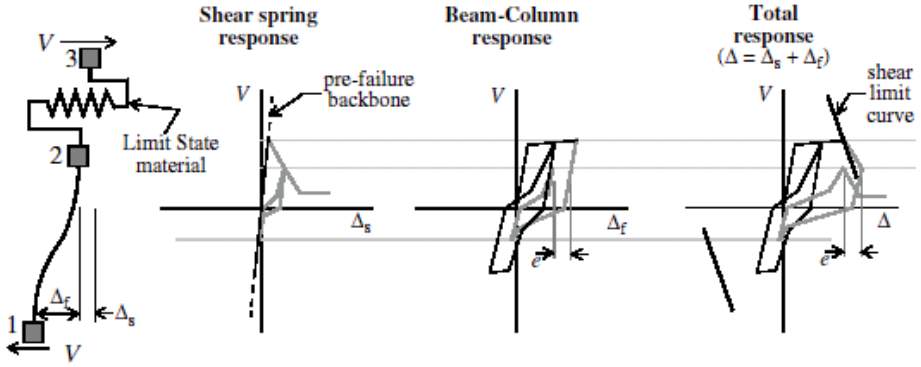

Figure 1.1. Shear Spring with Shear Limit Curve (Elwood, 2002).

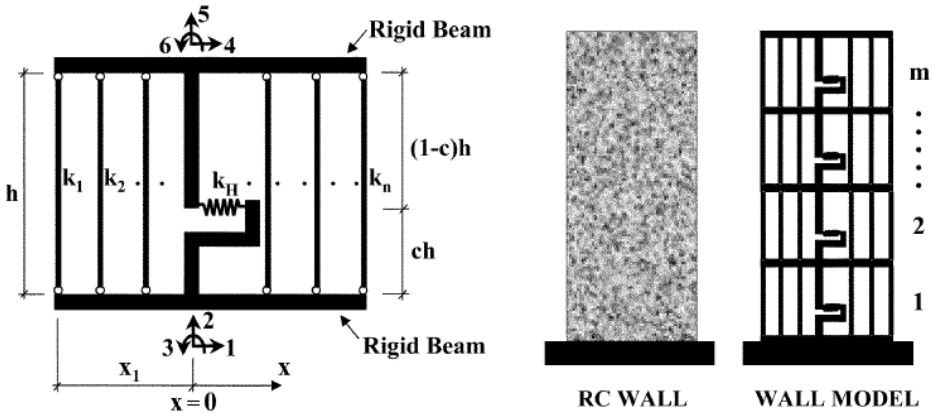

Figure 1.2. Multiple-Vertical-Line-Element Model (MVLEM) (Orakcal *et al.*, 2004).

In a displacement-based fiber model, the curvature profile between two element nodes varies linearly. In the MVLEM, however, a constant profile of the wall curvature along the height for each wall element is assumed, and the relative rotation between top and bottom faces of the wall element are concentrated at a particular point prescribed

for each element, defined as the center of rotation (Figure 1.3). In order to estimate the nonlinear response of slender RC walls, the MVLEM formulation was improved via elaborate hysteretic uniaxial stress-strain material models rather than simplified force-deformation rules (Fischinger *et al.*, 1990). The hysteretic model of Menegotto and Pinto (1973), as extended by Filippou *et al.*, (1983) to incorporate isotropic strain hardening effects, was adopted for the stress-strain model of reinforcing steel. Due to its advantages, such as taking into account the progressive degradation of stiffness of the unloading and reloading curves for increasing values of strain, the effects of confinement, tension stiffening and gradual crack closure, the Chang and Mander (1994) model was implemented to represent the uniaxial behavior of concrete. Although the improved MVLEM provided satisfactory predictions for the flexural load-deformation response od walls that is generally accompanied by stiffness degradation, plastic displacement, and pinching behavior, it remained to be incapable of representing the interaction between shear and flexure responses of walls, similarly to the original MVLEM. Therefore, the MVLEM was deemed suitable for predominantly slender walls, in which nonlinear shear deformations are not of primary concern.

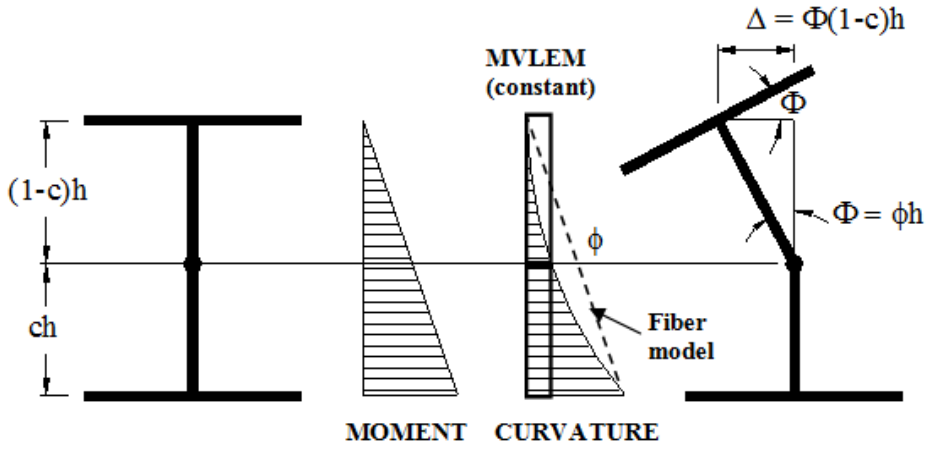

Figure 1.3. Flexural Deformations of MVLEM Element (Orakcal *et al.*, 2004).

Two experimental programs conducted by Thomsen and Wallace (2004) and Sayre (2003) were investigated elaborately by Massone (2006), for experimental characterization of the interaction between nonlinear shear and flexural responses in relatively slender walls. Deformations related with flexure and shear were determined for two,

approximately quarter scale, slender wall specimens with rectangular cross sections (RW2 of Thomsen and Wallace (2004), and SRCW1 of Sayre (2006)) in order to evaluate relative contributions to wall lateral displacements. The slender wall specimens were designed and detailed according to capacity design and displacement-based design approaches, respectively. Specimens were tested under reversed cyclic loading conditions with an axial load of approximately $0.1A_g f'_c$ in the upright position. Specimen RW2 was 3.66 m tall and 102 mm thick, with a web length of 1.22m, while specimen SRCW1 was 4.88 m tall, 152 mm thick, and 1.22m long, therefore aspect ratio (h_w/l_w) of wall specimens RW2 and SRCW1 were 3.0 and 4.0, respectively. The axial load was kept constant during testing of both RW2 and SRCW1, and a hydraulic actuator positioned at a level of 3.81m and 4.88m above the base of each specimen, respectively, were used to apply the lateral load. Both specimens were well instrumented to collect experimental data related to displacements, loads, and strains at critical locations. Wire potentiometers (WPs) were mounted on a rigid steel reference frame to measure lateral displacements over the wall height. Displacements measured with the WPs were calibrated with the help of the measurements from linear potentiometers (LPs) mounted horizontally and vertically on the wall foundation, which measured possible horizontal sliding of the foundation block (pedestal) along the strong floor, as well as rotations caused by uplift of the pedestal from the strong floor. In addition, two WPs mounted directly to the wall ends measured axial (vertical) displacements at the wall boundaries, for calculating wall base rotations by dividing the difference in relative axial displacements by the distance between the potentiometers.

Shear deformations within the first two levels of specimen RW2 and first three levels of specimen SRCW1 were obtained by using measurements from WPs placed on the walls diagonally in an "X" configuration. In order to measure average axial strains and to able to calculate section curvatures, vertically-oriented linear variable differential transducers (LVDTs) along the wall length just above the wall pedestal interface were mounted. Strain gauges that were mounted near the wall base were used to obtain strains in the reinforcing steel. To obtain further detailed information about experimental programs, papers by Thomsen and Wallace (2004) and Sayre (2003) are available. As well, detailed evaluation of the test results, with regards to shear-flexure

interaction behavior, is presented in the Ph.D. Thesis by Massone (2006).

A modeling methodology, in terms of plastic hinge approach that captures the interaction between axial, shear and flexural responses in RC columns, proposed by Zhang and Xu (2010, 2012). Inelastic response is modeled by the use of flexural and shear springs located within the column plastic hinge regions, whose behavior is governed by the flexural and shear backbone curves and a set of loading/unloading rules to describe the hysteretic characteristics of the response (e.g., pinching behavior, loading/reloading stiffness, softening and strength degradation); hysteretic model for shear by Ozcebe and Saatcioglu (1989) and hysteretic model for flexure by Takeda *et al.*, (1970) were used as bases to develop two improved hysteretic models for flexure and shear responses, respectively. Flexural and shear backbone curves are obtained by separating flexural and shear deformations from the total monotonic force-displacement relationship (backbone curve) of a column that accounts for shear-flexure interaction, which can be obtained either experimentally or analytically. In the modeling approach proposed by Zhang and Xu, the moment-curvature (M-ϕ) and the shear force-shear strain (V-γ) relationships are obtained for each section of a RC column by the use of Modified Compression Field Theory (MCFT, Vecchio and Collins 1986) based on the column geometry, reinforcement configuration, material properties, and applied external loads (Figure 1.4). Subsequently, the flexural deformation (Δ_f) and shear deformation (Δ_s) are obtained by integrating the curvature and shear strain in each section along the column length, which yield the bending moment-to-rotation angle (M-θ) and shear force-to-shear displacement (V-Δ_s) relationships used to define the envelopes of force-deformation behaviors of flexural and shear springs. Thus, the analytical model captures shear-flexure interaction at both section levels, when theoretically generating the backbone curves, and at the element level, through global and local equilibrium.

The proposed analytical model was used to simulate the behavior of two aspect ratios 2.0 RC walls tested by Lefas and Kotsovos (1990), specimen SW31 tested under monotonic loading and specimen SW33 tested under cyclic loading, as well as the behavior of RC columns that experienced shear-dominated behavior. The comparisons between the experimental and analytical results revealed that the model captures the

overall load-deformation response of considered wall specimens under monotonic and cyclic loading reasonably well, as well as the vertical strains at the wall boundary. In addition, Mullapudi *et al.*, (2009) investigated the sensitivity of analytical model results under monotonic loading to changes in wall slenderness ratio, transverse reinforcement ratio, and axial force using specimen SW 31 as the baseline model. Analytical results showed that the model captured systematic changes in local wall responses (e.g., normalized shear stress, distribution of normalized principal strains, and longitudinal boundary strains) with changes in mentioned wall parameters, whereas the sensitivity of global responses (e.g., lateral - load - versus - total - displacement) were not provided. Although the analytical model provided reasonably accurate predictions of behavior of moderate aspect ratio RC walls, the model validation studies were presented for a limited number of RC walls specimens (one monotonic and one cyclic test) as well as limited range of wall responses, i.e., lateral - load - versus - top - wall - displacement response and vertical boundary strain only, which are not overly sensitive to shear-flexure interaction.

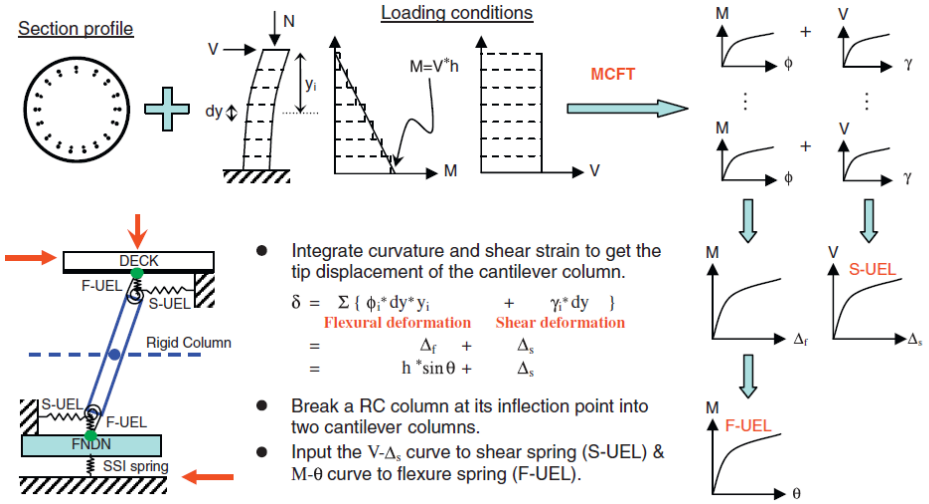

Figure 1.4. Implementation of Shear-Flexure Interaction (Zhang and Xu, 2010).

As an alternative approach, Panagiotou *et al.*, (2012) proposed a strut-and-tie approach to approximate the interaction between shear and flexural responses in RC walls. In this approach, a RC wall was modeled using nonlinear vertical, horizontal, and diagonal truss elements connected at nodes along which cyclic uniaxial material laws for concrete and steel were applied (Figure 1.5); the vertical and horizontal truss

elements represented reinforcing bars and their surrounding concrete, whereas diagonal truss elements represented the concrete alone The layout of the diagonal truss elements resembled but did not need to match, the principal compressive stress trajectories when approaching the ultimate load. Shear-flexure interaction in a model element was represented by reducing the capacity of a diagonal concrete truss element as a function of transverse tensile strain by the use of the concrete uniaxial material law that couples the element's compressive stress-strain behavior with the tensile strain normal to the element axis (Figure 1.6).

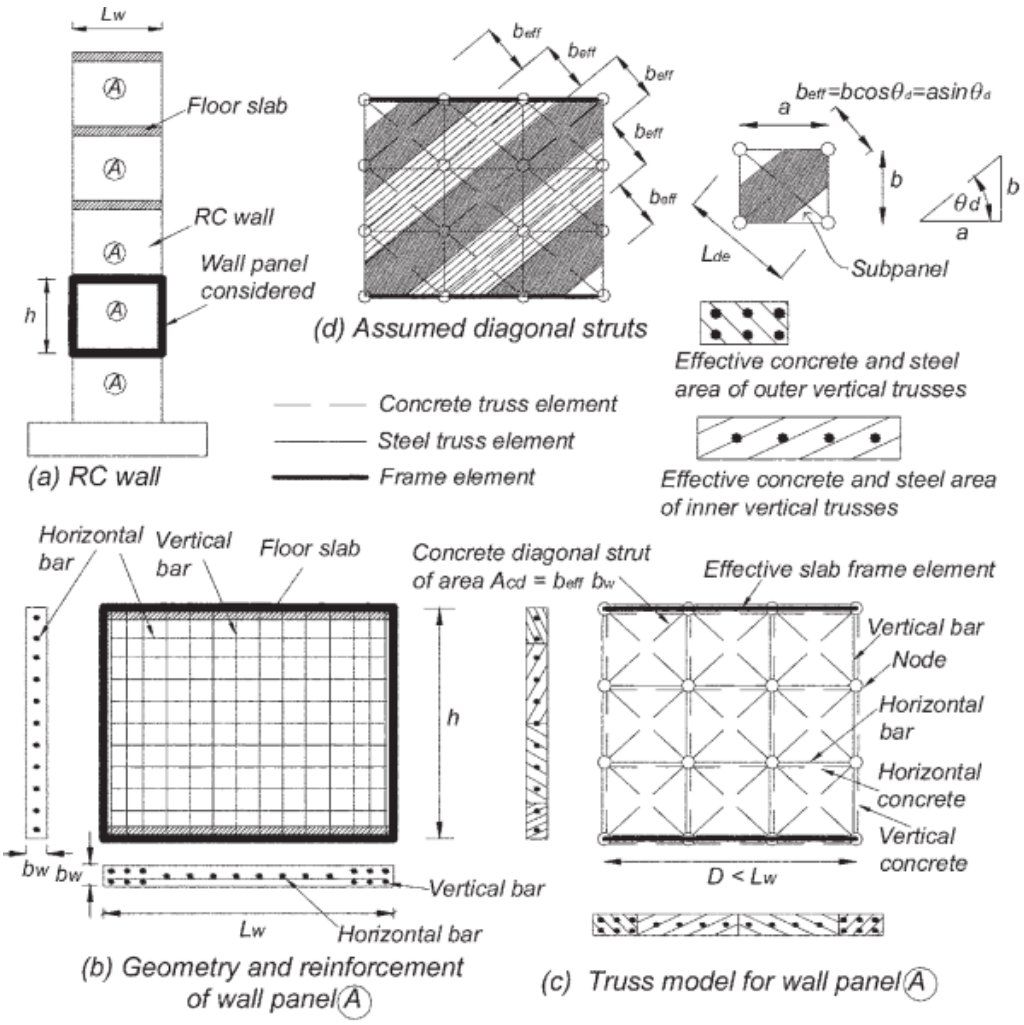

Figure 1.5. RC Wall and Wall Panel Truss Model Panagiotou *et al.*, 2012).

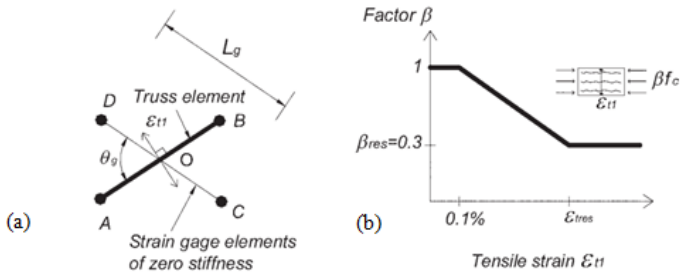

Figure 1.6. Coupled Compression-Tension Model for Diagonal Truss Elements: (a) Coupled Compression-Tension Truss Elements, (b) Concrete Compressive Stress Reduction due to Normal Tensile Strain (Panagiotou *et al.*, 2012).

In order to represent the interaction among nonlinear axial, flexural, and shear responses of RC walls, Petrangeli (1999) developed a model which implements fiber-based (multi-spring) model formulation into RC panel behavior. Later on, Massone *et al.*, (2006, 2009) modified the MVLEM by assigning a shear spring to each uniaxial element, which is then treated as a RC panel element subjected to in-plane uniform normal and shear stresses, as shown in Figure 1.7. A rotating-angle modeling approach, such as the Modified Compression-Field Theory (MCFT; Vecchio and Collins, 1986) or the Rotating-Angle Softened-Truss-Model (RA-STM; Hsu, 1993; Belarbi and Hsu, 1994 and 1995; Pang and Hsu, 1995), was used to model the constitutive panel behavior. The assumptions that forms the model formulation can be summarized as follows: Plane section remains plane, strain fields acting on concrete and reinforcing steel are identical (perfect bond between reinforcement and concrete), shear strains are uniformly distributed along the wall length, principal stress and strain directions coincide, and dowel action of reinforcement is equal to zero.

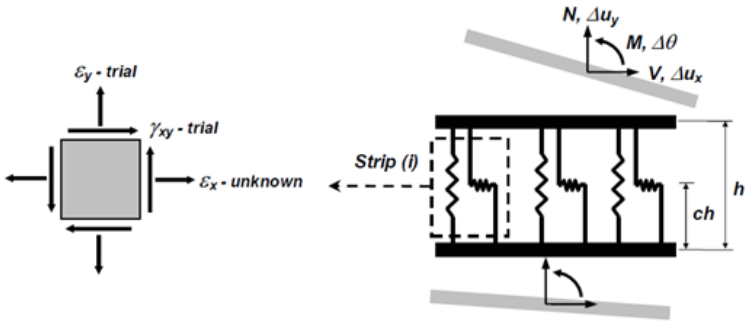

Figure 1.7. Coupled Model Element (Massone *et al.*, 2006, 2009).

A relatively new cyclic shear-flexure interaction modeling approach was developed by Kolozvari *et al.*, (2012). The model was validated by comparing the model predictions with experimental results obtained by Tran and Wallace (2012). The experimental study included five one-third scale cantilever RC wall specimens, were heavily instrumented to gain detailed response information, subjected to reversed cyclic lateral loading applied at the top of the walls with a constant axial load. The main goals of the test program were to investigate the impact of level of axial stress and average shear stress on the wall failure modes and lateral deformation capacity, as well as to assess the distribution and magnitude of lateral deformations associated with shear and flexure. Reasonable response predictions were gained with the shear - flexure - interaction model proposed by Kolozvari *et al.*, (2012) for the wall specimens with moderate aspect ratios. A description of the proposed model, significant characteristics of the model response predictions, and sensitivity of the model predictions to various modeling parameters and detailed comparisons with experimental results reported by Tran and Wallace (2012) are provided in the papers which are proposed by Kolozvari *et al.*, (2014). In Figure 1.8a the original formulation of MVLEM are shown. In the proposed SFI model formulation, each uniaxial element from the original formulation of the MVLEM is replaced with a RC panel element subjected to membrane actions (Figure 1.8b, Figure 1.8c. Behavior of the RC panel elements under reversed cyclic loading conditions is described using a 2D constitutive RC panel model formulation (Figure 1.8b based on the fixed - strut - angle - model (FSAM) developed by Ulugtekin (2010) and extended by Orakcal *et al.*, (2012) to incorporate shear aggregate interlock effects. The coupling of axial and shear responses is thus enabled at the panel (macrofiber) level, which further allows coupling of flexural and shear responses at the model element level. Although the approach is conceptually similar to the one proposed by Massone *et al.*, (2006), which addressed monotonic responses only, the proposed model with the FSAM panel model is capable of simulating cyclic responses. Detailed information about the new approach can be found in the papers proposed by Kolozvari *et al.*, 2014.

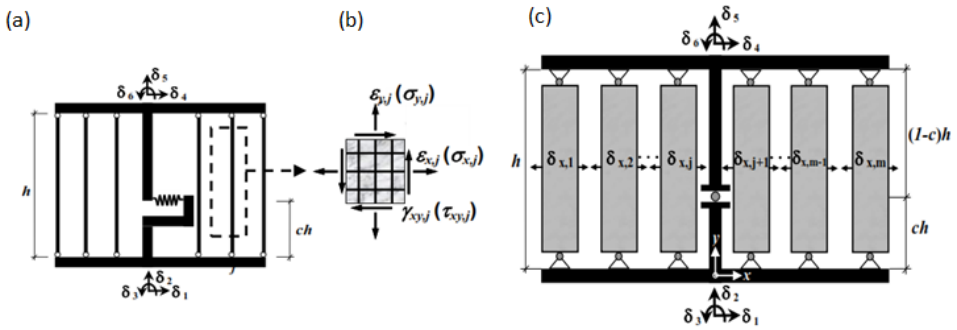

Figure 1.8. Element Models (a) original MVLEM element, (b) RC panel element, (c) SFI-MVLEM element (Kolozvari *et al.*, 2014).

Gullu (2013) proposed a new macroscopic finite element modeling approach for capturing the inelastic response of RC walls under reversed-cyclic loading. In this model, the fixed-crack-angle modeling approach, which is appropriate for reversed cyclic loading conditions, was also used. The primary objective of this study was to capture the unexpected shear yielding and nonlinear deformation behavior in slender RC walls. The analytical model successfully captured the stiffness degradation, shape of the load-displacement hysteresis loops, plastic displacements, and pinching behavior in slender walls. However, predictions of the proposed model were experimentally validated only for slender walls, which do not incorporate high-level shear-flexure interaction responses. As part of this study, improvements were made on the constitutive panel model formulation, to represent shear-aggregate-interlock effects in concrete, constituting the shear stress transfer mechanism across the cracks. This modeling approach, upon implementing a constitutive relationship to represent dowel action on reinforcing steel bars, was used by Orendil (2014) for predicting the lateral load responses of squat RC walls with predominantly shear-controlled responses.

1.3. Objectives and Scope

Although the lateral load behavior of RC structural walls have been widely investigated both experimentally and analytically, and there are numerous modeling approaches available in the literature for simulating their response, most of the available

modeling approaches focus on the characterization of the nonlinear flexural response of walls, or coupling of nonlinear flexural deformations with moderate levels of shear deformation. Existing approaches to model coupled shear and flexural responses typically incorporate ad-hoc modeling assumptions, some of which have not been experimentally validated against experimental data obtained for moderate aspect ratio structural walls with shear-controlled responses. There is still a need for a robust modeling approach to simulate the nonlinear hysteretic behavior of such walls.

Accordingly, the objective of this study is to adopt and experimentally-validate a new finite element modeling methodology for simulating the in-plane hysteretic lateral load behavior of moderate aspect ratio RC walls, with aspect ratios 1.5 and 2.0, involving significant shear flexure interaction and nonlinear shear deformations. The behavior of the constitutive panel (membrane) elements in the finite element model is described by a previously-developed constitutive panel model (i.e., the Fixed-Strut-Angle Model by Ulugtekin, 2010). Improvements were made on the constitutive panel model formulation for better representation of the shear-aggregate-interlock effects in concrete and dowel action in reinforcing bars, constituting the shear stress transfer mechanism across the cracks of the constitutive panel elements. Sensitivity studies were performed to investigate the variation in the model results with changes in various modeling parameters (aggregate interlock parameters and model discretization), wall configuration parameters (wall aspect ratio, boundary and web reinforcement ratios) and loading parameters (axial load level). The model was extensively calibrated for five moderately-slender RC wall specimens tested by Tran and Wallace (2012), and model predictions were compared with the experimentally-observed responses all five of the rectangular, moderate-aspect-ratio wall specimens. Model results were compared with test results not only at the global lateral load-displacement response level, but also at various deformation levels at different locations.

1.4. Thesis Outline

This thesis presents information on the modeling approach used, constitutive relationships incorporated in the model formulation, sensitivity of the analytical results

to model parameters, calibration of the model parameters, and comparison of the experimental and analytical results for moderately-slender RC walls. In Chapter 1, an introduction and a literature review, as well as the objectives and scope of this study are provided. Descriptions of constitutive panel model, the finite element modeling approach, and the shear transfer mechanisms across the cracks are presented in Chapter 2. Chapter 3 presents the results of the parametric sensitivity studies conducted using the model. Chapter 4 provides information on the test program used for experimental validation of the model as well as calibration of the model parameters. Chapter 5 focuses on comparison of model results with test results for the moderate-aspect-ratio wall specimens at various response levels and locations. Finally, concluding remarks and recommendations for model improvements are presented in Chapter 6.

2. MODEL DESCRIPTION

2.1. Overview

In this chapter, descriptions of the constitutive panel model formulation adopted in this study, the constitutive material relationships implemented in the constitutive panel model, the adopted macroscopic finite element modeling methodology, and the constitutive relationships implemented to represent transfer of shear stresses across cracks are provided. Finite element modeling of RC structural walls involves assembling of constitutive panel elements for obtaining the overall model of an wall. The behavior of the wall model is constituted by the combination of hysteretic nonlinear material relationships along crack directions of the constitutive panel together with behavioral response characteristics including compression softening, tension stiffening, hysteretic biaxial damage, and shear stress transfer across cracks.

The constitutive panel model implemented in the finite element model assembly is the so-called Fixed Strut Angle Model (FSAM), proposed by Ulugtekin (2010), since its simplicity in formation and its adequate accuracy makes the FSAM a feasible candidate for finite element model implementation. The formulation of the FSAM is based on interpretation and simplification of previously-developed RC panel models and results of RC panel tests available in the literature. A summary of the FSAM formulation is provided in the next section, whereas detailed information on the FSAM is available in the M.S. Thesis by Ulugtekin (2010).

However, for the present study, formulation of the original FSAM is improved. Originally, in the FSAM, the effects of shear aggregate interlock across cracks and dowel action on reinforcing steel bars were neglected. Significant overestimation of sliding shear strains may occur along crack directions due to the resulting assumption of zero shear stress developing along crack surfaces. In order to simulate shear aggregate interlock effects in concrete, a simple friction-based constitutive model was proposed by Orakcal *et al.*, (2012) and adopted by Gullu (2013). The shear aggregate interlock

constitutive model model used in this study is an extension of the one adopted by Gullu (2013). Furthermore, in the present study, a new nonlinear hysteretic constitutive relationship was developed and implemented in the model formulation for representing the dowel action developing on the reinforcing steel bars. Details on constitutive modeling of shear aggregate interlock behavior in concrete and dowel action on reinforcement in the present model formulation are presented in subsequent sections.

2.2. Constitutive Panel Model

In the original version of FSAM formulation, together with the perfect bond assumption between concrete and reinforcing steel bars, shear aggregate interlock effects along crack surfaces and dowel action on reinforcing bars are neglected. The strain fields acting on concrete and reinforcing steel components of an RC panel are assumed to be equal to each other as the result of the perfect bond assumption. While uniaxial directions along the rebar directions are used for the hysteretic constitutive modeling of reinforcing steel bars, biaxial relations along the fixed strut (crack) directions are incorporated for constitutive modeling of concrete stress-strain behavior.

To simulate the biaxial stress-strain behavior of uncracked concrete, a rotating strut approach, similar to the Modified Compression Field Theory (Vecchio and Collins, 1986) and the Rotating Angle Strut and Tie Model (Pang and Hsu, 1995) is utilized. The hysteretic behavior of concrete is assumed to be monotonic for small strains prior to cracking, for the uncracked loading stages. The principal strains directions acquired from the applied strain field are assumed to coincide with principal stress directions in concrete. As a result, the constitutive material model for concrete is applied along the principal strain directions (Figure 2.1).

The first crack in the RC panel forms in a perpendicular direction to the principal tensile strain, as the principal tensile strain exceeds the monotonic cracking strain value of concrete. For subsequent loading, this implies that the first "Fixed Strut" direction is already assigned, and it is parallel to the first crack. Furthermore, for subsequent loading stages, principal strain directions continue to rotate with the applied strain

field whereas principal stress directions in concrete coincide with the first crack direction (parallel and perpendicular). Since principal stress and crack directions coincide, zero shear stress develops along the crack directions, implying zero shear aggregate interlock and zero dowel action, which is the underlying assumption in the original FSAM formulation.

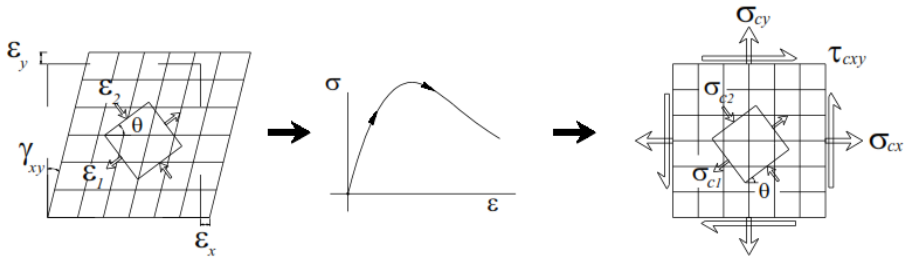

Figure 2.1. The Uncracked Behavior of Concrete in the Fixed Strut Angle Model (Orakcal *et al.*, 2012).

After the formation of the first crack, the hysteretic stress-strain relationship for concrete is used in parallel and perpendicular directions to the fixed strut. It should be noted that it is only possible to calculate the principal stresses in concrete with the transformation of the strain field into directions parallel and perpendicular to the fixed strut. Concrete stress values are indicated after the calculation of the strains that are parallel and perpendicular to the fixed strut direction by using the uniaxial constitutive model adopted for concrete. These calculated stresses are reduced by biaxial compression softening and biaxial damage parameters, which are described in the following section. The calculation of the stresses in reinforcing steel is acquired by the application of the hysteric uniaxial constitutive material model for reinforcing steel along the orthogonal rebar directions. By superimposing the stresses developing in concrete and reinforcing steel, the average stresses on the panel element are obtained. The behavior of concrete in the FSAM after the formation of the first crack is illustrated in Figure 2.2.

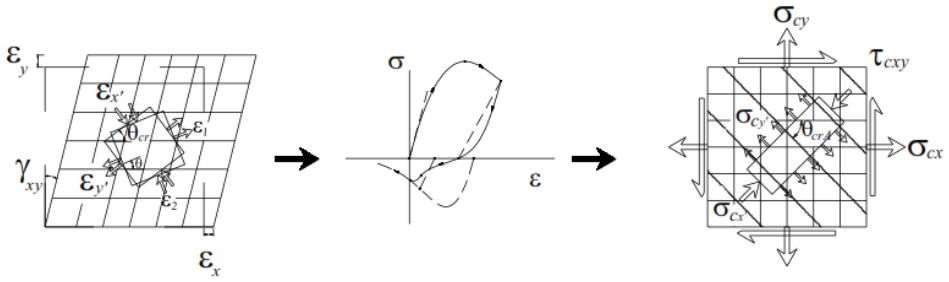

Figure 2.2. The Behavior of Concrete After the Formation of First Crack in the Fixed Strut Angle Model (Orakcal *et al.*, 2012).

The second crack is formed perpendicular to the first crack, as the tensile strain exceeds the cyclic cracking strain of concrete, due to the zero shear stress assumption along the crack directions. The constitutive behavior proceeds in the form of a single fixed strut mechanism until that stage. The first and second cracks being perpendicular is an example of the so-called "orthogonal crack" modeling approach, which has also been adopted in other constitutive panel model formulations. The second crack, being perpendicular to the first fixed strut, implies the formation of the second "fixed strut" direction. Depending on the loading direction, these fixed struts work either under tension or under compression. Principle stress directions are fixed along the fixed strut directions while principal strain values are able to rotate freely for subsequent loading stages. Instead of using principal strain directions for calculating the principle stresses in the concrete, the applied strain field is transformed into strain components in the fixed strut directions. Calculated strain values are used in the uniaxial constitutive model for concrete in order to obtain the principle stresses in concrete. Through compression softening and biaxial damage parameters, the concrete stresses are reduced. The constitutive material model for reinforcing steel is applied along the orthogonal rebar directions, and superposition of stresses developing in concrete and reinforcing steel provides the resultant average (smeared) stresses on the panel element. The behavior of concrete in the FSAM after the formation of the second crack is illustrated in Figure 2.3.

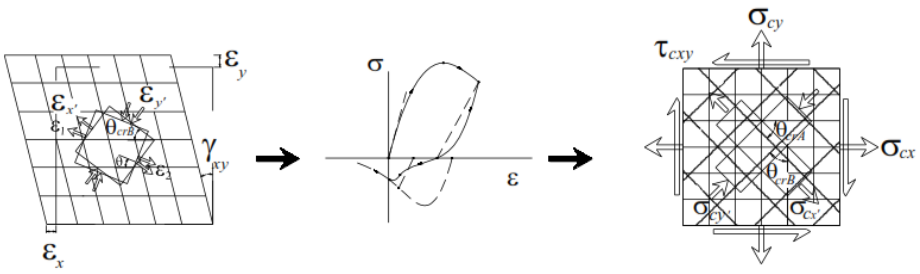

Figure 2.3. The Behavior of Concrete after the Formation of Second Crack in the Fixed Strut Angle Model (Orakcal *et al.*, 2012).

2.3. Constitutive Material Models

2.3.1. Constitutive Model for Reinforcement

In the constitutive panel model (FSAM), the behavior of reinforcing steel is represented by the well-known nonlinear hysteretic relationship of Menegotto and Pinto (1973), as extended by Filippou *et al.*, (1983) to incorporate isotropic strain hardening effects. This constitutive material model also represents the so-called Bauschinger's effect, by incorporating cyclic degradation of tangent stiffness in the unloading and reloading curves. Description of the constitutive reinforcing steel model is shown in Figure 2.4.

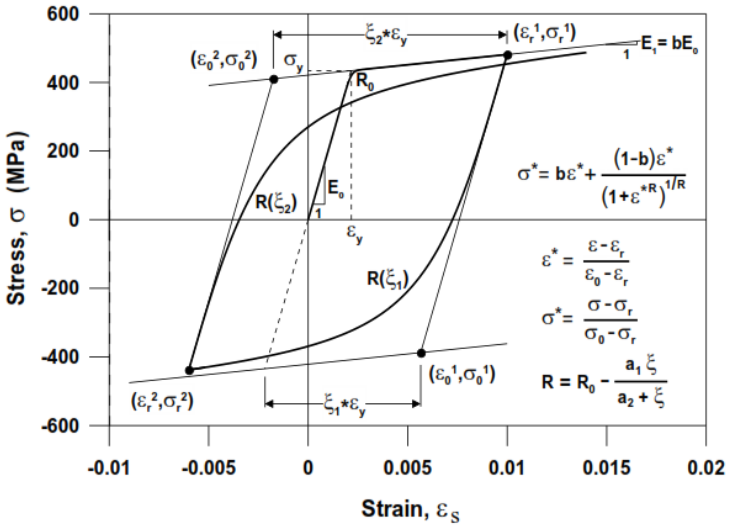

Figure 2.4. The Hysteretic Constitutive Model for Reinforcing Steel (Menegotto and Pinto, 1973).

2.3.2. Constitutive Model for Concrete

The uniaxial hysteretic constitutive model proposed by Chang and Mander (1994) is adopted to represent the uniaxial hysteretic stress-strain behavior of concrete along fixed strut directions in the FSAM. The advantage of the Chang and Mander (1994) Model is that it is a rule-based, generalized, and non-dimensional model that can simulate the hysteretic behavior of both confined and unconfined concrete, under continuous compression and tension loading. The Chang and Mander (1994) model has been shown to provide accurate representations of experimental results presented by various researchers. For unconfined concrete in cyclic compression, the model provided accurate predictions of experimental results presented by Karsan and Jirsa (1969), and Mander *et al.*, (1988a). Mander *et al.*, (1988b) performed tests on confined concrete and confirmed the model accuracy. The experiments conducted by Gopalaratnman and Shah (1985) and Yankelevsky and Reinhardt (1987) showed that the behavior of concrete in tension is similar to the behavior of concrete in compression. Based on this observation, the model by Chang and Mander (1994) recommends similar envelopes for tension and compression (Figure 2.5), with different stress magnitudes.

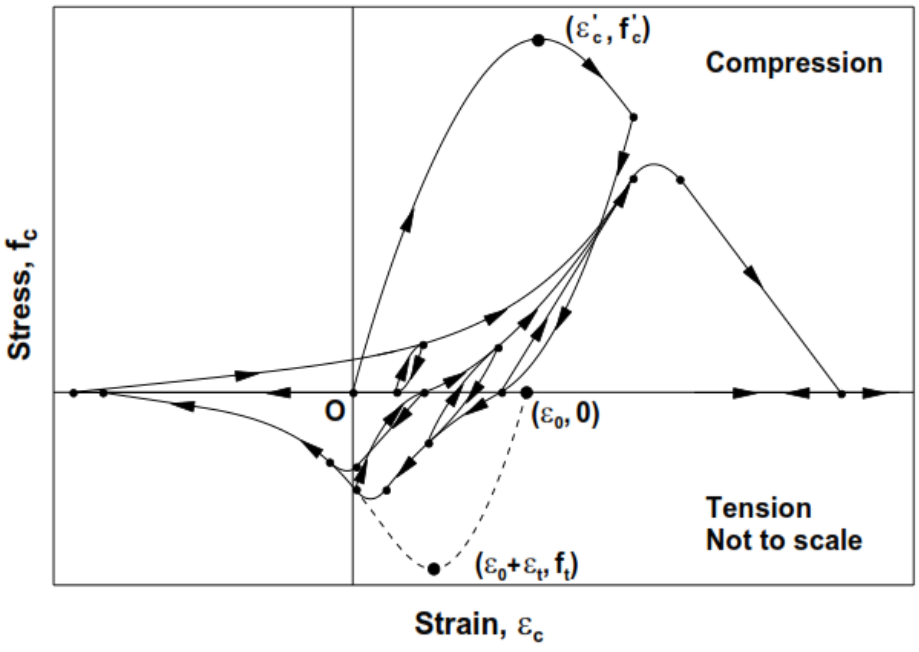

Figure 2.5. The Hysteretic Constitutive Model for Concrete (Chang and Mander, 1994).

In the FSAM, the formulation of the Chang and Mander (1994) model was modified by incorporating parameters to represent compression softening (defined by Vechio and Collins, 1993), hysteretic biaxial damage (defined by Mansour *et al.*, 2002), and tension stiffening effects (defined by Belarbi and Hsu, 1994) into its formulation. These modifications, which are described in the following sections, aim to simulate the behavioral features of concrete subjected to biaxial loading along the perpendicular strut directions.

2.3.3. Compression Softening Effect on Concrete

For the modeling the behavior of RC panel elements, compression softening effect is an important consideration. Although the behavior of concrete under biaxial stress state was first determined by Kupfer, Hilsdorf and Rüsch in 1964, the softening effect has been experimentally observed by many other researchers, (e.g., Vecchio and Collins, 1986) and representative constitutive relationships were proposed. Stemming from the tensile strains perpendicular to crack directions, compression softening is the reduction in the compressive stresses in concrete along the principal compression direction of RC panels (Figure 2.6).

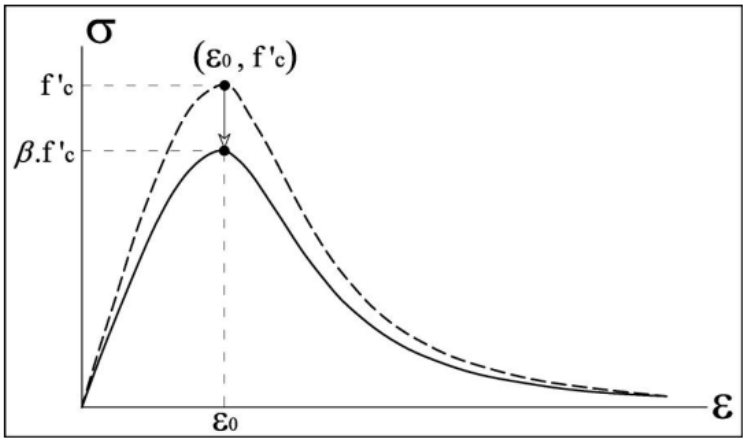

Figure 2.6. Compression Softening Effects Implemented in the Panel Model (Ulugtekin, 2010).

The compression softening relationship proposed by Vecchio and Collins (1993)

was applied to the formulation of the FSAM. There are more complicated models available in the literature representing compression softening effects; however, this relationship was found to provide reasonably accurate predictions of experimentally-observed stress vs. strain behavior, despite its relatively simple formulation.

2.3.4. Tension Stiffening Effects on Concrete and Reinforcing Steel

The contribution of cracked concrete to the tensile resistance of RC members is defined as tension stiffening. The tension stiffening effect influences the post-cracking stiffness, yield capacity and shear behavior of the RC members. The impact of tension stiffening has been studied by many researchers (e.g. Vecchio and Collins, 1988; Stevens, 1987; Collins and Mitchell, 1991; Belarbi and Hsu, 1994; Pang and Hsu, 1995; Hsu and Zhang, 1996; Mansour *et al.*, 2002; Hsu and Zhu, 2002).

The tension stiffening relationship that was proposed by Belarbi and Hsu (1994) was implemented in the formulation of the constitutive panel model. The tension stiffening phenomenon considers two significant effects simultaneously. The first one is the consideration of an average (smeared) tensile stress-strain curve for cracked concrete; and the second one, replacement of the uniaxial stress-strain relationship of bare reinforcing bar with a mean stress-strain curve of defined for bars stiffened by concrete between cracks.

2.3.5. Biaxial Damage Effect on Concrete

The cyclic damage effects on concrete subjected to biaxial loading is another significant consideration in modeling the behavior of an RC panel element. This damage on concrete is represented with a damage coefficient. Unlike compression softening and tension stiffening parameters, the damage coefficient is a cyclic-strain-history-dependent parameter. Depending on the maximum value of the previously-applied compressive strain in the perpendicular direction, the biaxial damage effect physically reflects as softening in the compressive stress-strain behavior of concrete along one direction. Therefore, the biaxial damage behavior is loading-history-dependent and is

not observed under monotonic loading. In terms of constitutive modeling, the damage coefficient, similarly to the compression softening coefficient, is typically applied as a reducing multiplier to compressive stresses in the concrete. There are two models for the damage coefficient in the literature; Stevens (1987), Mansour and Hsu (2002). The biaxial damage formulation proposed by Mansour and Hsu (2002) was implemented into the formulation of constitutive Fixed Strut Angle Panel Model.

2.3.6. Constitutive Modeling of the Shear Aggregate Interlock Effect in Concrete

In the original formulation of the Fixed-Strut-Angle constitutive panel model developed by Ulugtekin (2010), the shear aggregate interlock effect along crack surfaces in concrete were neglected. To remedy this shortcoming of the original FSAM, the cyclic shear aggregate interlock model proposed by Orakcal *et al.*, (2012) starts with linear loading/unloading behavior, relating the sliding shear strain along a crack to the shear stress, via a simple linear elastic relationship between the sliding shear strain and the resultant shear stress along the crack surface. When the concrete normal stress perpendicular to the crack is tensile (crack open), the shear stress is restrained to zero value and when the concrete normal stress is compressive (crack closed), is bounded via the product of a friction coefficient and the concrete normal stress perpendicular to the crack. The linear unloading/reloading slope of the shear stress vs. sliding strain relationship was taken as a fraction of the concrete elastic modulus (a value 0.4 E_c was adopted, representing the elastic shear modulus of concrete), and a value of 1.0 was assumed for the friction coefficient, which needs to be multiplied by the compressive stress in concrete in perpendicular direction to the crack, in order to obtain the shear stress capacity along the crack surface (Figure 2.7a). Under constant compressive stress in concrete perpendicular to the crack, this model yields an elasto-plastic aggregate interlock behavior under cyclic loading, similar to the cyclic stress-strain behavior of reinforcing steel. Gullu and Orakcal (2014) also considered the clamping effect of reinforcing steel bars straddling the crack surface to the sliding shear stress (shear friction) capacity of the aggregate interlock model, similarly to the approach presented in ACI-318-11 (Figure 2.7b).

As mentioned in the paper by Kappos *et al.*, (2011), the mechanisms mobilized along interfaces due to slip and their interaction is a rather complex mechanical issue, especially under cyclic loading conditions where degradation should also be accounted for. In addition, Kappos *et al.*, (2011) recommends the shear aggregate interlock friction coefficient μ to be taken equal to a value of 0.44 regardless of whether the interlock affects are induced by compressive stresses in concrete or clamping effect on reinforcing bars. In this study, contribution of the clamping force created by the reinforcing steel bars to the shear friction capacity is represented by a friction coefficient of $\mu_s = 0.5$, whereas contribution of the compressive stress in concrete perpendicular the crack surface is considered using a friction coefficient $\mu = 1$, based on sensitivity studies conducted using the model on previously-conducted tests on squat RC walls experiencing sliding shear failure (Terzioglu, 2011). As well, while sliding shear stresses on the crack surface resulting from the compressive stress in concrete follows elasto-plastic hysteretic behavior (Figure 2.7a), those resulting from the clamping force of the reinforcing steel bars are assumed to follow an origin-oriented hysteretic behavior (Figure 2.8). In the present study, different values are used for μ_s and μ_c; however, degradation of the aggregate interlock stresses with the number of loading cycles (Kappos *et al.*, 2011) is not considered. An origin-oriented hysteretic behavior for the clamping-induced interlock stresses and a value of 0.5 for μ_s were selected based on results of the aforementioned tests on squat RC walls (Terzioglu, 2011), as well as recommendations by Kappos *et al.*, (2011).

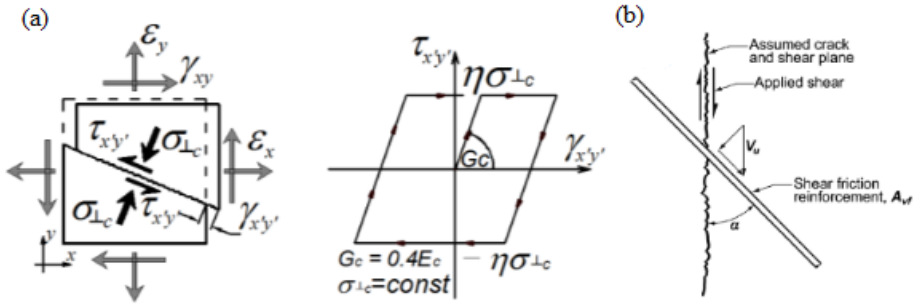

Figure 2.7. a-) Friction Based Constitutive Model for Shear Aggregate Interlock (Orakcal *et al.*, 2012), b-) Shear Friction Mechanism along a Crack in ACI- 318.

2.3.7. Constitutive Modeling of Dowel Action on Reinforcing Bars

The nonlinear flexural behavior of RC walls can be accurately estimated using relatively simple modeling approaches. However, accurate prediction of the nonlinear shear behavior of RC walls remains to be formidable task, even with the use of finite element modeling approaches. This, in part, is due to complexity of the shear transfer mechanism along cracks in concrete, and the lack of suitable models for the various actions that contribute to the shear transfer. A constitutive model representing dowel action on reinforcing bars was developed by He and Kwan (2001), for incorporation in finite element analysis of reinforced concrete structures. This constitutive dowel action model was implemented in the present study into the FSAM formulation, due to its relative simplicity. An overview of the dowel action model by He and Kwan (2001) is presented in this section.

In the dowel action model by He and Kwan (2001), the dowel effects on the reinforcing steel bars crossing cracks in concrete is represented in a smeared form in order to be compatible with the smeared crack model and smeared reinforcement model used in finite element analysis. A representative cracked concrete element containing a reinforcing steel bar crossing the crack perpendicularly is depicted in Figure 2.8.

When the concrete blocks at the two sides of the crack slide against each other, the reinforcement bar embedded inside the concrete is subjected to dowel displacement, which is defined as the relative transverse displacement of the two ends of the reinforcement bar. Due to the dowel deformation so caused, transverse shear force and contraflexural bending moment are developed in the reinforcement bar. However, only a certain length of the bar in the vicinity of the crack is subjected to significant dowel deformation. Denoting the length of the bar subjected to significant dowel deformation by l, the dowel displacement Δ may be calculated from the shear strain across the crack γ_{12} using the Equation 2.1. The dowel force V_d developed in the bar varies with the dowel displacement Δ according to a certain dowel force - displacement relation. Using the secant stiffness formulation, the dowel force and the dowel displacement can be related by Equation 2.2. where K_d is the secant dowel stiffness of the reinforcement

bar. The dowel force V_d acts against the concrete and may be smeared over the crack surface as a dowel stress acting across the crack. The dowel stress may be calculated from the dowel force from Equation 2.3 in which ρ_s is the reinforcement ratio in the crack direction and is the sectional area of the reinforcement. Equation 2.4 was derived from putting Equation 2.1 to Equation 2.3 together.

The case of a reinforcing bar crossing a crack at an acute angle is more complicated because apart from the shear strain, the tensile strain across the crack can also cause dowel displacement of the reinforcement bar. Consider the cracked concrete element containing a reinforcement bar running in the x-direction in Figure 2.9a and the cracked concrete element containing a reinforcement bar running in the y-direction in Figure 2.9b. The dowel displacements Δ_x of the bar running in the x-direction and Δ_y of the bar running in the y-direction are given in Equation 2.5 and Equation 2.6. In the present model formulation, dowel displacements Δ_x and Δ_y are defined as an equal values that are calculated by using the half of the shear strain acting on the panel element, γ_{xy}. The dowel forces are identified as V_{dx} and V_{dy} develop in the two reinforcing bars running in the x and y directions, respectively. The corresponding dowel stresses (τ_x, τ_y) developing in the reinforcing bars are expressed as Equation 2.7 and Equation 2.8. Equilibrium requires that τ_{xy} should be equal to τ_{yx} for panel elements; however, τ_x and τ_y are not necessarily equal to each other. Therefore, the smeared dowel stress τ_{xy} is defined as an average value of τ_x and τ_y. The dowel action effects on the vertical and horizontal reinforcing steel bars in a RC wall are thus incorporated in the formulation of the FSAM.

$$\Delta = \ell \times \gamma_{12} \tag{2.1}$$

$$V_d = K_d \times \Delta \tag{2.2}$$

$$\tau_{12}^d = \frac{\rho_s}{A_s} \times V_d \tag{2.3}$$

$$\tau_{12}^{d} = \frac{\rho_s}{A_s} \times K_d \times \ell \times \gamma_{12} \tag{2.4}$$

$$\Delta_x = \ell_x(\varepsilon_1 cos\theta \sin\theta + \gamma_{12}\cos^2\theta) \tag{2.5}$$

$$\Delta_y = \ell_y(\varepsilon_1 cos\theta \sin\theta - \gamma_{12}\sin^2\theta) \tag{2.6}$$

$$\tau_{x}^{d} = \frac{\rho_x}{A_{sx}} \times V_{dx} \tag{2.7}$$

$$\tau_{y}^{d} = \frac{\rho_y}{A_{sy}} \times V_{dy} \tag{2.8}$$

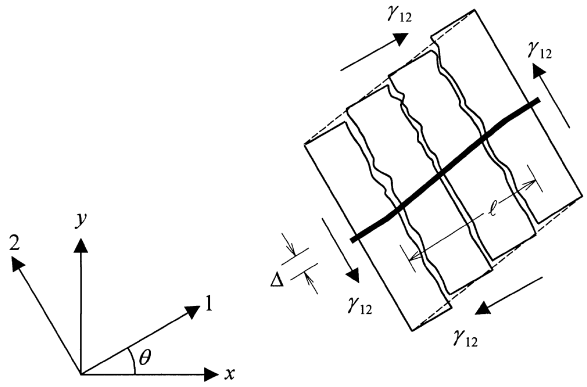

Figure 2.8. Dowel action of a Reinforcement Bar Crossing a Crack (He and Kwan, 2001).

In this dowel action model, the dowel force at ultimate limit state V_{du} is expressed as in Equation 2.1. In this equation, f_c represents the compressive strength of the concrete in MPa, d_b is the diameter of the bar in mm and f_y is the yield strength of reinforcing steel bar. This equation is based on experimental results conducted by Dulacska (1972). A similar empirical equation has also been proposed by Vintzeleou and Tassios (1987). Detailed information on derivation of this empirical equation is

presented in the paper proposed by He and Kwan (2001).

$$V_{du} = 1.27 \times d_b^2 \times \sqrt{|f_c| \times |f_y|} \tag{2.9}$$

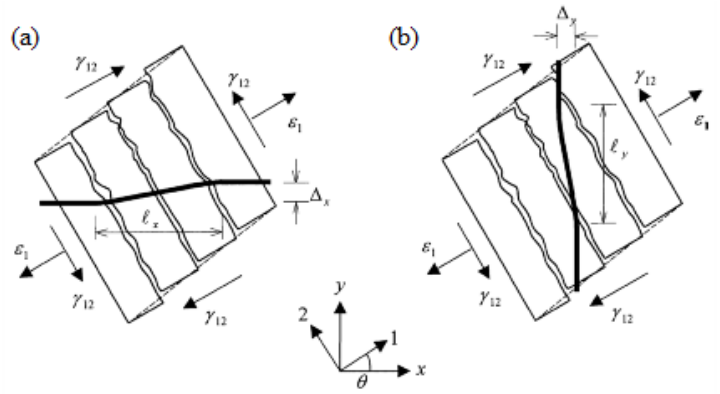

Figure 2.9. a-) Cracked Concrete Elements Containing a Reinforcement Bar Running in the x-Direction Crossing the Cracks at Acute Angle, b-) Cracked Concrete Elements Containing a Reinforcement Bar Running in the y-Direction Crossing the Cracks at Acute Angle (He and Kwan, 2001).

Overall, in the present study, the elasto-plastic dowel action model presented by He and Kwan (2001) is implemented as the monotonic envelope of the dowel force vs. shear strain constitutive relationship, and origin-oriented unloading and reloading paths are adopted to represent hysteretic behavior (Figure 2.10). An origin-oriented hysteretic behavior was selected for the implementation, because despite its simple formulation, it reasonably represents more detailed hysteretic relationships available in the literature for dowel action on reinforcing bars.

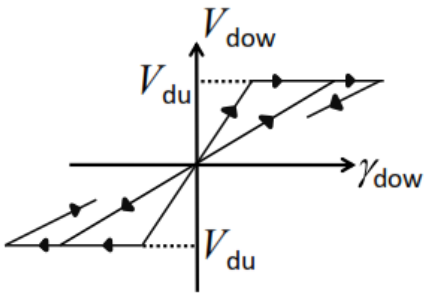

Figure 2.10. Dowel Action Model.

2.4. Finite Element Modeling Methodology

This section presents a brief description of the two-dimensional finite element modeling methodology that was used for assembling the constitutive panel elements described in the previous sections into a wall model, similarly to the methodology adopted by Gullu (2013) for modeling of slender walls. The internal force vector of these local elements (mesh elements) and the assembly of the local stiffness matrices are described in the following subsections. As well, summary information on the formulation of support conditions and constraints for modeling of walls are presented. The adopted nonlinear analysis solution strategy is also summarized. Further details on the finite element model assembly procedure are available in the M.S. Thesis by Gullu (2013).

2.4.1. 4 Nodes, 8 Degree of Freedom Rectangular Element

A rectangular two-dimensional finite element modeling approach is adopted for the present study. Four-node, eight-degree-of-freedom finite elements were used as constitutive model elements. At each node, the model element has two degrees of freedom (DOFs), one in vertical and one in horizontal direction. Model elements do not incorporate rotational DOFs; only in-plane loading conditions are considered in the formulation of the model since the constitutive elements are membrane (panel) elements. As a result, the model does not possess any, out-of-plane stiffness, and only in-plane loads are considered in the analysis.

Each local DOF of the rectangular model element is numbered as shown in Figure 2.11a. Average in-plane strains in each model element are calculated using simple linear shape functions, based on the displacement values along the nodal DOFs. (Figure 2.11b).

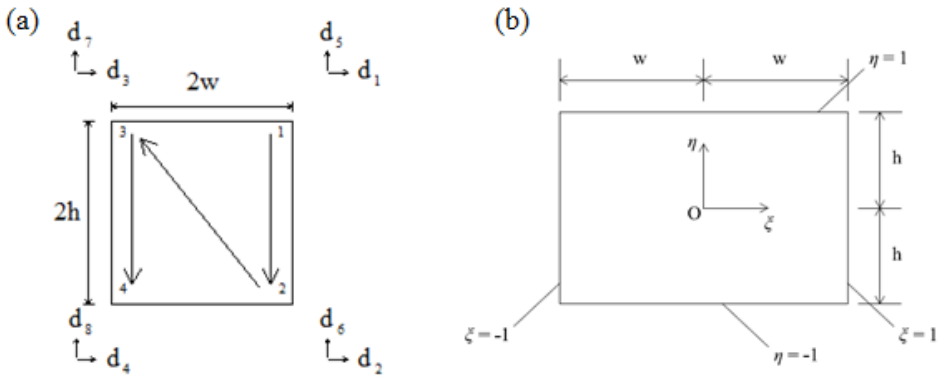

Figure 2.11. a-) Local Nodes and DOFs in a Rectangular Model Element, b-) Normalized Coordinates of a Rectangular Model Element.

Using the known displacements along the DOFs, (Figure 2.11a), which are obtained by solving equilibrium equations at the four nodes of the rectangular element, and the shape functions presented in Equation 2.10 to Equation 2.13, displacement values along horizontal and vertical directions at any point of rectangular element can be obtained (Equation 2.14). Strain and stress values are however only calculated at the center of each rectangular element, corresponding to $\zeta = \eta = 0$, for simplicity.

$$N_1 = \frac{1}{4}(1+\zeta)(1+\eta) \tag{2.10}$$

$$N_2 = \frac{1}{4}(1+\zeta)(1-\eta) \tag{2.11}$$

$$N_3 = \frac{1}{4}(1-\zeta)(1+\eta) \tag{2.12}$$

$$N_4 = \frac{1}{4}(1-\zeta)(1-\eta) \tag{2.13}$$

$$\begin{Bmatrix} u \\ v \end{Bmatrix} = \begin{bmatrix} N_1 & N_2 & N_3 & N_4 & 0 & 0 & 0 & 0 \\ 0 & 0 & 0 & 0 & N_1 & N_2 & N_3 & N_4 \end{bmatrix} \begin{Bmatrix} d_1 \\ d_2 \\ d_3 \\ d_4 \\ d_5 \\ d_6 \\ d_7 \\ d_8 \end{Bmatrix} \tag{2.14}$$

At the beginning of each load step, initial displacements at each node of a structural wall model are transformed into eight nodal displacement values defined for each model element). After this process, deformations of each element are calculated by using the transformation matrix [B], using Equation 2.15. Next, average strain values in each model element are computed using Equation 2.16, Equation 2.17 and Equation 2.18 for each model element and the tangent stiffness matrix terms for each element are calculated as output values as depicted in Figure 2.12, where average strain values are the input values for the Fixed Strut Angle constitutive model.

$$\begin{Bmatrix} defx \\ defy \\ defyx \\ defxy \end{Bmatrix} = \begin{bmatrix} \frac{1}{2} & \frac{1}{2} & -\frac{1}{2} & -\frac{1}{2} & 0 & 0 & 0 & 0 \\ 0 & 0 & 0 & 0 & \frac{1}{2} & -\frac{1}{2} & \frac{1}{2} & -\frac{1}{2} \\ \frac{1}{2} & -\frac{1}{2} & \frac{1}{2} & -\frac{1}{2} & 0 & 0 & 0 & 0 \\ 0 & 0 & 0 & 0 & \frac{1}{2} & \frac{1}{2} & -\frac{1}{2} & -\frac{1}{2} \end{bmatrix} \begin{Bmatrix} d_1 \\ d_2 \\ d_3 \\ d_4 \\ d_5 \\ d_6 \\ d_7 \\ d_8 \end{Bmatrix} \tag{2.15}$$

$$\varepsilon_x = \frac{defx}{2w} \tag{2.16}$$

$$\varepsilon_y = \frac{defy}{2h} \tag{2.17}$$

$$\gamma_{xy} = \frac{defyx}{2h} + \frac{defxy}{2w} \tag{2.18}$$

$$\begin{Bmatrix} \varepsilon_x \\ \varepsilon_y \\ \gamma_{xy} \end{Bmatrix} \rightarrow \text{Fixed Strut Angle Panel Model (FSAM)} \rightarrow \begin{bmatrix} E_{11} & E_{12} & E_{13} \\ E_{21} & E_{22} & E_{23} \\ E_{31} & E_{32} & E_{33} \end{bmatrix}$$

Figure 2.12. Tangent Stiffness (Elasticity) Matrix Calculation Path.

The objective is to generate the global tangent stiffness matrix by assembling the local stiffness matrices of the model elements. Each local stiffness matrix is obtained by using the tangent stiffness matrix and the geometric properties of each element, performed by integration of the product of transpose of strain matrix $[G]^T$ elasticity matrix [E], and strain matrix [G], as in definition of the finite element modeling approach. During the volume integration given in Equation 2.19, normalized coordinates $\zeta = \frac{x}{w}, \eta = \frac{y}{h}$ are to be considered dependent on x and y, respectively.

$$[k] = \int_V [G]^T [E] [G] \, dV = \int_V [G]^T [E] [G] \, dxdydz \tag{2.19}$$

The integral Equation 2.19 is used to calculate the 8x8 local stiffness matrix [k] for each model element (Equation 2.20 to Equation 2.31). In the equations, $\beta = \frac{h}{w}$, t is the thickness of the membrane element and E values are scalars taken from the tangent stiffness matrix. Using the equations below, the 8x8 local stiffness matrix for each element can be obtained as the matrix depicted in Equation 2.32.

$$k_{11} = \frac{t}{3}\left(E_{11}\beta + E_{33}\frac{1}{\beta}\right) \tag{2.20}$$

$$k_{21} = \frac{t}{3}\left(E_{11}\frac{\beta}{2} - E_{33}\frac{1}{\beta}\right) \tag{2.21}$$

$$k_{31} = \frac{t}{3}\left(-E_{11}\beta + E_{33}\frac{1}{2\beta}\right) \tag{2.22}$$

$$k_{41} = \frac{t}{3}\left(-E_{11}\frac{\beta}{2} - E_{33}\frac{1}{2\beta}\right) \tag{2.23}$$

$$k_{51} = \frac{t}{4}\left(E_{12} + E_{33}\right) \tag{2.24}$$

$$k_{61} = \frac{t}{4}\left(-E_{12} + E_{33}\right) \tag{2.25}$$

$$k_{71} = \frac{t}{4}\left(E_{12} - E_{33}\right) \tag{2.26}$$

$$k_{81} = \frac{t}{4}\left(-E_{12} - E_{33}\right) \tag{2.27}$$

$$k_{55} = \frac{t}{3}\left(E_{22}\frac{1}{\beta} + E_{33}\beta\right) \tag{2.28}$$

$$k_{65} = \frac{t}{3}\left(-E_{22}\frac{1}{\beta} + E_{33}\frac{\beta}{2}\right) \tag{2.29}$$

$$k_{75} = \frac{t}{3}\left(E_{22}\frac{1}{2\beta} - E_{33}\beta\right) \tag{2.30}$$

$$k_{85} = \frac{t}{3}\left(-E_{22}\frac{1}{2\beta} - E_{33}\frac{\beta}{2}\right) \tag{2.31}$$

$$[k] = \begin{bmatrix} k_{11} & k_{21} & k_{31} & k_{41} & k_{51} & k_{61} & k_{71} & k_{81} \\ k_{21} & k_{11} & k_{41} & k_{31} & k_{71} & k_{81} & k_{51} & k_{61} \\ k_{31} & k_{41} & k_{11} & k_{21} & k_{61} & k_{51} & k_{81} & k_{71} \\ k_{41} & k_{31} & k_{21} & k_{11} & k_{81} & k_{71} & k_{61} & k_{51} \\ k_{51} & k_{71} & k_{61} & k_{81} & k_{55} & k_{65} & k_{75} & k_{85} \\ k_{61} & k_{81} & k_{51} & k_{71} & k_{65} & k_{55} & k_{85} & k_{65} \\ k_{71} & k_{51} & k_{81} & k_{61} & k_{75} & k_{85} & k_{55} & k_{65} \\ k_{81} & k_{61} & k_{71} & k_{51} & k_{85} & k_{75} & k_{65} & k_{55} \end{bmatrix} \tag{2.32}$$

The local stiffness matrix [k] of each model element is symmetrical. The next step is assembly of these local stiffness matrices to generate the global stiffness matrix for the wall model.

2.4.2. Finite Element Model Stiffness Assembly

As shown in Figure 2.13a, a rectangular wall model is divided into model elements that are first numbered for the assembly operation. Then, the overlapping terms of the 8x8 local stiffness matrices are superimposed with each other for generating the global stiffness matrix. In the illustrated wall model with four elements, the global DOFs of the wall model are numbered as shown in Figure 2.13b which also defines the order of the terms in the global displacement vector and global stiffness matrix.

In Figure 2.13b, local DOF numbers are displayed inside the model elements whereas global DOF numbers outside the model elements. Global stiffness matrix of this sample model is calculated by superimposing the local stiffness terms at overlapping locations within the global stiffness matrix.

Equation 2.33 is an example for calculation of one of the terms in the global stiffness matrix. Superscripts in Equation 2.33 indicate the model element numbers while subscripts indicate the local stiffness term index for each model element. Each term in the global stiffness matrix of the wall model is calculated by the same procedure. As this sample includes 18 global DOFs, the resulting global stiffness matrix will be an 18x18 matrix.

$$[K]_{99} = [k]^{1}_{11} + [k]^{2}_{33} + [k]^{3}_{22} + [k]^{4}_{44} \tag{2.33}$$

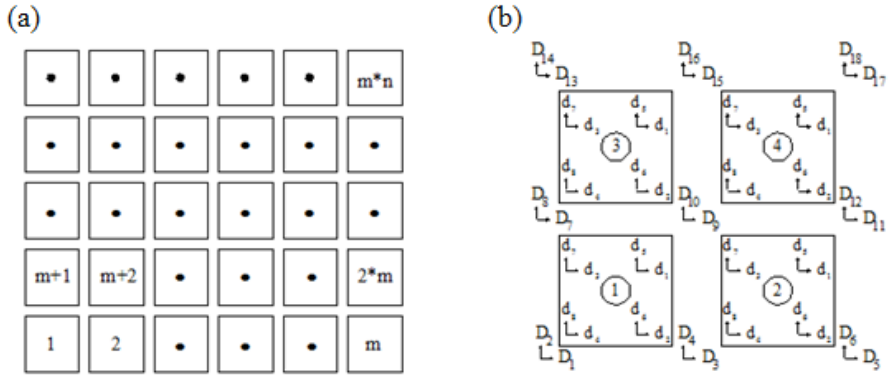

Figure 2.13. a-) Numbering Technique Used for the FEM of a Rectangular Wall, b) Global and Local DOFs for a Wall Model.

2.4.3. Internal Force Vector Assembly

The assembly procedure for the local internal force vectors, in order to obtain the global internal force vector is explained in this section. The average stresses in each element can be calculated using the constitutive Fixed Strut Angle Panel Model and these stress values are multiplied with the model element thickness and half of the vertical or horizontal width of the model element and are superimposed to obtain the internal force vector for each model element.

The numbering of the internal force vector components is illustrated in Figure 2.14 and the obtained stress values are used in combination to calculate the terms of

the internal force vector for each model element. In the next step, the local internal force vectors are superimposed, and thereby, the global internal force vector for the wall model is obtained.

For the assembly operation, the global internal force vector of the sample wall model is subdivided into four model elements calculated by superimposing the local internal force vector terms at overlapping locations within the global force vector. After numbering of each model element as per the example in Figure 2.14, the intersection of 8 x 1 local internal force vectors with each other are superimposed for generating the global internal force vector.

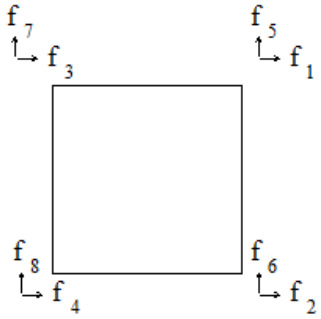

Figure 2.14. Numbering of Internal Force Terms for a Model Element (Gullu, 2013).

The adopted numbering scheme and the obtained stress values can be used in combination to calculate the terms of the internal force vector for each model element. Calculation of the internal force values along each nodal DOF is performed using equilibrium, as depicted in Equation 2.34 to Equation 2.41.

$$f_1 = \sigma_x \times h \times t + \tau_{xy} \times w \times t \tag{2.34}$$

$$f_2 = \sigma_x \times h \times t - \tau_{xy} \times w \times t \tag{2.35}$$

$$f_3 = -\sigma_x \times h \times t + \tau_{xy} \times w \times t \tag{2.36}$$

$$f_4 = -\sigma_x \times h \times t - \tau_{xy} \times w \times t \tag{2.37}$$

$$f_5 = \sigma_y \times w \times t + \tau_{xy} \times h \times t \tag{2.38}$$

$$f_6 = -\sigma_y \times w \times t + \tau_{xy} \times h \times t \tag{2.39}$$

$$f_7 = \sigma_y \times w \times t - \tau_{xy} \times h \times t \tag{2.40}$$

$$f_8 = -\sigma_y \times w \times t - \tau_{xy} \times h \times t \tag{2.41}$$

The global DOFs of the wall model define the order of the terms in the global force vector for the wall model. Local and global DOF numbers are displayed inside and outside the model elements in Figure 2.13b, respectively. Equation 2.42 is an example of the calculation of one of the terms in the global internal force vector where superscripts indicate the model element numbers while subscripts the local internal force vector index for each model element.

$$\{F\}_{91} = \{f\}^1_{11} + \{f\}^2_{31} + \{f\}^3_{21} + \{f\}^4_{41} \tag{2.42}$$

Each term in the global internal force vector is calculated using the same procedure. As 18 global DOFs exist for this sample, the global internal force vector will be an 18x1 vector.

2.4.4. Support Conditions and Constraints

At the supports of a wall, displacement values are assigned as zero. This implies zero displacement along the DOFs of the model at the supports. The reaction forces at the supports are calculated from the equilibrium equation, using the known (zero) displacement values along the DOFs at the supports.

In addition, enforcement of constraint conditions along selected DOFs would be necessary in order to simulate the test conditions for which the wall model was experimentally validated. In this study, the wall specimens used for experimental validation of the model were cast monolithically with stiff RC load-transfer-beams, which behaved like rigid bodies during testing. Therefore, a body constraint was defined along the top DOFs of the FEM of the wall.

The aim of implementing the body constraint in the model is representation of rigid load-transfer-beams located at the top of RC wall specimens. Body constraint is implemented in the model formulation using a displacement transformation matrix [T]. The body constraint condition enforces equal horizontal displacement in the horizontal direction while relating vertical displacements to a global rotational displacement at the top of the wall through the plane-sections-remain-plane condition. The transformation matrix is a matrix that transforms an 18x18 stiffness matrix to a 15x15 stiffness matrix. Derivation of the global stiffness matrix, the global internal force vector, and the displacement vector of the sample wall after assignment of the body constraint are illustrated in Equation 2.43 to Equation 2.45. Equation 2.46 gives the result of the production of the transpose of the transformation matrix [T] with both sides of Equation 2.43.

$$[K]_{18x18} \times \{D\}_{18x1} = \{F_{unb}\}_{18x1} \tag{2.43}$$

$$[K]_{18x18} \times [T]_{18x15} \times \{D\}_{15x1} = \{F_{unb}\}_{18x1} \tag{2.44}$$

$$[T]^{T}_{18x15} \times [K]_{18x18} \times [T]_{18x15} \times \{D\}_{15x1} = [T]^{T}_{18x15} \times \{F_{unb}\}_{18x1} \tag{2.45}$$

$$\begin{array}{llll} [T]^{T}_{18x15} \times [K]_{18x18} \times [T]_{18x15} \times \{D\}_{15x1} = [T]^{T}_{18x15} \times \{F_{unb}\}_{18x1} \\ \Downarrow \qquad\qquad\qquad \Downarrow \\ [K]_{15x15} \qquad\quad \times \{D\}_{15x1} \;=\; \{F_{unb}\}_{15x1} \end{array} \tag{2.46}$$

2.4.5. Nonlinear Analysis Solution Strategy

The global stiffness matrix and the internal force vector for the wall model were derived as described in the previous sections, by integration and stiffness assembly of the model elements. In addition, support conditions and constraints were implemented in the model formulation. Next, a displacement-controlled nonlinear analysis solution strategy (Clarke and Hancock, 1990; Simons and Powell, 1982) is adopted for conducting displacement-controlled hysteretic lateral load analysis of RC walls so that model results can be correlated with results of drift-controlled lateral load tests carried out on wall specimens.

The applied strategy consists of two main stages; load incrementation and equilibrium stages. During the increment stage (denoted by "i"), the target displacements imposed on the model are incremented, whereas during the equilibrium stage (denoted by "j"), iterations are performed on the model displacements, in order to reach equilibrium. During the load incrementation stage, the target displacements imposed on the model are incremented, whereas during the equilibrium stage, iterations are performed on the model displacements, in order to reach equilibrium between the internal and external forces, within a specified tolerance. The adopted nonlinear analysis solution strategy, details of which are presented by Gullu (2013), is graphically illustrated in Figure 2.15 and Figure 2.16.

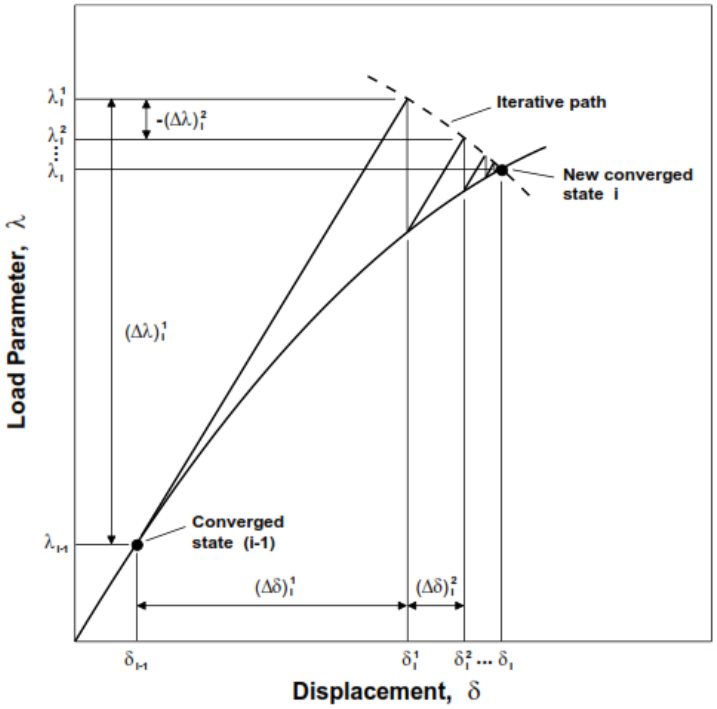

Figure 2.15. Representation of the Nonlinear Analysis Solution Strategy for a Single Degree of Freedom System (Clarke and Hancock, 1990).

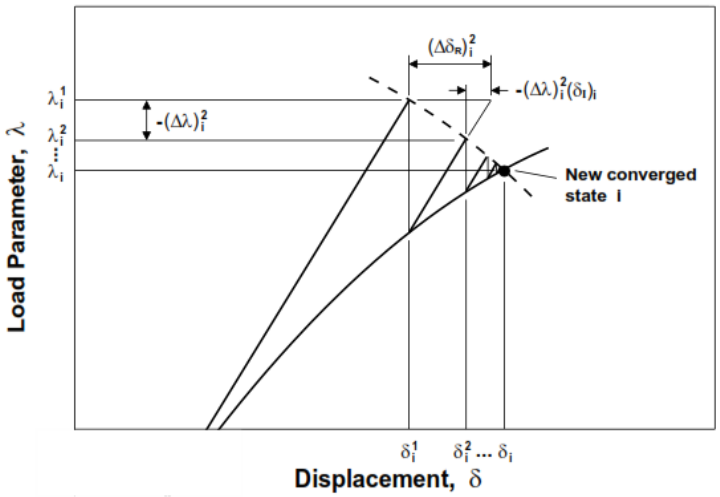

Figure 2.16. Iterative Strategy and Residual Displacements (Clarke and Hancock, 1990).

3. ANALYTICAL MODEL RESULTS AND PARAMETRIC SENSITIVITY STUDIES

3.1. General

The adopted finite element modeling methodology, together with the implemented constitutive formulations and nonlinear analysis solution strategy described in Chapter 2 were implemented in Matlab for conducting nonlinear quasi-static analyses of RC structural walls. This chapter provides a detailed discussion of the model capabilities and model response characteristics, together with sensitivity of model results to variations in wall geometry, reinforcement characteristics, and loading conditions, as well as selected model parameters and model discretization.

The moderate-aspect-ratio wall specimen RW-A15-P10-S78 tested by Tran and Wallace (2012) was used as a baseline model for evaluating the model response characteristics and for the sensitivity analyses. Detailed information on calibration of the model to represent the wall specimen, and detailed comparison of model results with test results are provided in Chapters 4 and 5. The analysis results presented in this chapter are not intended to evaluate the accuracy of the model in representing the test results, but rather to assess the model capabilities and sensitivity. Wall specimen RW-A15-P10-S78 had a rectangular cross-section (RW), aspect ratio of 1.5 (A15) with height of 1830 mm, length of 1220 mm, and thickness of 152 mm, a constant axial load of approximately 10% of the axial load capacity of the wall (P10), and a design shear stress (at flexural capacity) of 0.65 $\sqrt{f'_c}$ MPa (7.8 $\sqrt{f'_c}$ psi, S78). The specimen had a web reinforcing ratio of 0.73% in both directions and a boundary longitudinal reinforcing ratio of 6.06%. The behavior of the specimen was characterized by significant contribution of nonlinear shear deformation, contributing up to 35% of total lateral deformations, and significant shear-flexure interaction behavior (Tran, 2012).

Material models for concrete and reinforcing steel were calibrated to match the material properties of the wall specimen, as described in detail in Chapter 4. The lateral

displacement history applied at the top of the specimen during the test program was composed of force-controlled loading cycles at 1/8, 1/4, 1/2 and 3/4 of the expected yield force, followed by displacement-controlled loading cycles to drift levels of 0.5%, 0.75%, 1.0%, 1.5%, 2.0%, and 3.0%. Although multiple loading cycles to each drift were imposed during the test program, only one cycle to each drift level was enforced for the analyses presented in this chapter. As well, for the present analyses, only the drift-controlled cycles were employed. Details on the test program are provided in Chapter 4.

3.2. Analytical Model Results

The lateral load vs. top displacement response of specimen RW-A15-P10-S78 under cyclic lateral loading and constant axial load applied at the top of the wall is depicted in Figure 3.1. It can be seen from Figure 3.1 that characteristics of the overall cyclic wall behavior are represented by the model, including the overall hysteretic shape of the lateral load vs. top displacement behavior, degradation of unloading/reloading stiffness, plastic displacements at zero load level, and moderate pinching behavior.

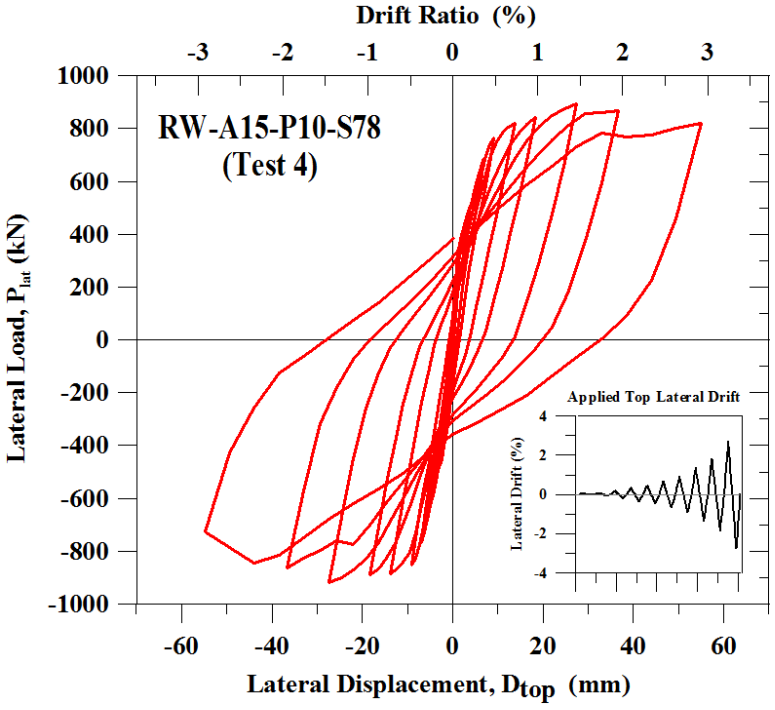

Figure 3.1. Lateral load vs. Top Displacement Response Predicted by the Model.

Analytical results presented in Figure 3.2 and Figure 3.3 illustrate lateral load vs. flexural and shear deformation contributions to top displacement, respectively. It can be deduced from the figures that model adequately captures nonlinear shear and flexural responses, as well as their interaction, since flexural and shear yielding occur near-simultaneously at a lateral load of approximately 820 kN. Highly pinched behavior is observed in the hysteretic response in shear, as expected, and it can be clearly observed in Figure 3.2 that the shape of the hysteretic loops for flexural behavior show minimal pinching behavior, and therefore, the pinched shear behavior produces the moderate pinching observed in the overall lateral load-displacement response. Figure 3.3 also indicates that the relative contribution of shear deformation to wall displacement at the top is approximately 30-40%, which successfully captures test results (contributing by 35% to lateral displacement, as will be shown in Chapter 5), whereas Figure 3.2 shows that flexural deformations contribute by approximately 60-70% to the lateral displacement of the wall, throughout the cyclic loading history.

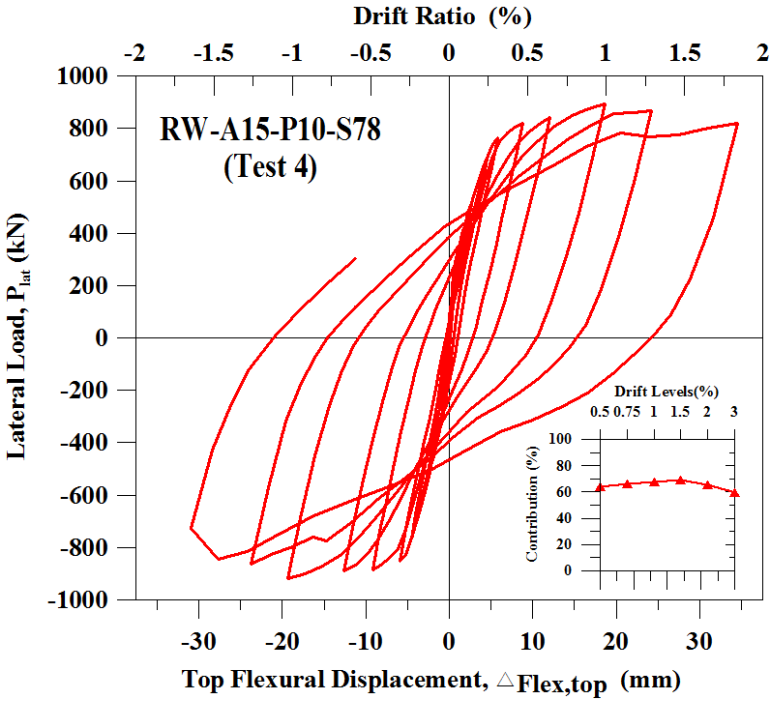

Figure 3.2. Load vs. Flexural Top Displacement Response Predicted by the Model.

Figure 3.4 illustrates the profiles (distribution) of lateral displacements over the wall height, at applied drift levels of 0.5%, 0.75%, 1.0%, 1.5%, 2.0% and 3.0%, whereas

corresponding shear and flexural displacement profiles and their contributions to total displacement are shown in Figure 3.5. Displacement profiles were obtained at elevations of 610 mm, 1220 mm, and 1830 mm along wall height.

It can be observed in Figure 3.4 that the total displacement profiles along wall height are almost linear at low drift levels, whereas for larger drifts, total displacements are higher at the bottom of the wall up to a height of approximately $l_w/2$ (610 mm). This concentration of nonlinear deformations can be also observed in Figure 3.5, which shows that shear and flexural deformation profiles are also nonlinear up to the wall height of about $l_w/2$, whereas along the rest of the wall height, the profiles are almost linear.

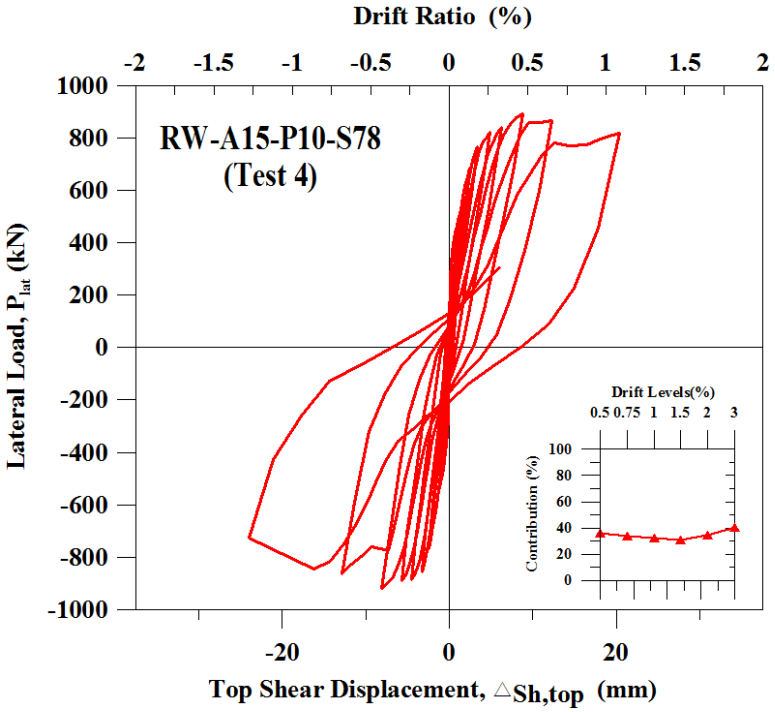

Figure 3.3. Load vs. Shear Top Displacement Response Predicted by the Model.

It can also be deduced from Figure 3.5 that relative contributions of shear deformations to lateral displacement are dominant at the bottom of the wall. Their Predicted shear deformation contribution to the total lateral displacement ranges from 60% at bottom of the wall to 34% at top of the wall, indicating larger nonlinear shear deformations along the lower part of the wall compared to nonlinear flexural deforma-

tions, due to shear-flexure interaction behavior.

The predicted relationship between the vertical growth (upward vertical displacement at the wall centroid) due to yielding of longitudinal reinforcement and migration of the neutral axis) and the lateral displacement at the top of the wall is shown in Figure 3.6, which reveals that the model predicts consistently increasing vertical growth of the wall throughout the loading history. At larger drift levels, since the strains in longitudinal reinforcement increase more rapidly, the rate of vertical displacement (growth) increases, as expected.

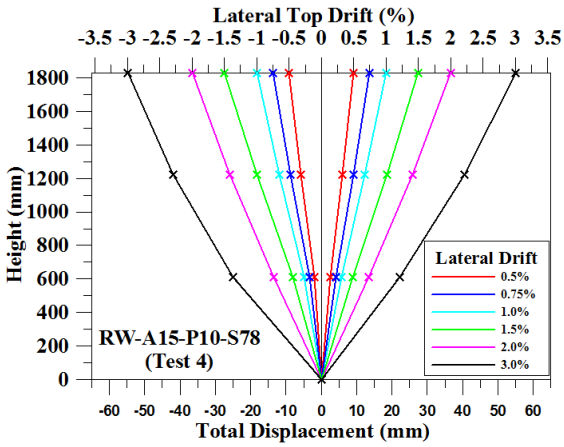

Figure 3.4. Total Displacement Profiles.

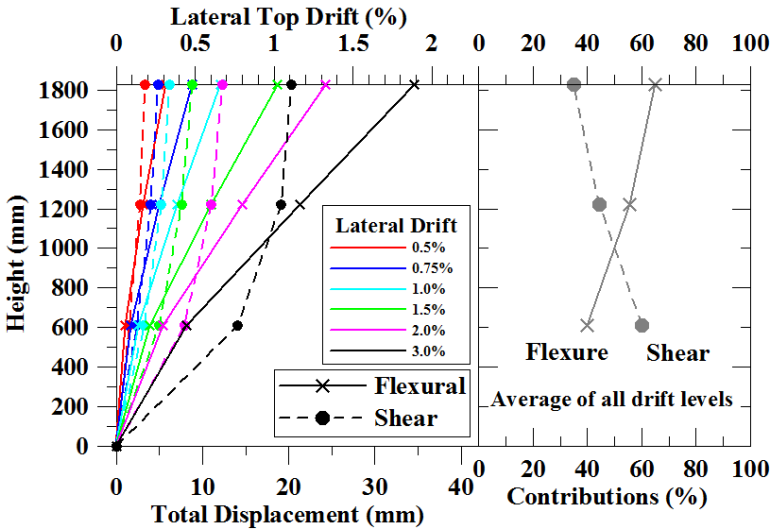

Figure 3.5. Shear and Flexural Displacement Profiles with Contributions to Total Displacement.

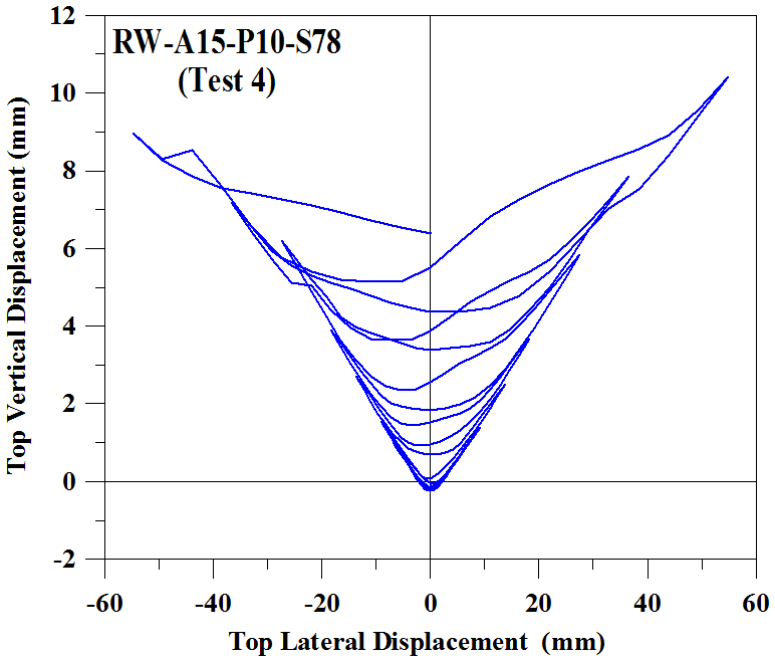

Figure 3.6. Vertical Growth versus Lateral Displacement.

3.3. Sensitivity of Model Response to Wall Configurations and Model Parameters

Variation of model results to different wall aspect ratios, reinforcement amounts, levels of axial load, model discretization, and selected shear aggregate interlock coefficients are presented in this section in order to demonstrate the model response sensitivity to such parameters and to illustrate the capabilities of the model in predicting the response of RC walls with various behavioral modes and failure mechanisms.

As mentioned earlier, specimen RW-A15-P10-S78 (Tran and Wallace, 2012) is used as the baseline model for the sensitivity studies. Detailed calibration of the model for wall geometry and material parameters are described in Chapter 4.

3.3.1. Wall Aspect Ratio

In order to investigate the sensitivity of model predictions to wall aspect ratio, the wall configuration used for previous analyses (representing specimen RW-A15-P10-S78,

with aspect ratio of 1.5) was "shortened" to an aspect ratio of 1.0, and "elongated" to aspect ratios of 2.0 and 3.0, while maintaining cross-sectional dimensions and reinforcement characteristics. Each wall configuration was analyzed under the cyclic loading protocol defined in Section 3.1. Figure 3.7 compares the model results obtained for the four considered aspect ratios of 1.0, 1.5, 2.0 and 3.0. Predicted wall lateral load vs. deformation responses can be distinguished by the lateral load capacity prediction, the shape of the overall lateral load vs. top displacement response, and the contribution of shear deformation to wall lateral displacement. For the short wall with an aspect ratio of 1.0 (Figure 3.7a), the overall lateral load vs. displacement response reflects characteristic shear-dominated (pinched) hysteretic loops, which is consistent with the large contribution of shear deformation to wall lateral displacement (more than 70%), as shown in Figure 3.8. In contrast, for the more slender wall configurations with aspect ratios of 2.0 and 3.0 (Figure 3.7c and Figure 3.7d), the overall load-displacement response possesses wide hysteretic loops and almost no pinching, similarly to the shape of the flexural load-displacement responses shown in Figure 3.9c, d, implying that flexural deformation contributes significantly to lateral displacement, and the contribution of shear deformations is relatively small (limited to approximately 20% and 10%, respectively, as shown in Figure 3.8c, d). The predicted response of the wall with the intermediate aspect ratio of 1.5 (baseline model, Figure 3.7b) differs from the walls with aspect ratios of 1.0 and 2.0 in terms of the pinching characteristics of the response and contribution of shear deformations to lateral displacement, as moderately-pinched hysteresis loops were obtained and the contribution of shear deformations to lateral displacement is approximately 35%. As expected, the lateral load capacities estimated for the four walls decrease with increasing aspect ratios.

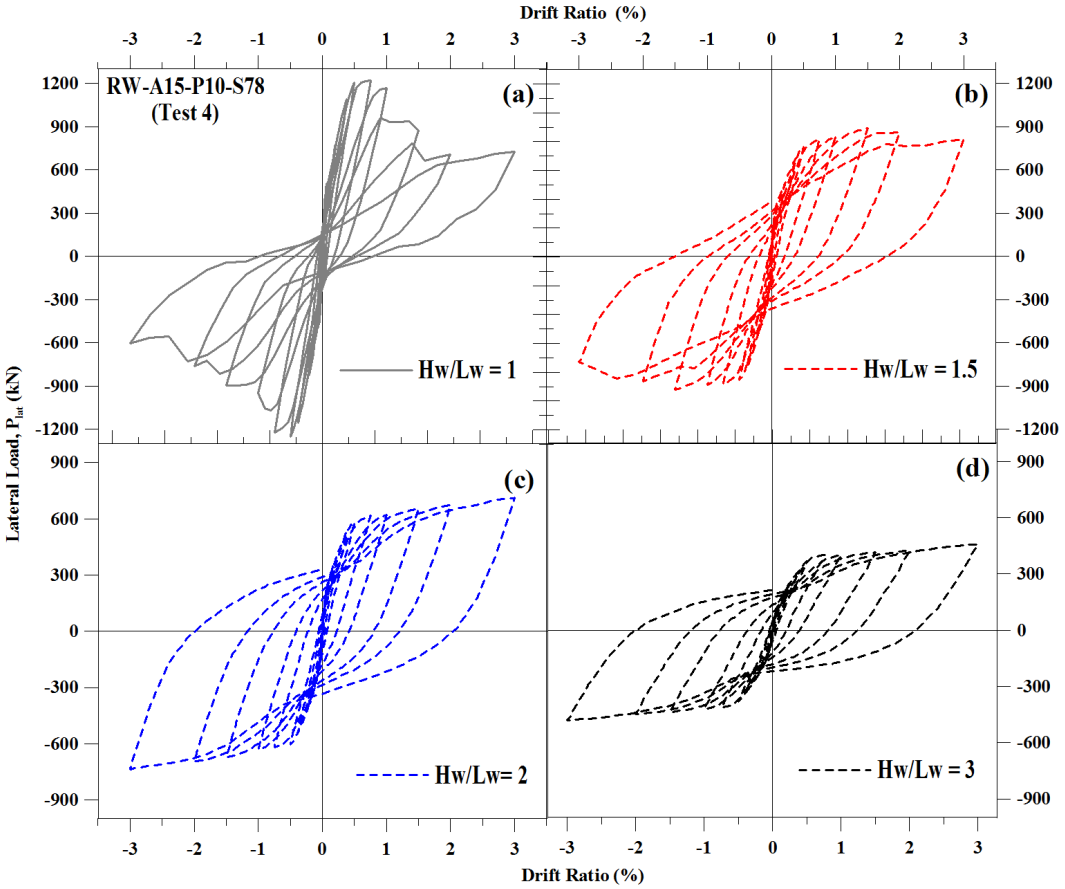

Figure 3.7. Sensitivity of Predicted Response to Wall Aspect Ratio (h_w/l_w).

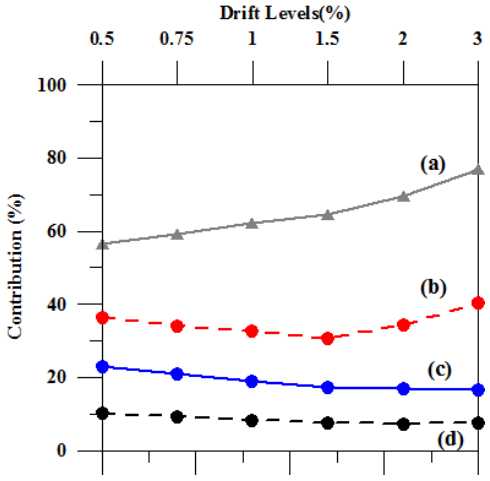

Figure 3.8. Contribution of Shear Deformation to Top Displacement, for Different Wall Aspect Ratios.

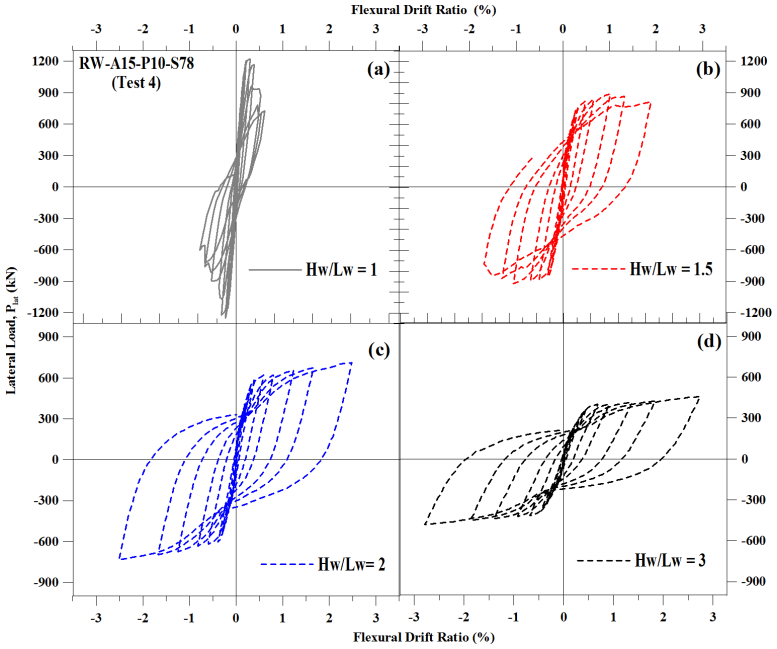

Figure 3.9. Sensitivity of Predicted Flexure Response to Wall Aspect Ratio (h_w/l_w).

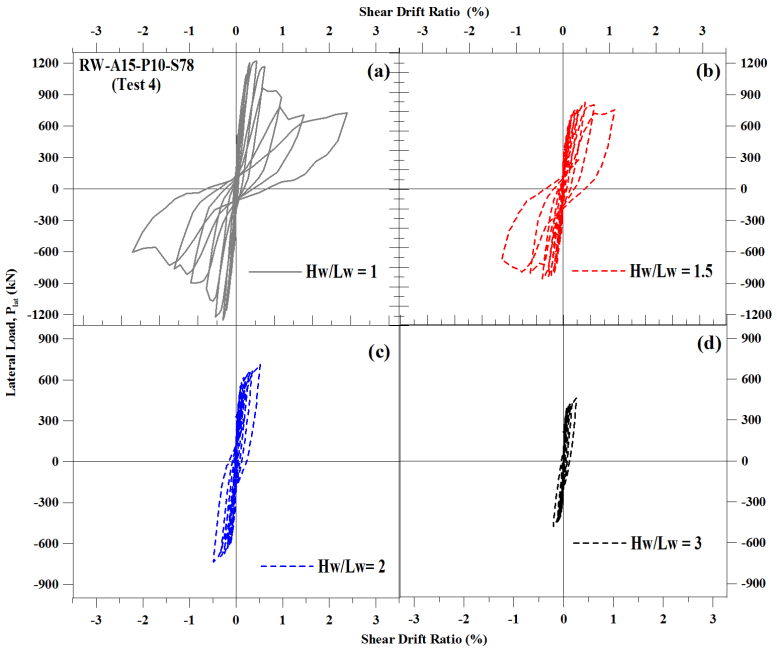

Figure 3.10. Sensitivity of Predicted Shear Response to Wall Aspect Ratio (h_w/l_w).

3.3.2. Reinforcement Ratio

The sensitivity of the model response to the web reinforcement ratio (ρ_{web}) and the boundary vertical reinforcement ratio (ρ_b) of the wall were also investigated in

order to evaluate whether the model can capture different modes of behavior and different flexural and shear deformation contributions to the response, depending on relative nominal flexural and shear capacities of the wall. For this purpose, the web reinforcement ratio of the wall configuration was reduced to half of its original value (0.73% to 0.36%), and the vertical boundary reinforcement was reduced to half of its initial value (6.06% to 3.03%). Figure 3.11 illustrates the influence of decreasing the web reinforcement ratio, and vertical boundary reinforcement ratio on the lateral load vs. displacement response of the wall. As depicted in the figure, decreasing the reinforcement ratio of the wall results in a reduced lateral load capacity prediction for the wall. Larger shear deformation contribution is obtained when web reinforcement ratio is reduced and smaller shear deformation contribution is predicted when boundary vertical reinforcement ratio is reduced, as shown in the figure. Therefore, the model successfully considers the influence of the amount of the web and vertical reinforcement (or nominal shear and flexural capacities) on the overall response of the wall, as well as the relative magnitude of nonlinear flexural and shear deformations developing in the wall.

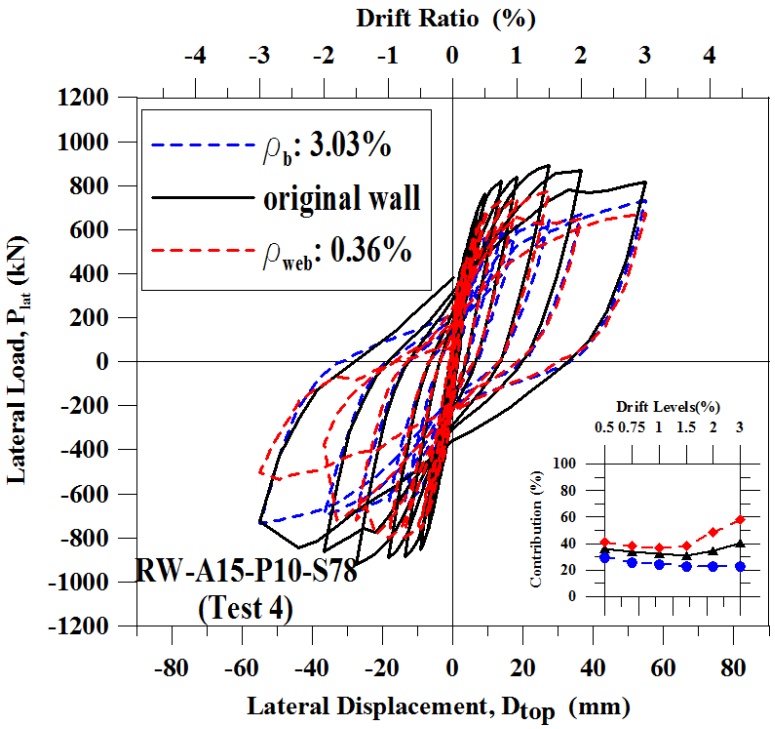

Figure 3.11. Sensitivity of Predicted Response to Wall Reinforcement.

3.3.3. Axial Load

Another sensitivity analysis on the model results was conducted by varying the axial load level applied on the baseline wall model. As shown in Figure 3.12, axial load levels of 0%, 5%, 10% (original axial load level), 15%, and 20% of the wall axial capacity ($A_g f'_c$) are applied in order to assess the influence of applied axial load level on the predicted response. As illustrated in Figure 3.12, changing the axial load level significantly influences the overall behavior of the wall. Larger lateral load capacity, less ductility, and more pronounced pinched behavior are observed for increasing axial load levels, as expected. The model successfully incorporates the influence of axial load on the response prediction.

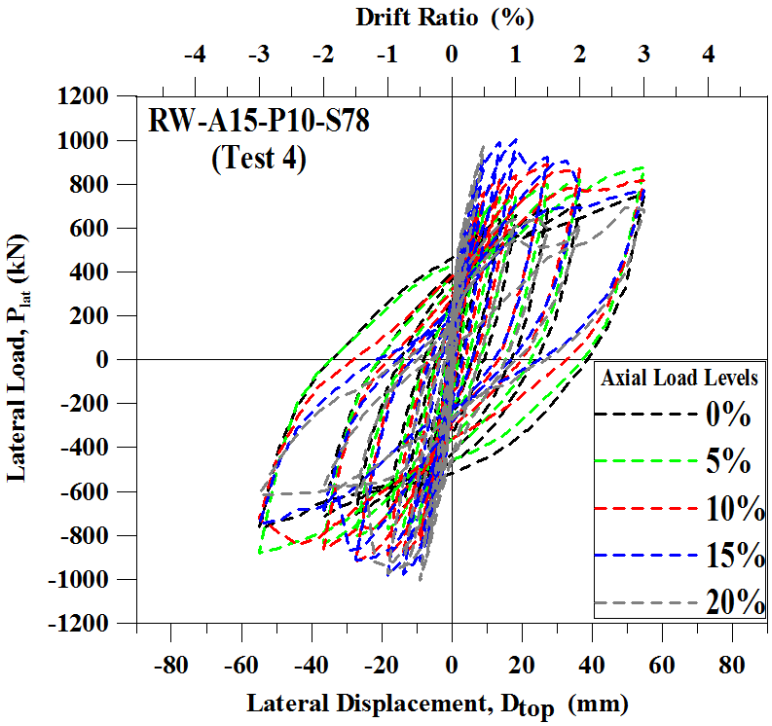

Figure 3.12. Sensitivity of Predicted Response to Axial Load Level.

3.3.4. Shear Resisting Mechanism of RC Panel Model

The sensitivity of model predictions to the parameters of the constitutive shear aggregate interlock models (concrete compressive stress friction coefficient η_c, steel clamping effect friction coefficient η_{st}) is illustrated in Figure 3.13. Analytical results

were obtained for six different yet reasonable η_c and η_{st} pairs, which are η_c =1-η_{st} =1, η_c =1-η_{st} =0.5(were used in calibration of the model), η_c =0.5-η_{st} =1, η_c =0.5-η_{st} =0.5, η_c =1.5-η_{st} =1 and η_c =1.5-η_{st} =0.5. As discussed in Chapter 2, η_c =1 and η_{st} =0.5 are the recommended values in this study, based on previous experimental results on squat walls and available literature on the subject. It can be seen in Figure 3.13 that reasonable variation in these parameters does not significantly alter the model response for this particular moderate-aspect-ratio wall. However, reliable aggregate interlock parameters should be valid for all wall configurations (slender, medium-rise and squat walls). Previous modeling studies on walls (Gullu, 2013, Orendil, 2014) indicates that the recommended values (η_c =1 and η_{st} =0.5) are also suitable for slender and squat walls.

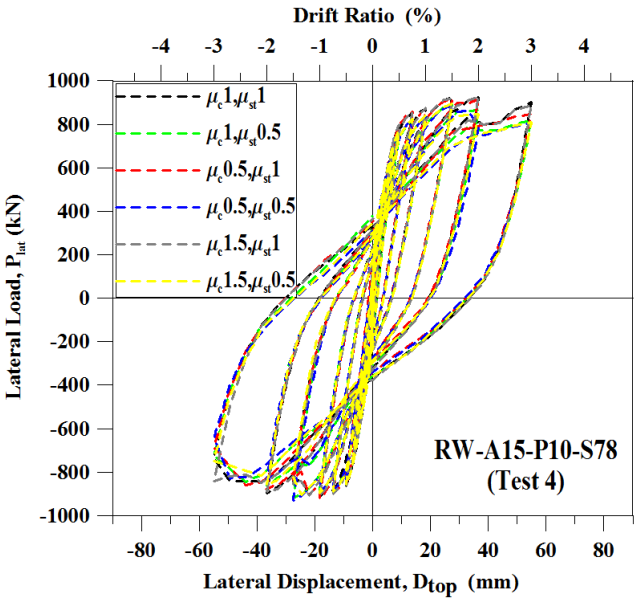

Figure 3.13. Sensitivity of Predicted Response to Shear Aggregate Interlock Parameters.

3.3.5. Number of Model Elements

The number of model elements (m - number of model elements along wall length and n - number of model elements along wall height) used for modeling of the wall specimen RW-A20-P10-S78 was varied. Model results were obtained for four different m and n pairs which are m=6, n=9 (baseline model); m=6, n=18; m=12, n=9; and

m=12, n=18. These configurations were selected to evaluate the influence of model discretization on the predicted response. As shown in Figure 3.14, using different discretizations moderately influences the global response prediction of the model. By increasing the number of model elements in the vertical direction (n), degradation at large drift levels is more pronounced. Furthermore, by increasing the number of model elements in the horizontal direction (m), slightly larger shear deformations were observed. The height and length of the wall specimen are 1830 mm and 1220 mm, respectively. Therefore, m=6, n=9 and m=12, n=18 couples result in model elements with approximately square geometry. It can observed in Figure 3.14 that larger lateral load capacity and less pronounced degradation is obtained when non-square-geometry (high aspect ratio) model elements are used. The number of model elements does not result in significant change in the stiffness and pinching behavior in the analytical results.

In addition to comparison of global (load-displacement) response predictions, sensitivity of the vertical strain distributions along wall length to the number of model elements were investigated. Comparison of the predicted profiles of vertical strains along wall length at the bottom of the wall, corresponding to lateral drifts of 0.5%, 0.75%, 1.0%, 1.5% and 2.0%, are presented for m=6, n=9 (baseline model); m=6, n=18; m=12, n=9; and m=12, n=18 in Figures 3.15 to 3.17. The predicted strain profiles are constructed using vertical strains at 0 mm, 203 mm, 406 mm, 609 mm, 813 mm, 1016 mm, and 1220 mm along the length of the wall for m=6; and at 0 mm, 102 mm, 203 mm, 305 mm, 406 mm, 508 mm, 609 mm, 711 mm, 813 mm, 914 mm, 1016 mm, 1117 mm, and 1220 mm along the length of the wall for m=12, along a height of 40.6 cm from the bottom of the wall for all cases.

It can be deduced from the comparisons that the vertical strain profiles predicted by the baseline model with m=6 and n=9 shows unexpected fluctuations. By increasing the number of model elements in vertical or horizontal directions, the fluctuations disappear and consistent profiles are obtained, with comparable strain magnitudes. Considering both global and local response predictions of the model, the discretization with 12 model elements along wall length (m=12) and 18 model elements along wall

height (n=18) produces the optimum results. Therefore, this model discretization was used for comparison of model results with test results presented in Chapter 5.

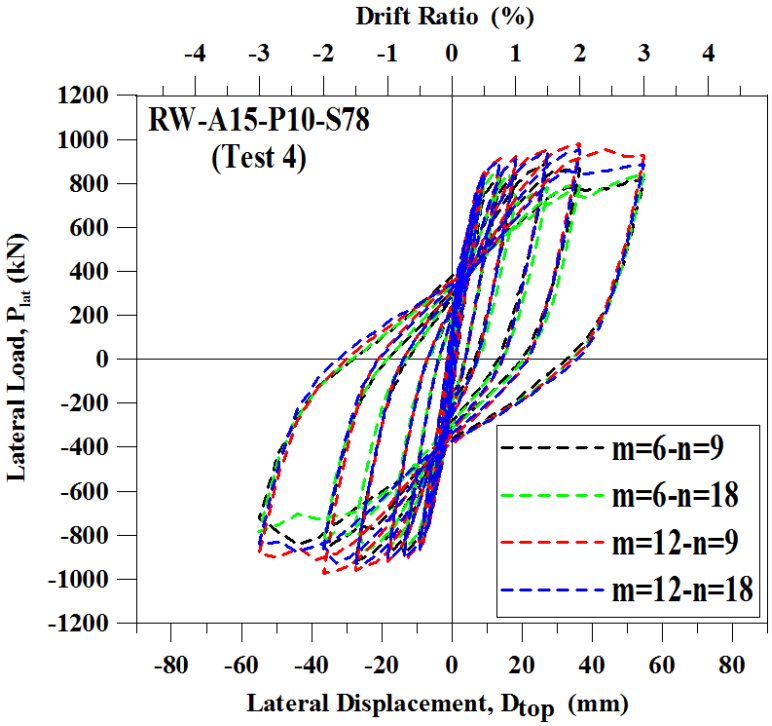

Figure 3.14. Sensitivity of Predicted Response to Number of Model Elements.

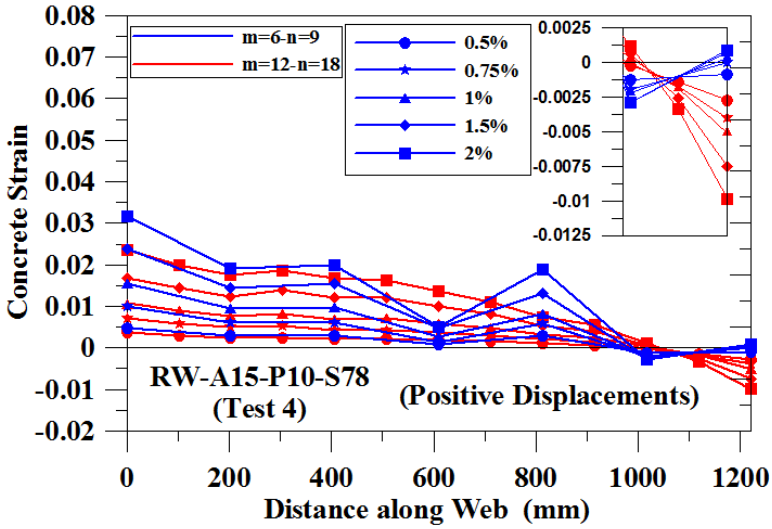

Figure 3.15. Vertical Strain Profiles for m=6 - n=9 and m=12 - n=18.

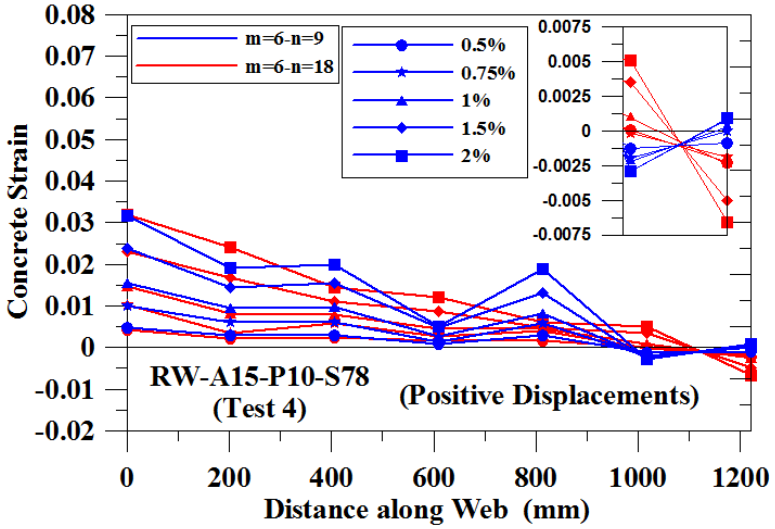

Figure 3.16. Vertical Strain Profiles for m=6 - n=9 and m=6 - n=18.

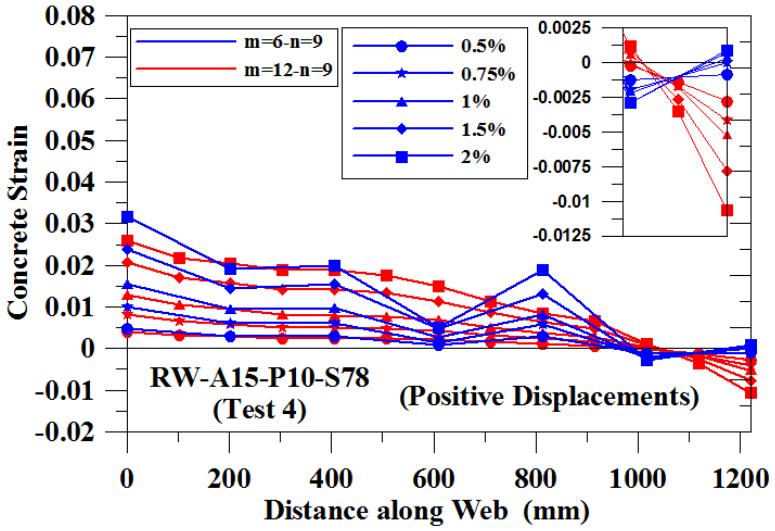

Figure 3.17. Vertical Strain Profiles for m=6 - n=9 and m=12 - n=9.

3.4. Overview

A detailed evaluation of the model response characteristics and sensitivity of the model results to variations in wall configuration and selected model parameters were presented in this chapter. Lateral load vs. top displacement, lateral load vs. flexural and shear deformations, lateral displacement profiles and vertical growth predictions of the model were presented to show the model response attributes. Sensitivity of the model results to wall aspect ratio, reinforcement amount, axial load level, shear

aggregate interlock parameters, and model discretization were also presented.

It was observed that increasing the wall aspect ratio caused the predicted response to become more flexural-dominant, as expected. Decreasing the reinforcement ratio on the web and boundary regions resulted in the increase and decrease of predicted shear deformation contributions, respectively, together with decrease in the predicted lateral load capacity, also as expected. By increasing the axial load level, larger lateral load capacity and more pronounced pinching behavior was observed, as is typical. The model results showed behaviorally-consistent and systematic sensitivity to all of these variations in wall configuration.

Varying the parameters of the constitutive shear aggregate interlock models (within reasonable range) did not noticeably alter the model predictions. However, changing the number of model elements resulted in significant variation in the predicted vertical strain profiles, indicating that a reasonably fine model discretization must be used in order to obtain reliable local deformation predictions. As well, using model elements with approximately square geometry were observed to give better response estimates. For the 1.5-aspect-ratio specimen investigated, using 12 model elements along wall length and 18 model elements along wall height was deemed adequate.

4. EXPERIMENTAL CALIBRATION OF THE MODEL

In order to simulate the hysteretic lateral load behavior of the five rectangular RC wall specimens tested by Tran and Wallace (2012), the finite element formulation involving the constitutive material and behavioral models described in Chapter 2 were implemented in Matlab. In this chapter, the experimental program and experimental calibration of the model for representing the characteristics of the wall specimens and the loading conditions are presented. Within the scope of the experimental program conducted by Tran and Wallace (2012), five 1/3 scale cantilever RC wall specimens were tested under combination of constant axial load and reversed cyclic lateral load imposed at the top of each wall. Specimens were designed and tested in the Structural/Earthquake Engineering Research Laboratory (SEERL) at the University of California Los Angeles (UCLA). The primary objectives of the test program were to investigate the impact of the level of axial stress and the level of average shear stress at flexural capacity, on wall failure modes and lateral deformation capacity, as well as to assess the distribution and magnitude of lateral deformations associated with shear and flexure. The primary test variables included wall aspect ratio (1.5 and 2.0), axial load level (0.025 and 0.10), and wall shear stress level at flexural yielding (between approximately 0.33 and 0.66 MPa). An overview of specimen design, materials, test setup and instrumentation is presented in the following sections, whereas detailed information can be found in the Ph.D. Thesis by Tran (2012).

4.1. Description of the Wall Specimens

Five 15 cm thick and 122 cm long RC wall specimens were subjected to lateral loads applied at either 183 cm or 244 cm - depending on the target aspect ratio -above the wall-pedestal interface. For the first four specimens, the axial load level was 0.10 $A_g f'_c$, whereas for the fifth specimen it was 0.025 $A_g f'_c$. A_g. Here, A_g is the gross cross-section area of shear walls and f'_c is the specified concrete compressive strength. The horizontal and vertical web reinforcement ratios satisfy (i.e. are higher than) the minimum ratio of 0.0025 specified in ACI 318-11 Ch. 21. The ductility of the specimens

is ensured such that flexural yielding occurs before the nominal shear strength per ACI 318-11 is reached. The details of the test specimens are provided in Table 4.1, a typical wall cross section is shown in Figure 4.1, and wall reinforcement details are summarized in Table 4.2, The minimum and maximum ratios of vertical boundary reinforcement ρ_b for the five test specimens are 3.23% and 7.11%.

Table 4.1. Test Specimens Details.

Test No.	Specilen code	$\frac{h_w}{l_w}$	$\frac{P_{ax}}{A_g f'_c}$		Web Reinforced		Boundary Reinforced		$\frac{V@M_n}{V_n}$		$\frac{V@M_n}{A_{cv}\sqrt{f_c}}$	
			des.	act.	$\rho_t = \rho_l$ (%)	configuration	ρ_b (%)	conf.	des.	act.	des.	act.
1	RW-A20-P10-S38	2	0.1	0.07	0.27	6D6 @ 140 mm	3.23	8#4	0.8	0.81	3.8	3.6
2	RW-A20-P10-S63		0.1	0.07	0.61	5#3 @ 152 mm	7.11	8#6	0.88	0.91	6.3	6.1
3	RW-A15-P10-S51	1.5	0.1	0.08	0.32	7D6 @ 114 mm	3.23	8#4	0.8	0.83	5.1	4.9
4	RW-A15-P10-S78		0.1	0.06	0.73	6#3 @ 127 mm	6.06	4#6+ 4#5	0.84	0.85	7.8	7
5	RW-A15-P2.5-S64		0.03	0.02	0.61	5#3 @ 152 mm	6.06	4#6+ 4#5	0.79	0.79	6.4	5.8

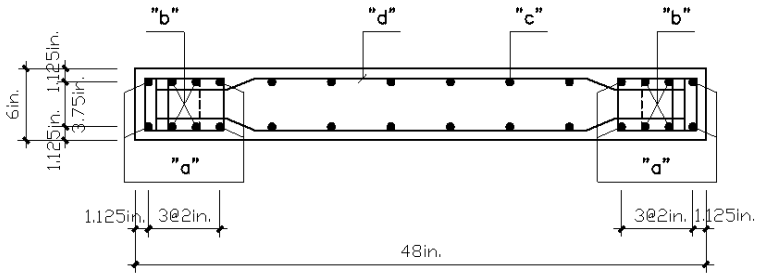

Figure 4.1. Typical Wall Cross-Section.

Table 4.2. Wall Reinforcement Details.

Wall specimen	"a"	"b"	"c"	"d"
RW-A20-P10-S38	4#4	4#4	6D6a @ 140 mm	D6b @ 140 mm
RW-A20-P10-S63	4#6	4#6	5#3 @ 152 mm	#3 @ 152 mm
RW-A15-P10-S51	4#4	4#4	7D6a @ 114 mm	D6b @ 114 mm
RW-A15-P10-S78	4#6	4#5	6#3 @ 127 mm	#3 @ 127 mm
RW-A15-P2.5-S64	4#6	4#5	5#3 @ 152 mm	#3 @ 152 mm

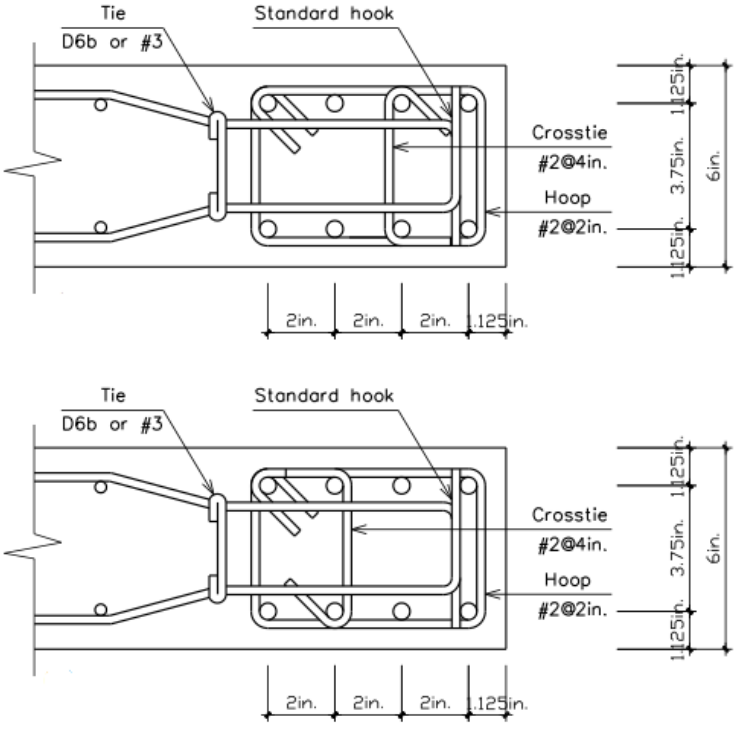

Figure 4.2. Wall Boundary Zone Detailing (Tran, 2012).

All five of the specimens required special boundary elements according to the ACI 318-11 Section 21.9.6 specifications. Since the specimens were designed and de-

tailed per ACI 318-11, the transverse reinforcement detailing of the boundaries was conforming. Figure 4.2 represents a typical wall boundary zone detailing used on the specimens. Within the wall boundaries, a hoop and a single crosstie were used at each level along the height (both #2 bars, d_b=6.35 mm). The configuration of the crossties were staggered, i.e., the crossties were alternated between the longitudinal reinforcement pairs and two successive crossties in heightwise are not lined up as shown in Figure 4.2. One end of a crosstie has a 90-degree hook while the other has 135-degree hook and are arranged interchangeably per ACI 318-11 Section 21.6.4.2 (Figure 4.2).

4.2. Test Setup and Instrumentation

The cantilever wall specimens were tested in an upright position. The reversed cyclic lateral load was applied by an 890 kN hydraulic actuator attached to the top of the wall specimens, while the vertical load was applied on the specimens by using two 100-ton hollow cylinders. The lateral load was applied on a top loading beam to ensure that the load was distributed uniformly along the top of each specimen. Testing was continued until loss of lateral and axial load capacity was observed during each test. A schematic of the test setup is presented in Figure 4.3.

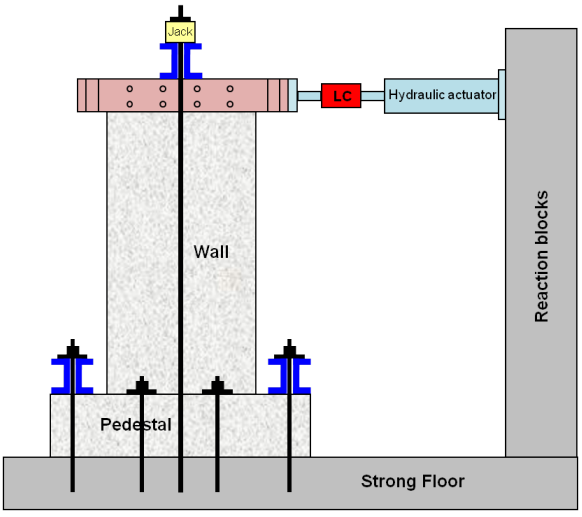

Figure 4.3. Scheme of Test Setup (Tran, 2012).

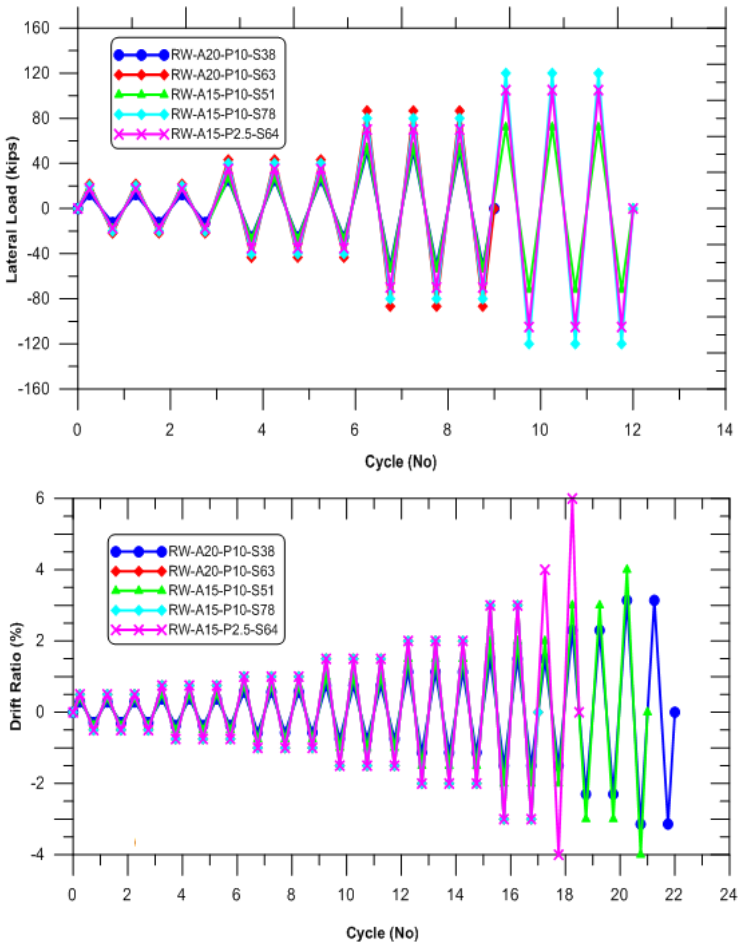

Figure 4.4. Loading Protocols (Tran, 2012): (a) Force Controlled, (b) Displacement Controlled.

The testing protocol consisted of load-controlled cycles followed by displacement-controlled cycles. Load-controlled cycles generally consisted of cycles at 1/8, 1/4, 1/2, and 3/4 of the expected yield force (Figure 4.4a), after which the testing protocol was switched to displacement-controlled cycles for the remainder of each test. Displacement-controlled cycles were typically performed at lateral drift ratios of 0.5%, 0.75%, 1.0%, 1.5%, 2.0%, 3.0%, and 4.0% (Figure 4.4b), with slight differences in the applied drift history for drift levels beyond 3.0%. Force and drift controlled loading protocols for all five wall specimens are presented in Figure 4.4.

4.3. Instrumentation and Data Acquisition

In order to collect detailed response information, the wall specimens were heavily instrumented. Wall pedestal sliding and uplift, lateral wall displacements varying over the height (incorporating flexural, shear, and sliding shear components), and average concrete strains over specified gauge lengths were computed from the data gathered by Linear Variable Differential Transformers (LVDTs). Figure 4.5 and Figure 4.6 show the sensor configuration used for specimens #1, #2, #3, and #4, #5, respectively.Within a $l_w/2$ portion of the height measured from the wall-pedestal interface, 30 strain gauges were attached to the reinforcing bars at various locations, including horizontal and transverse reinforcement of both the web and the boundary regions. For the test specimens, the arrangement of the strain gauges on the transverse reinforcement in the boundary region (hoops and cross-ties) can be seen in Figure 4.7. Similarly, the arrangement of the strain gauges for the remaining reinforcement (longitudinal in boundary regions, longitudinal and horizontal in web region) is illustrated in Figure 4.8.

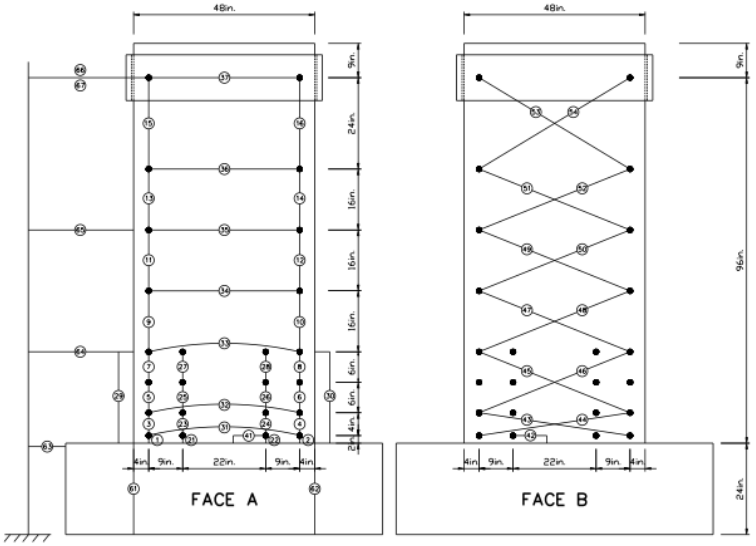

Figure 4.5. Sensor Configuration for Specimens #1 and #2 (Tran, 2012).

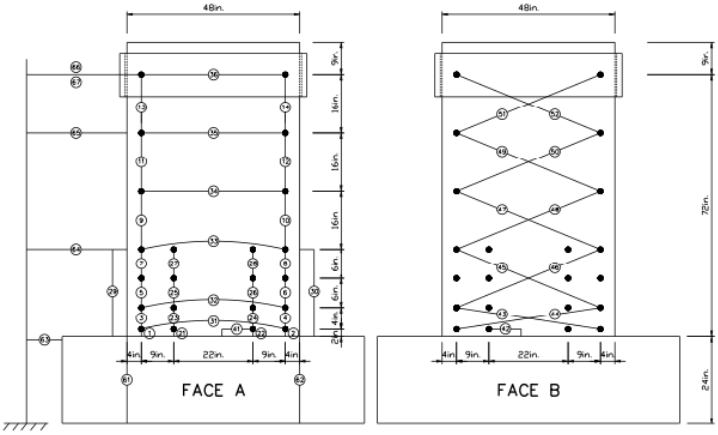

Figure 4.6. Sensor Configuration for Specimens #3, #4, and #5 (Tran, 2012).

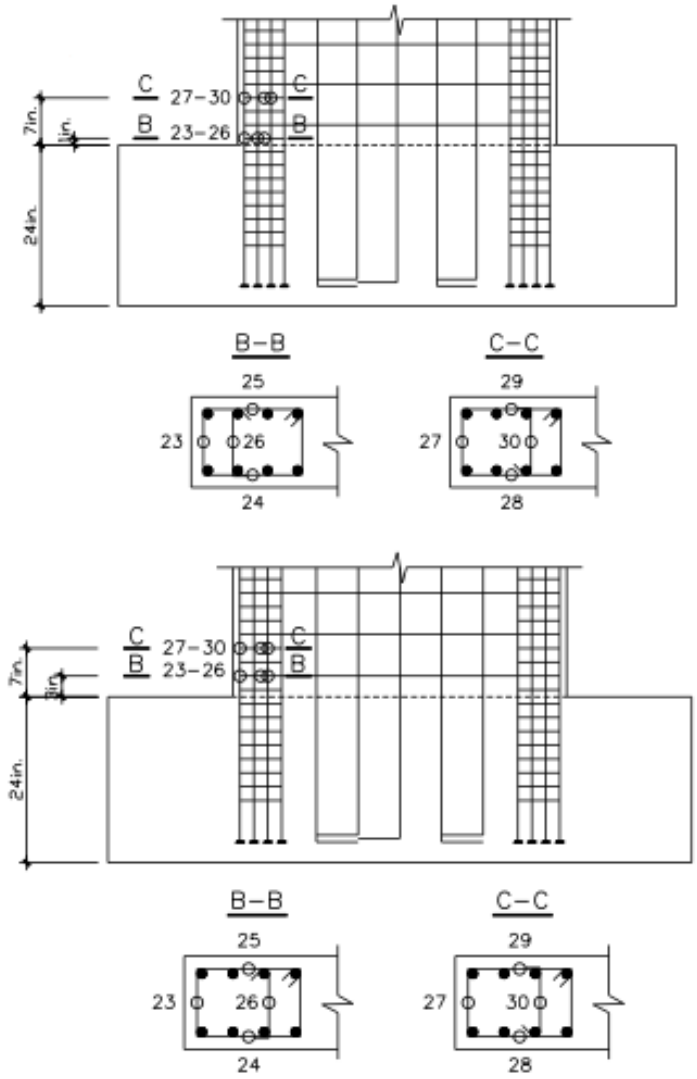

Figure 4.7. Strain Gage Location in Boundary Transverse Reinforcement: Tests 1 and 3.

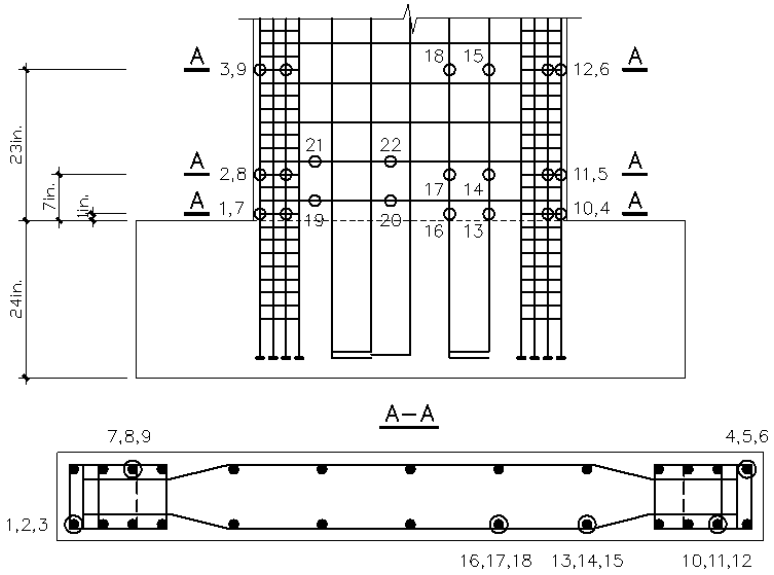

Figure 4.8. Strain Gauge Location in Vertical and Horizontal Reinforcement (Tran, 2012).

4.3.1. Total Displacement Calculation

During processing of the experimental data, displacement sensors in wall longitudinal direction and sensors installed on the walls in "X" configuration were used in combination for calculation of total lateral deformation, flexural deformation, and shear deformation along wall height. Deformation profiles were obtained at maximum top displacement displacement points under positive and negative loading directions for the first loading cycles at each target drift level. Total lateral deformations (displacements) were calculated along wall height as shown in Figure 4.9.

Based on measurements from these sensors, total lateral displacement was obtained as:

$$\Delta_{total} = \frac{\sqrt{(d_1 + D_1)^2 - (h + V_2)^2} - \sqrt{(d_2 + D_2)^2 - (h + V_1)^2}}{2} \tag{4.1}$$

where d_1 and d_2 are original lengths of the two diagonal sensors, D1 and D2 are displacements measured by these diagonal sensors, h is the height of the wall segment, and V_1 and V_2 are displacements measured by the vertical sensors (Figure 4.9).

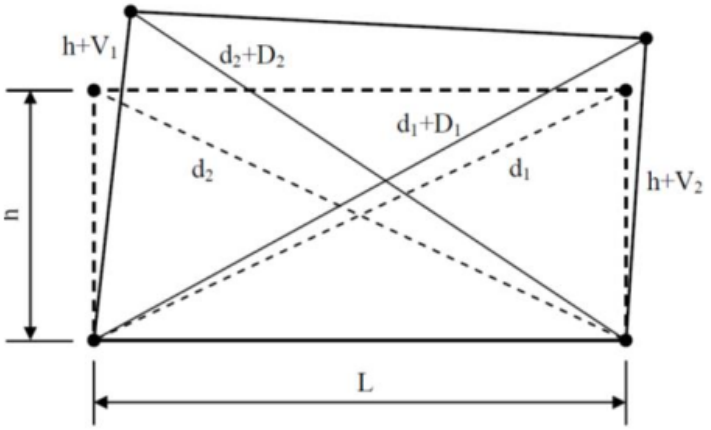

Figure 4.9. Deformation of a Wall Segment (Tran, 2012).

4.3.2. Flexural Component of Lateral Displacement Calculation

Flexural displacements of a wall section of height h are derived from the definition of the location of center of curvature distribution as:

$$\alpha h = \frac{\int_0^h \Phi x dx}{\int_0^h \Phi dx} = \frac{\Delta_f}{\theta} \Rightarrow \Delta_f = \alpha \theta h \tag{4.2}$$

where Δ_f is the flexural lateral displacement at the top of the wall section, α is the relative distance from the top of the wall section to the centroid of the curvature diagram, h is the height of the wall section, θ is the rotation at the top of the wall section, and $\Phi = \Phi_{(x)}$ is the curvature of the wall section at location x (Figure 4.10).

The rotation θ at the top of the wall segment is obtained as:

$$\theta = \frac{V_1 - V_2}{L} \tag{4.3}$$

where V_1 and V_2 are vertical displacements measured from two lines of vertical sensors near the wall edges, and L is the horizontal distance between the sensors. Details on calculation of flexural displacements from the experimental data can be found in the Thesis by Tran (2012).

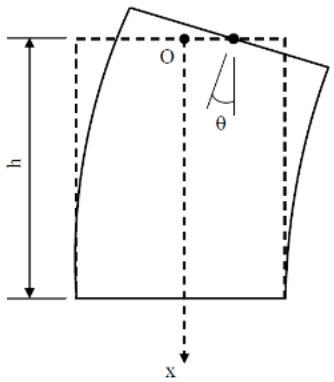

Figure 4.10. Calculation of Flexural Deformation for a Wall Section in Experiment (Tran, 2012).

4.3.3. Shear Component of Lateral Displacement Calculation

Shear deformations were obtained directly from the sensors in "X" configuration as:

$$\Delta_s = \frac{\sqrt{(d_1 + D_1)^2 - h^2} - \sqrt{(d_2 + D_2)^2 - h^2}}{2} \tag{4.4}$$

where d_1 and d_2 are original lengths of the two diagonal sensors, D1 and D2 are displacements measured from these diagonal sensors, h is the height of the wall section, as shown in Figure 4.11.

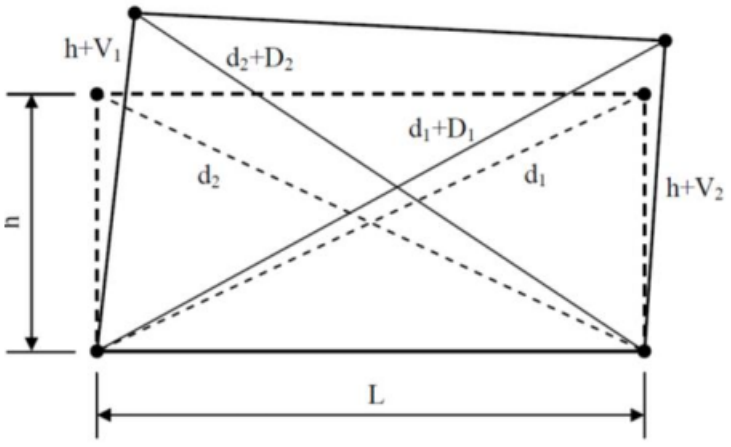

Figure 4.11. Deformations of Wall Segment.

To evaluate the consistency of the measurements, lateral shear deformation along a wall segment (Δ_s) was also calculated by subtracting the flexural (Δ_f) and sliding shear (Δ_{sld}) deformations from the total lateral deformation (Δ_{total}) as:

$$\Delta_s = \Delta_{total} - \Delta_f - \Delta_{sld} \tag{4.5}$$

4.4. Material Properties

The concrete used for the wall was designed to have a compressive strength of 34.5 MPa. For each wall, three 15.2x30.5 cm concrete cylinder specimens were tested at the UCLA material testing laboratory. The stress-strain curves and the average values of peak concrete compressive stress f'_c and corresponding concrete strain ε'_c for the five wall specimens are provided in Figure 4.12. Once the concrete strength degradation starts, the concrete cylinder specimen behaves in an unstable manner. For this reason, it can be observed from Figure 4.12 that the curves terminate at the peak since the post-peak portion could not be recorded reliably. Average concrete compressive strength and the corresponding strain value at the test day, the test date of the wall, and test date of the cylinders for all five specimens are listed in Table 4.3.

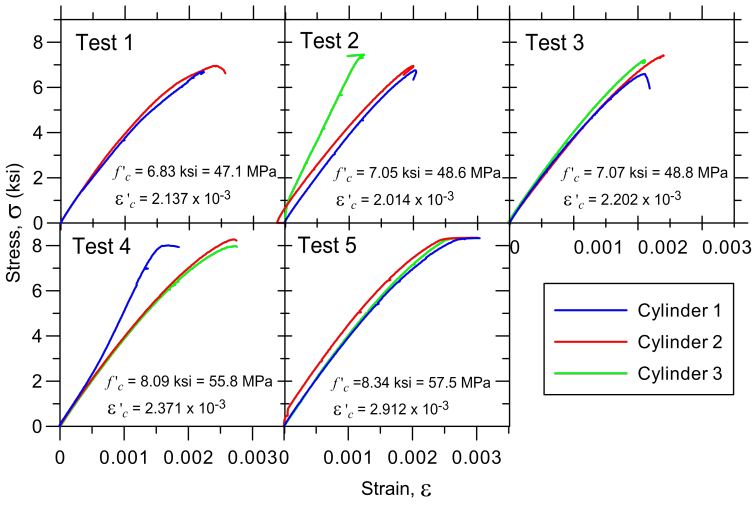

Figure 4.12. Concrete Cylinder Stress-Strain Relationships for Tests 1 to 5.

Table 4.3. Average Compressive Strength of Concrete at the Day of Testing (Tran, 2012).

No.	Specimen	Wall test date	Cylinder test date	Cylinder maturity days	Compressive strength (Mpa)	Strain at peak stress ($x10^3$)
Test 1	RW-A20-P10 S38	07.11.2011 to 07.12.2011	07.06.2011	216	47.1	2.317
Test 2	RW-A20-P10 S64	07.27.2011 to 08.04.2011	08.10.2011	232	48.6	2.014
Test 3	RW-A15-P10 S51	08.19.2011	08.23.2011	255	48.8	2.202
Test 4	RW-A15-P10 S78	10.07.2011	10.10.2011	304	55.8	2.371
Test 5	RW-A15-P2.5-S65	10.24.2011	10.26.2011	321	57.5	2.912

As wall boundary longitudinal reinforcement, eight A706 Grade 60 (yield strength of 414 MPa) vertical bars with various diameters (#4, #5, or #6) were used. The bars were continuous along the wall height and headed at the both ends to prevent congestion and to reduce the required anchorage lengths at the top of the specimens. Vertical and horizontal web reinforcement used in tests #2, #4, and #5 were Grade 60 deformed #3 bars, whereas Grade 60 deformed D6 (6 mm) bars were used in tests #1 and #3. On the other hand, Grade 40 #2 smooth bars (yield strength of 310 MPa) were used for transverse reinforcement (hoops and crossties) in the boundary regions. A minimum of three rebar samples (coupons) from D6, #2, and #3 bars with lengths of 610 mm were subjected to uniaxial tensile test, and the stress-strain relationships in Figure 4.13 were obtained. However, all of the available headed bars (#4, #5, and

#6 bars) were used during the tests, and no headed bars were left for the tensile tests. Therefore, material strengths were adopted as specified in the mill certificates. The cross-sectional areas, yield strengths, and ultimate strengths for the reinforcing bars are provided in Table 4.4 and Figure 4.13.

Table 4.4. Yield and Ultimate Strengths of Reinforcement.

Bar	#2	#3	#4	#5	#6	D6a	d6b
Diameter (mm)	6.4	9.5	12.7	15.9	19.1	6	6
Cross-sectional area, (mm^2)	31.7	71.3	126.7	197.9	285	28.3	28.3
Yield strength (Mpa)	423	443	472	474	477	450	516
Ultimate strength, (Mpa)	492	707	613	620	637	661	580

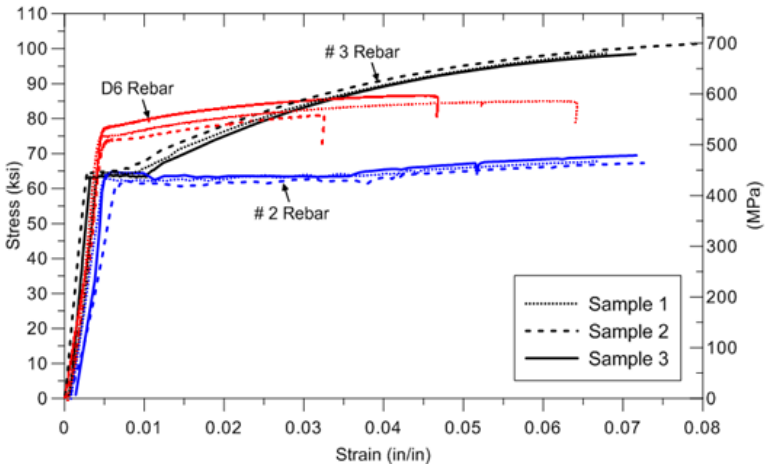

Figure 4.13. Experimental Stress-Strain Relationships for Reinforcement.

4.5. Calibration of the Model for the Wall Specimens

In order to represent the geometric properties, reinforcement attributes, and material characteristics of the wall specimens, the finite element models used for the analyses of the test specimens were calibrated. The constitutive material parameters used in the model formulation were calibrated with respect to the as-tested properties of the materials employed in the construction of the specimens. The constitutive material parameters were also calibrated in terms of the expected compressive and the tensile stress-strain curves of concrete. In addition, the constitutive parameters for reinforcing steel were calibrated to incorporate tension stiffening effects. All calibration was performed according to either as-tested material properties or based on well-established empirical relationships presented in the literature. It should be emphasized that the material parameters were not adjusted to fit the model predictions with the experimental results obtained for the wall specimens. Further information on the calibration of the model is provided in this section.

4.5.1. Calibration of Model Element Dimensions and Reinforcement Ratios

The number of constitutive panel elements (number of meshes) was adjusted such that the meshes are almost square-shaped, and the meshing of the specimen is adequately fine to represent the wall geometry. Corresponding dimensions and numbers of the constitutive model elements (mesh dimension and mesh number) are shown in Table 4.5. The horizontal dimensions of the constitutive model elements (meshes) located in the wall boundaries are different from that of the web regions, while the vertical mesh dimensions are the same throughout the entire wall height. The reinforcement ratios in the boundary and web regions of the walls were calibrated according to the values presented in Table 4.1.

Table 4.5. Wall Model Geometry Details.

Specimen	Model Element Dimension			Model Element Number		
	Horizontal		Vertical	Horizontal		Vertical
	Boundary Region	Web Region		Boundary Region	Web Region	
RW-A20-P10-S38	10.5	10.0	10.2	4	8	24
RW-A20-P10-S63	10.5	10.0	10.2	4	8	24
RW-A15-P10-S51	10.5	10.0	10.2	4	8	18
RW-A15-P10-S78	10.5	10.0	10.2	4	8	18
RW-A15-P2.5-S64	10.5	10.0	10.2	4	8	18

4.5.2. Calibration of Constitutive Material Parameters

Constitutive material parameters involved in the model formulation were calibrated in detail to reflect the as-is properties of the materials that were used in construction of the test specimens. As aforementioned, the constitutive material parameters were also calibrated to obtain reasonable compressive and the tensile stress-strain curves for concrete, and the constitutive parameters for reinforcing steel were calibrated to also incorporate tension stiffening effects.

4.5.2.1. Calibration of the Constitutive Model for Reinforcing Steel. According to Belarbi and Hsu (1994), the average stress-strain relationships of the reinforcing steel bars covered by concrete differs from that of the bare bars, especially when the yield stress is of concern. It was observed that the yield stress of steel a bar reduces when it is embedded concrete, due to the so-called tension stiffening effect. A comparative illustration between the stress-strain behavior of a bare bar and a bar embedded in concrete is provided in Figure 4.14.

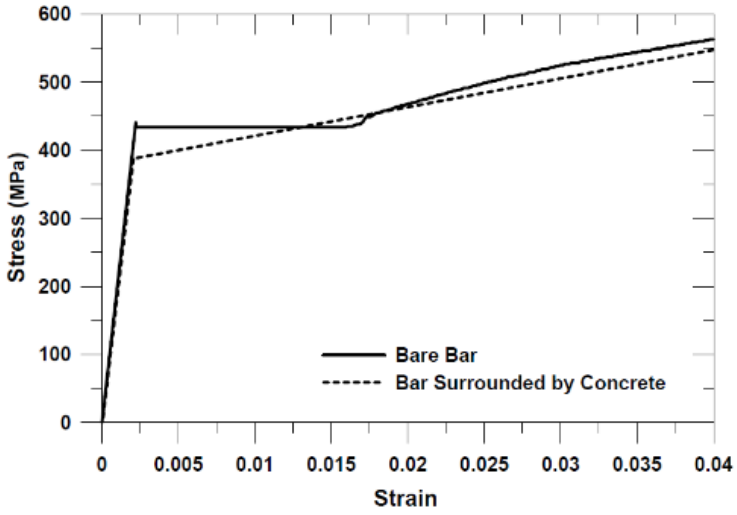

Figure 4.14. The Stress-Strain Behavior of Bare Rebar and Rebar Embedded in Concrete.

Based on the experimental results on uniaxially-loaded column specimens, Belarbi and Hsu (1994) derived empirical relationships between the behavior of bare reinforcing bars and bars surrounded by concrete. The parameters affecting the average yield stress of an embedded bar were found to be the ratio of the cross-sectional area of the longitudinal steel bars to that of concrete, namely ρ, and the ratio of concrete tensile (cracking) strength (f_{cr}) to the yield strength of the bare bar (σ_y). The strain hardening ratio of a bar embedded in concrete also differs from the strain hardening ratio of the bare bar.

According to Belarbi and Hsu (1994), the monotonic stress-strain envelope of a reinforcing bar surrounded by concrete can be described by two regions. The first being the elastic range with a slope of modulus of elasticity of the steel bar (E_s), and the second being the post-yield range with a slope of E_p* (Figure 4.15).

The monotonic stress-strain envelope of a reinforcing bar surrounded by concrete can be described by two regions. The first being the elastic range with a slope of modulus of elasticity of the steel bar (E_s), and the second being the post-yield range with a slope of E_p* (Figure 4.15).

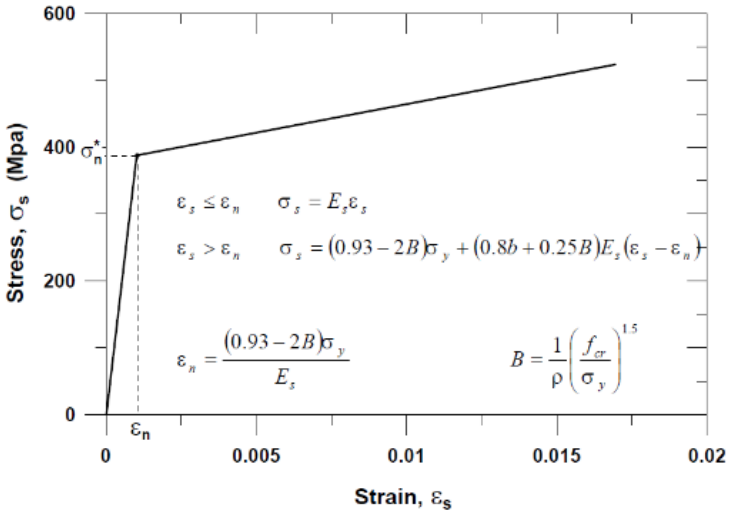

Figure 4.15. Stress-Strain Relationship by Belarbi and Hsu (1994) for the Bar in Concrete.

The effective yield stress (σ_n*), which is defined as the point where the two regions intersect, and the plastic slope (E_p*) is given in Equation 4.6-Equation 4.7.

$$\sigma_n^* \epsilon_n = (0.93 - 2B)\sigma_y \tag{4.6}$$

The B parameter in the above equations is defined as:

$$E_p^* = (0.8b + 0.25B)E_s \tag{4.7}$$

$$B = \frac{1}{\rho}\left(\frac{f_{cr}}{\sigma_y}\right)^{1.5} \tag{4.8}$$

and b is the strain hardening ratio (E_p/E_s) defined for the bare bar.

Accordingly, the model of Belarbi and Hsu (1994) for modeling the average stress-strain behavior of bars embedded in concrete (Figure 4.15) is defined as:

$$\text{If } \varepsilon_s \leq \varepsilon_n, \sigma_s = E_s\varepsilon_s \tag{4.9}$$

$$\text{If } \varepsilon_s > \varepsilon_n, \sigma_s = (0.93 - -2B) + (0.8\text{b} + 0.25B)\, E_s(\varepsilon_s - \varepsilon_n) \tag{4.10}$$

where σ_s is the average stress, ε_s the average strain and ε_n the average strain defined at the intersection of the two lines as defined in the equation below:

$$\varepsilon_n = \frac{\sigma_n^*}{E_s} = \frac{(0.93 - 2B)\,\sigma_y}{E_s} \tag{4.11}$$

Here, E_s, σ_y and b are the modulus of elasticity, yield stress, and experimentally-measured strain hardening ratio of bare bars, respectively. The calibrated parameters belonging to the reinforcing steel bars of the specimens are presented in the following section.

Calibrated Constitutive Parameters for Reinforcing Steel Bars: Table 4.6 shows the calibrated parameters of the reinforcing steel bars used in the test specimens. Through the Table 4.6, reinforcement ratios (ρ), strain hardening slopes (E_p*), and the stress (σ_n) and strain (ε_n) values at the intersection of the elastic and post-yield regions are provided. The calibrated parameters of the first set of specimens are listed in Table 4.6. Two different bar diameters, ϕ8 and ϕ16, exist in these specimens. As expected, the tension stiffening phenomenon affects the constitutive parameters of the bars in tension only, and it has no influence on the parameters of the bars in compression. The parameters for bars in compression are identical to those obtained for bare bar tests.

4.5.2.2. Calibration of the Constitutive Model for Concrete. In order to obtain reasonable stress-strain relationships for concrete in compression and tension, the constitutive material parameters for concrete were calibrated in detail. The compression envelope curve of the model proposed by Chang and Mander (1994) is defined by the initial slope E_c (elastic modulus of concrete), the peak coordinate (ε_c', f_c'), a parameter r from Tsai's (1988) equation defining the shape of the envelope curve, and the parameter $x_{cr}' > 1$ to define the normalized strain at which the stress-strain curve transforms into a straight line, namely a transition point (Figure 4.16).

Table 4.6. Calibrated Values of the Constitutive Parameters of Reinforcing Steel Bars for the Wall Specimens.

Specimen	Mesh Location	ϕ	$\rho(\%)$	Compression		Tension	
				f_y	b	o_n*	b'
RW-A20-P10-S38	Boundary Mesh						
	Horizontal	#2	0.834	423	0.00300	393	0.00251
	Vertical	#4	3.23	472	0.01042	439	0.00836
	Web Mesh						
	Horizontal	D6b	0.27	450	0.02000	417	0.01631
	Vertical	D6a	0.27	516	0.00328	479	0.00288
RW-A20-P10-S63	Boundary Mesh						
	Horizontal	#2	0.834	423	0.00300	393	0.00252
	Vertical	#6	7.11	477	0.01031	444	0.00826
	Inner Mesh						
	Horizontal	#3	0.61	443	0.01697	411	0.01372
	Vertical	#3	0.61	443	0.01697	411	0.01372
RW-A15-P10-S51	Boundary Mesh						
	Horizontal	#2	0.834	423	0.00300	393	0.001372
	Vertical	#4	3.23	472	0.01042	439	0.01372
	Inner Mesh						
	Horizontal	D6b	0.32	450	0.02000	417	0.01628
	Vertical	D6a	0.32	516	0.00328	479	0.00286
RW-A15-P10-S78	Boundary Mesh						
	Horizontal	#2	0.834	423	0.00300	393	0.00255
	Vertical	#6#5	6.06	476	0.01018	442	0.01018
	Inner Mesh						
	Horizontal	#3	0.73	443	0.01697	411	0.01373
	Vertical	#3	0.73	443	0.01697	411	0.01373
RW-A15-P2.5-S64	Boundary Mesh						
	Horizontal	#2	0.834	423	0.00300	393	0.00255
	Vertical	#6#5	0.06	476	0.01018	442	0.01018
	Inner Mesh						
	Horizontal	#3	0.61	443	0.01697	411	0.01377
	Vertical	#3	0.61	443	0.01697	411	0.01377

The calibration of the constitutive parameters for concrete in tension and con-

crete in compression were conducted based on different criteria. Calibration of the stress-strain relationship for concrete in tension was based on the empirical relationships suggested by Belarbi and Hsu (1994), to take into account the tension stiffening effects on cracked concrete.. On the other hand, for concrete in compression, the constitutive parameters (excluding the as-tested concrete compressive strength) were mainly calibrated using the empirical relationships proposed by Chang and Mander (1994); however, for the purpose of comparison, the Saatcioglu-Razvi Model (1992) was also utilized for the calibration of the critical strain parameter being the transition point between the envelope curve and the straight line.

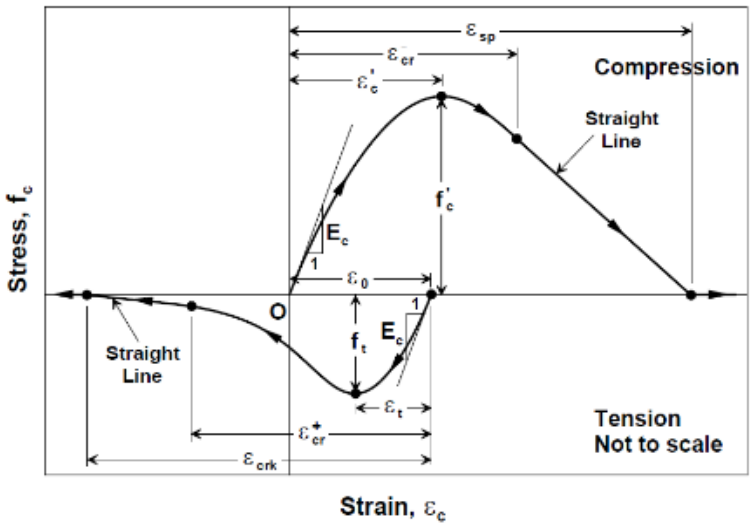

Figure 4.16. Compression and Tension Envelope Curves of the Model by Chang and Mander (1994).

Concrete in Compression: The compressive strength of concrete (f'_c), the strain at compressive strength (ε'_c), the initial Young's Modulus (E_c), the parameter r defining the shape of the envelope, and the normalized critical strain x^-_{cr} (also named x_{crn}) where the curve becomes a straight line are the parameters regarding to the compression envelope curve of the model. Chang and Mander (1994) suggested empirical relationships for the parameters E_c, ε'_c and r as in the Equation 4.12-4.14.

$$Initial\ modulus\ of\ elasticity : E_c = 8200(f'_c)^{(3/8)} \tag{4.12}$$

$$Strain\ at\ compressive\ strength : \varepsilon_c' = \frac{(f_c')^{0.25}}{1150} \tag{4.13}$$

$$Shape\ parameter : r = \frac{f_c'}{5.2} - 1.9 \tag{4.14}$$

The unit of f_c' in the empirical relationships in the above equations is MPa.

The normalized critical strain value x_{crn} was calibrated through a graphical manner, since no empirical relationships exists for x_{crn}. The stress-strain envelopes for unconfined concrete proposed by Chang and Mander (1994) and Saatcioglu and Razvi (1992) were compared via visual observation. It was intended to produce parallel straight lines in the descending portion of the stress-strain curves (Figure 4.17). The calibration was achieved by a basic trial and error approach for each individual specimen. The post-peak behavior of the stress-strain relationship for both confined and unconfined concrete was calibrated by the use of parameter ε_{cr}, which defines the strain where the descending (linear) branch of the monotonic stress-strain relation reaches zero stress, such that the post-peak slope of the concrete stress-strain model agrees with the post-peak slope of the Saatcioglu and Razvi (1992) model for both confined and unconfined concrete. The calibrated constitutive parameters for concrete in compression are listed in Table 4.7 for all five of the test specimens.

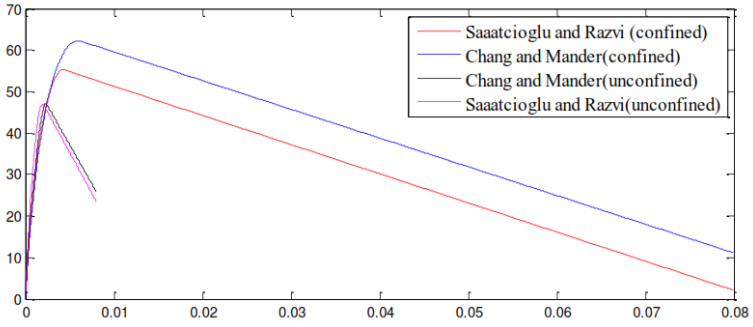

Figure 4.17. Stress-Strain Curves for Confined and Unconfined Concrete in Compression for Specimen RW-A20-P10-S38.

Table 4.7. Calibrated Values of the Constitutive Parameters for Concrete in Compression.

Concrete in Compresion Web					
Specimen	f'$_c$ (Mpa)	E$_c$(Mpa)	ε'_c	r	x$_{crn}$
RW-A20-P10-S38	47.1	34965	0.002317	7.208	1.045
RW-A20-P10-S63	48.6	35378	0.002014	7.498	1.032
RW-A15-P10-S51	48.8	35433	0.002202	7.537	1.032
RW-A15-P10-S78	55.8	37259	0.002371	8.891	1.026
RW-A15-P2.5-S64	57.5	37681	0.002912	9.220	1.025
Concrete in Compresion Web					
Specimen	E$_{cc}$ (Mpa)	ε_{cc}	r	X$_{crn}$	f$_{cc}$
RW-A20-P10-S38	38596	0.006000	3.400	1.071	62.221
RW-A20-P10-S63	39379	0.005500	2.150	1.118	65.647
RW-A15-P10-S51	3899	0.005600	2.300	1.107	63.971
RW-A15-P10-S78	40884	0.005900	2.200	1.113	72.552
RW-A15-P2.5-S64	41250	0.007200	4.400	1.062	74.296

Concrete in Tension: The calibration of the concrete stress-strain relationship in tension was performed considering the following constitutive parameters: The initial slope (elastic modulus) of the average stress-strain relationship (E_c), the tensile (cracking) strength of concrete (f_{cr}) the strain at cracking (ε_{cr}), the parameter r representing the shape of the curve, and the normalized critical strain at which the stress-strain curve becomes a straight line (x_{crp}). Concrete test results for these parameters were missing, since concrete tension tests were not conducted during the wall test program. Hence, calibration of the constitutive parameters for concrete in tension were performed in compliance with the empirical relationships suggested by Belarbi and Hsu (1994), which also considers the effect of tension stiffening on cracked concrete.

The average stress-strain relationship proposed by Belarbi and Hsu (1994) for

concrete in tension (Figure 4.18) is defined by Equations 4.15-Equation 4.16.

$$\text{If } \varepsilon_c > \varepsilon_{cr} \text{ then } \sigma_c = E_c \varepsilon_c \tag{4.15}$$

$$\text{If } \varepsilon_c > \varepsilon_{cr} \text{ then } \sigma_c = f_{cr}\left(\frac{\varepsilon_{cr}}{\varepsilon_c}\right)^{0.4} \tag{4.16}$$

where

$$E_c = 3875\sqrt{f'_c(MPa)} \tag{4.17}$$

$$f_{cr} = 0.31\sqrt{f'_c(MPa)} \tag{4.18}$$

$$\varepsilon_{cr} = 0.00008 \tag{4.19}$$

As can be observed in Figure 4.18, the stress-strain relationship of Belarbi and Hsu (1994) can be described by two regions, the first being the linear region, and the second being the exponentially-descending region.

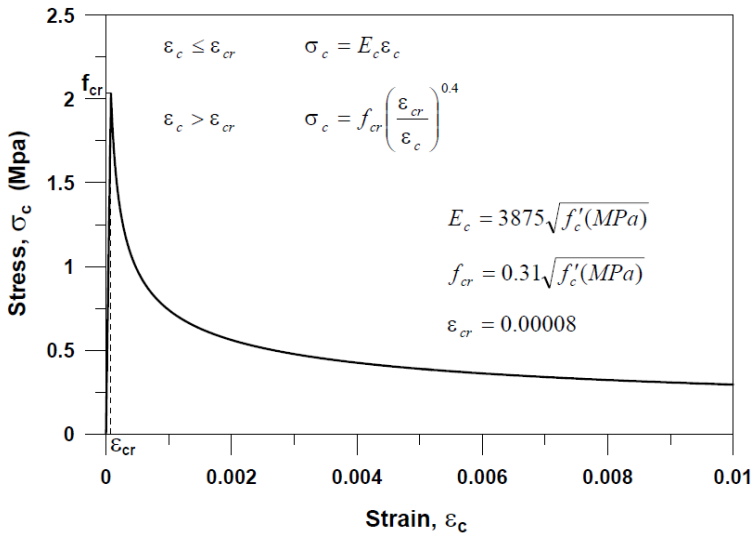

Figure 4.18. Stress-Strain Relationship by Belarbi and Hsu (1994) for Concrete in Tension.

Table 4.8. Calibrated Values of the Constitutive Parameters for Concrete in Tension.

Specimen	E_c (Mpa)	f_{cr} (Mpa)	ε_{cr}	rt	X_{crp}
RW-A20-P10-S38	34965	2.128	0.00008	1.23000	10000
RW-A20-P10-S63	35378	2.161	0.00008	1.23000	10000
RW-A15-P10-S51	35433	2.166	0.00008	1.23000	10000
RW-A15-P10-S78	37259	2.316	0.00008	1.23000	10000
RW-A15-P2.5-S64	37681	2.351	0.00008	1.23000	10000

The normalized critical strain value for concrete in tension (where the descending region of the stress-strain relationship transforms from a curve into a straight line) was calibrated so that the descending region continues as a curve and does not transform into a straight line, which is the case for the descending portion of the Belarbi and Hsu (1994) relationship. Such calibration was achieved by assigning a very large hypothetical value to the x_{crp} parameter (e.g., 10000), and thereby shifting the transition point to very large strain value far away from the range of interest. The parameter r_t (controlling the shape of the tension envelope) was calibrated graphically by visual observation. For calibration of , the shape of the stress-strain curve obtained using the Chang and Mander (1994) model was intended to visually match the Belarbi and Hsu (1994) relationship, as shown in Figure 4.19. The calibrated constitutive parameters for concrete in tension are listed in Table 4.8 for all five of the test specimens.

The normalized critical strain value for concrete in tension, was calibrated so that no linear range is observed and the curve always stays as a curve, which is the case for the descending portion of the Belarbi and Hsu (1994) relationship. Such calibration was achieved by assigning an enormous value to the x_{crp} parameter (also can be deemed the transition point), i.e. shifting this point far away from the range of interest. Just like the previous case mentioned above, the parameter r_t (controlling the shape of the tension envelope) was calibrated graphically by visual observation. The shape of the stress-strain diagram obtained by the Chang and Mander (1994) model with the Belarbi and Hsu (1994) relationship were intended to match for the calibration, which are given in Figure 4.19. The calibrated parameters of concrete in tension are listed in

Table 4.8 for all the test specimens.

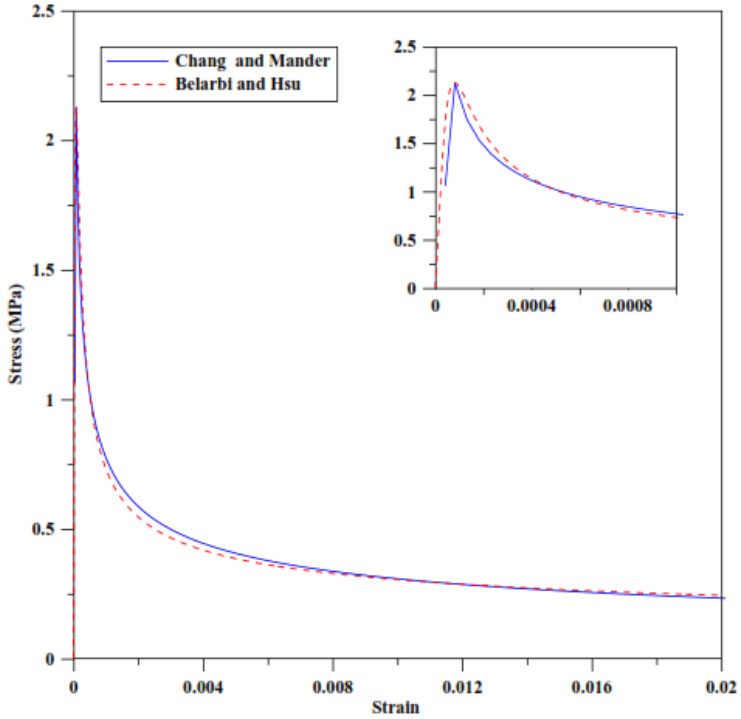

Figure 4.19. Stress-Strain Diagrams for Concrete in Tension for RW-A20-P10-S38.

5. COMPARISON OF ANALYTICAL AND EXPERIMENTAL RESULTS

This chapter presents detailed information on experimental validation of the model, via comprehensive correlation studies between model predictions and experimental results obtained for the five moderate-aspect-ratio RC wall specimens investigated, at both global and local response levels. Descriptions of the wall specimens, test setup, and instrumentation layout in the test program launched by Tran and Wallace (2012) were presented in Chapter 4, where the calibration of the model to represent the wall specimens was also described. The response quantities obtained from the analyses using the calibrated analytical model are compared with the processed test data, in an effort to validate the model and to propose possible improvements to the model. The response quantities evaluated in this chapter consist of lateral load vs. top displacement, contributions of flexural and shear deformation components to the response (lateral load vs. flexural deformation, lateral load vs. shear deformation, relative contributions of shear and flexural deformations), lateral displacement profile as well as flexural and shear deformation profiles over wall height, wall vertical growth, crack patterns, and local deformations (vertical strain distributions and rotations at the base of the wall).

5.1. Lateral Load versus Top Displacement Response

For the five wall specimens, analytically-predicted and experimentally-measured lateral load vs. top lateral displacement responses are compared in this section. Comparisons of important response characteristics which determine the quality of agreement between the analytical model and experimental results, such as the lateral load capacity, stiffness degradation, hysteretic shape, ductility, and pinching characteristics of the walls are discussed.

5.1.1. Lateral Stiffness and Load Capacity

In Figures 5.1-5.5, wall lateral load vs. lateral top displacement responses and the contributions of shear deformations to lateral displacement are compared. The contribution of shear deformations to lateral displacements are evaluated in detail in Section 5.4.4. For specimens RW-A20-P10-S38 and RW-A15-P10-S51, lateral strength degradation (failure) initiated with crushing of core concrete in wall boundaries and buckling of longitudinal boundary reinforcement. Strength degradation due to widening of the diagonal cracks was also observed during the tests. As shown in Figure 5.1 and Figure 5.3, the analytical model results are in agreement with the test results for these two specimens, in terms of lateral load capacity and ductility, as well as other important response characteristics such as stiffness degradation, plastic deformations and pinching. The analytical model slightly underestimates the lateral load capacity of specimens RW-A20-P10-S38 and RW-A20-P10-S63 at positive loading cycles. The model also provides a reasonable response prediction for specimen RW-A20-P10-S63, which experienced strength degradation due to the crushing of concrete starting from the base of the wall and propagating along diagonal compression struts. As shown in Figure 5.2, the model provides very close estimations for this specimen in terms of stiffness degradation and pinching. For specimens RW-A15-P10-S78 and RW-A15-P2.5-S64, which experienced failure due to crushing of the diagonal compression strut at wall base, model predictions presented in Figures 5.4 and 5.5 are again reasonable. However, distinctively for specimen RW-A15-P2.5-S64, the model fails to capture the pinching behavior in the measured lateral load-displacement response accurately. This specimen was subjected to a very low axial load level, and experienced unexpected formation of a premature horizontal crack close to the bottom of the wall (along a horizontal reinforcing bar in the wall web), resulting in sliding shear behavior along that horizontal crack, which could not be predicted by the model. It can be deduced from the figures that, the lateral stiffness values, i.e. the slope of the force-displacement curve, are almost perfectly matched for the five specimens. However, during the last loading cycles of the specimens exhibiting degradation (only the last cycles RW-A15-P10-S51, RW-A15-P10-S78, and RW-A15-P2.5-S64), the model tends to estimate larger lateral stiffness, as expected. This degradation is not well captured by the analytical model.

Overall, with the exception of specimen RW-A15-P2.5-S64, which suffered premature sliding shear failure, the model provides reasonably accurate predictions for lateral load-displacement responses of the wall specimens.

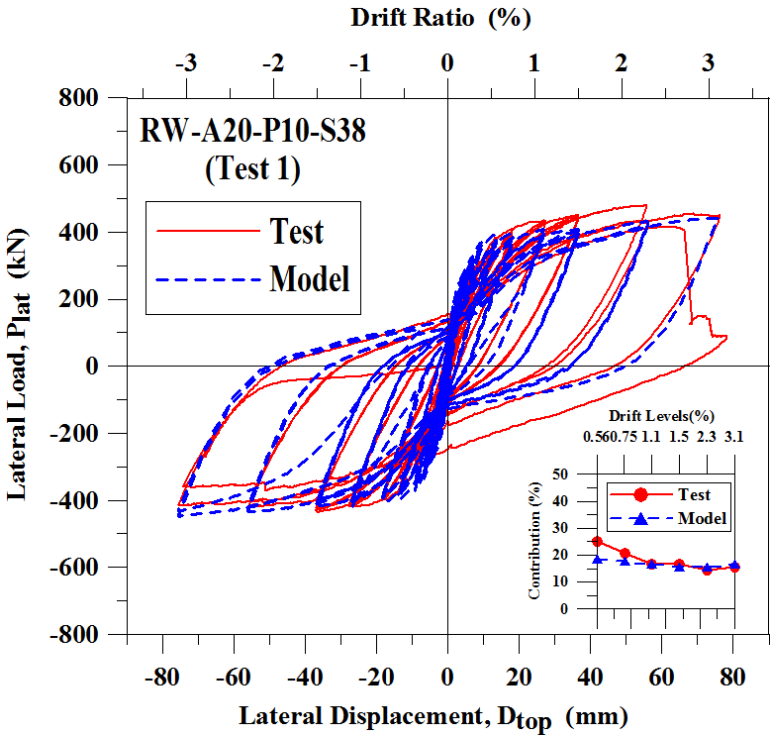

Figure 5.1. Lateral Load-Displacement Response of Specimen RW-A20-P10-S38.

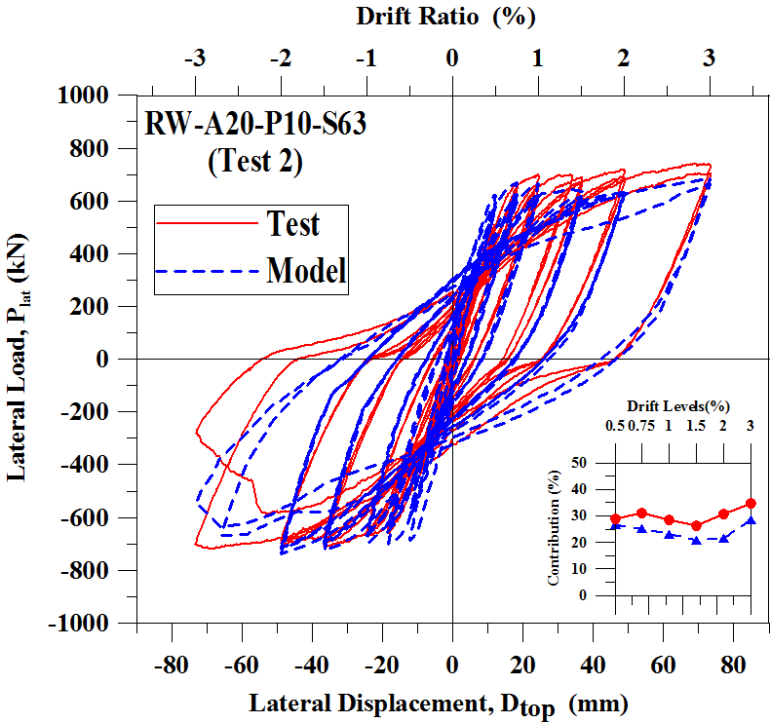

Figure 5.2. Lateral Load-Displacement Response of Specimen RW-A20-P10-S63.

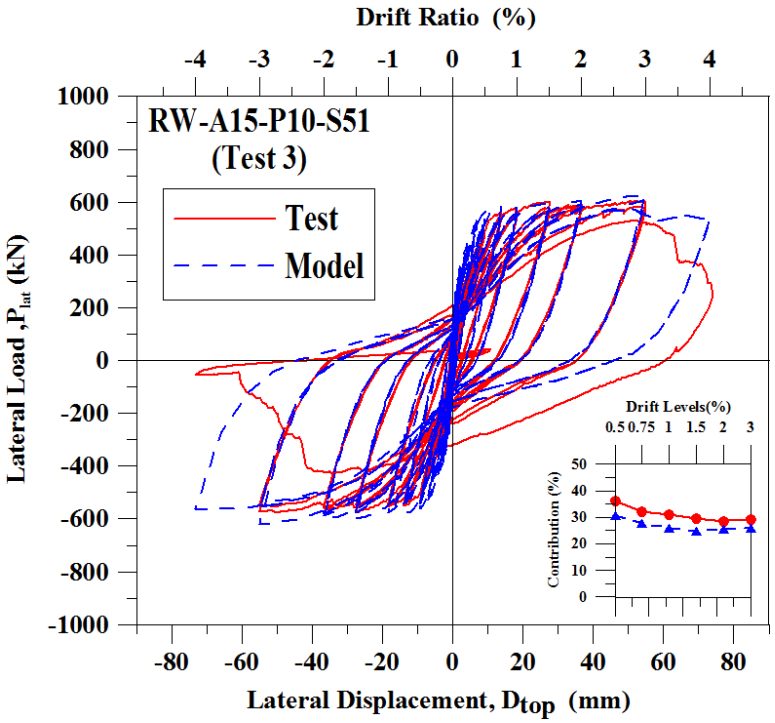

Figure 5.3. Lateral Load-Displacement Response of Specimen RW-A15-P10-S51.

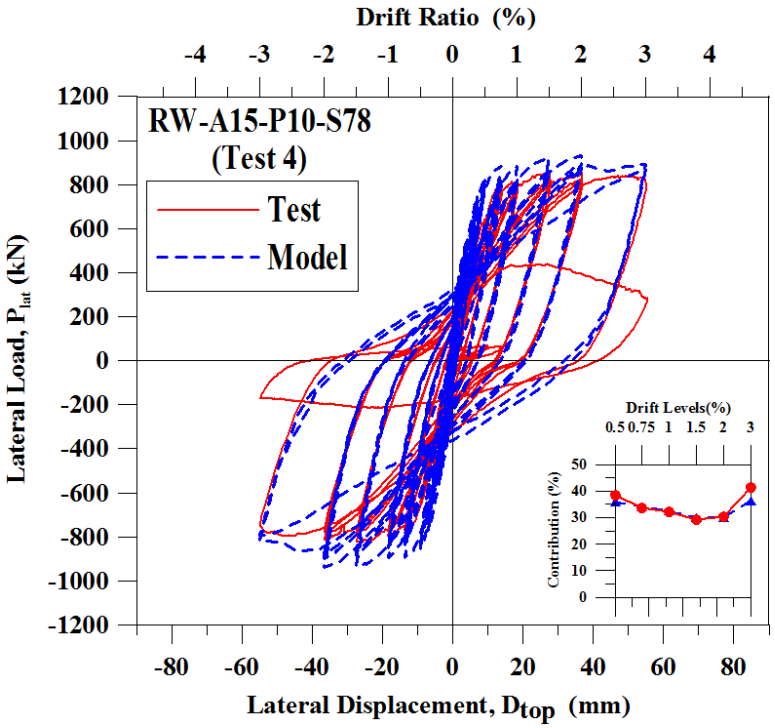

Figure 5.4. Lateral Load-Displacement Response of Specimen RW-A15-P10-S78.

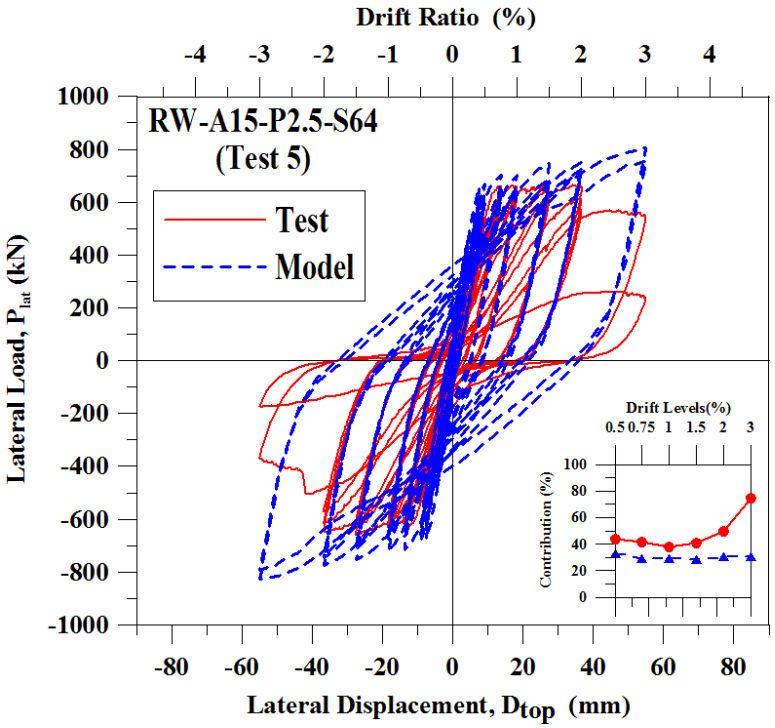

Figure 5.5. Lateral Load-Displacement Response of Specimen RW-A15-P2.5-S64.

5.2. Failure Mechanisms

According test results of Specimen RW-A20-P10-S38, during the second loading cycle to 3.0% lateral drift crushing of core concrete in the boundary element and buckling of boundary longitudinal reinforcement caused sudden diagonal tensional failure with fracture of horizontal web bars along a diagonal crack, resulting in decrease in wall lateral strength to roughly 30% of its peak value (Figure 5.1). At the drift level of 3.0%, the analytical model predicts the initiation of concrete crushing in wall boundaries accurately. However, the significant strength degradation caused by the buckling of longitudinal reinforcement was not captured because the constitutive stress-strain relationship adopted in the model for reinforcing steel does not incorporate buckling. For Specimen RW-A20-P10-S63, during the second loading cycle in negative direction at 3.0% drift, lateral instability of the boundary zone (out of plane buckling of the boundary) was observed due to concrete crushing and bar buckling in the wall boundary, which led to a drop of wall strength to 39% of its peak value (Figure 5.2). Similarly, strength degradation initiated by buckling of longitudinal reinforcement was

not captured by the analytical model. For Specimen RW-A15-P10-S51, crushing of core concrete of the south wall boundary and buckling of vertical boundary reinforcement were observed at 4% drift in positive loading direction, resulting in initiation of diagonal tension failure along a major crack with fracture of several horizontal web bars crossing the diagonal crack. Strength loss to 59% of the peak capacity was observed at this drift level, as can be seen in Figure 5.3. When reversed loading was applied, fracture of two longitudinal bars at the south wall boundary was observed, along with concrete crushing and buckling of longitudinal reinforcement at the north wall boundary causing the lateral load to drop to only 10% of the peak capacity (Figure 5.3). In the analysis, crushing of concrete in wall boundaries was predicted in both positive and negative loading directions at 4.0% drift, which resulted in a drop of the predicted lateral load capacity to approximately 80% in positive loading direction and 90% of peak lateral load in negative loading direction, as shown in Figure 5.3. Degradation due to the buckling and fracture of reinforcing bars were not captured. During testing of Specimen RW-A15-P10-S78, boundary region cover concrete spalled during 3.0% lateral drift along the wall base, resulting in 10% loss in lateral load capacity. During the second cycle to 3.0% drift, occurrence of shear sliding near the base of the wall followed by out-of-plane buckling led to 67% loss of the lateral load capacity (Figure 5.4). When the load was reversed, out-of-plane buckling occurred on the other (opposite) wall boundary, and the lateral load dropped to 20% of the peak value (Figure 5.4). In the model, shear sliding failure at the wall base is not considered, which caused the difference between the model and test results. On the other hand, spalling of cover concrete and strength degradation of the confined concrete were captured in the analytical predictions. For Specimen RW-A15-P2.5-S64, during the first loading cycle to 3.0% drift, spalling of cover concrete was observed along diagonal compressive struts near the wall-foundation interface at the wall boundaries, leading to relatively significant strength degradation in both loading directions. The wall lateral strength decreased significantly due to shear sliding followed by in-plane buckling of boundary longitudinal reinforcement during the subsequent cycle. The wall capacity dropped to 55% of the peak value at negative 3.0% drift due to these factors (Figure 5.5). Again, the analytical model does not consider shear sliding at or near the base of the wall, nor buckling of wall reinforcement. Some failure mechanisms observed in the

experiments that occurred after the initiation of wall strength degradation, i.e. rebar buckling and fracture, shear sliding along the base of the wall and lateral instability of the wall boundary, are not implemented in the present model formulation. Therefore, analytical results do not accurately represent the failure mechanisms observed during experiments, and therefore do not capture the significant and sudden strength degradation observed in the experimental load-displacement responses.

5.3. Shear and Flexural Components of Lateral Displacement

In this section, flexural and shear deformation components of wall lateral displacements are compared. The experimental and analytical responses are presented in terms of to load-versus-deformation-component relationships.

5.3.1. Lateral Load versus Flexural Displacement Relations

Experimental and analytical responses for the lateral-load-versus-flexural-displacement at the top of the wall for Tests 1 to 5 are shown in Figure 5.6 to Figure 5.10, respectively. The experimental flexural displacement measurement method was presented in Section 4.3.2. Analytically-predicted flexural displacement is computed as the difference between total lateral displacement and shear displacement. For the specimens with an aspect ratio of 2.0, which are flexure-dominant specimens, the overall shape of the load vs. flexural displacement responses resemble the shape of the load vs. total displacement responses shown in Figure 5.1 and Figure 5.2. The main difference between the two responses is that flexural deformations in RW-A20-P10-S63 (Test 2) were much smaller than those in RW-A20-P10-S38 (Test 1) at large drift ratios, although both of these two specimens reached about the same drift levels prior to significant loss of lateral strength. Comparison between the responses of RW-A20-P10-S38 and RW-A20-P10-S63 also indicates that the wall with higher shear stress demand has less pinching, probably due to a deeper compression zone, which would lead to more pull-out, or slip/extension of vertical reinforcement, in the wall with lower shear. The shape of load vs. flexural displacement responses, as well as flexural loading and unloading stiffness characteristics are well-estimated by the analytical model. It can be seen from

Figure 5.6 to Figure 5.8 that experimentally-measured and analytically-predicted load vs. flexural displacement relations for specimens with aspect ratio of 1.5 are characterized by the absence of pinching, whereas the load vs. total displacement relations for these specimens were characterized by moderately-to-highly pinched shapes, indicating that flexural deformations are less pronounced in the 1.5-aspect-ratio specimens compared to the 2.0-aspect-ratio specimens.

Experimentally-measured flexural displacements of RW-A15-P10-S78 tend to be smaller than those of RW-A15-P10-S51 during cycles at large drift levels, probably for the same reasons noted in the comparisons of RW-A20-P10-S38 and RW-A20-P10-S63. Analytical results capture experimental results at drift levels which are smaller than 3% for RW-A15-P10-S51 and RW-A15-P10-S78. For RW-A20-P10-S38, overall shape of the lateral load versus flexural displacements relations are captured by specimen, but the analytical model underestimates the capacity in positive loading direction. The analytical model provides accurate results for RW-A20-P10-S63 at all drift levels, except 3.0%. For RW-A15-P2.5-S64, with relatively low axial load level, experimental results reveal that flexural deformations are much smaller than those of RW-A15-P10-S78 after yielding of boundary longitudinal reinforcement. The analytical model overestimates flexural deformations at all drift levels for RW-A15-P2.5-S64. The model predicts reasonably well the flexural loading/unloading stiffness of the wall specimens in Tests 1 to 4 throughout the entire cyclic loading history. For Test 5, the flexural stiffness is obviously not captured.

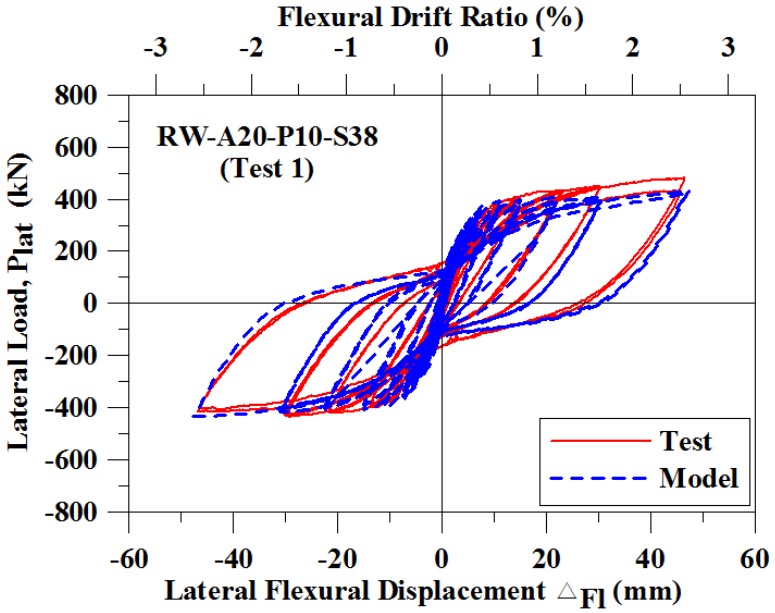

Figure 5.6. Load vs. Flexural Displacement for Specimen RW-A20-P10-S38.

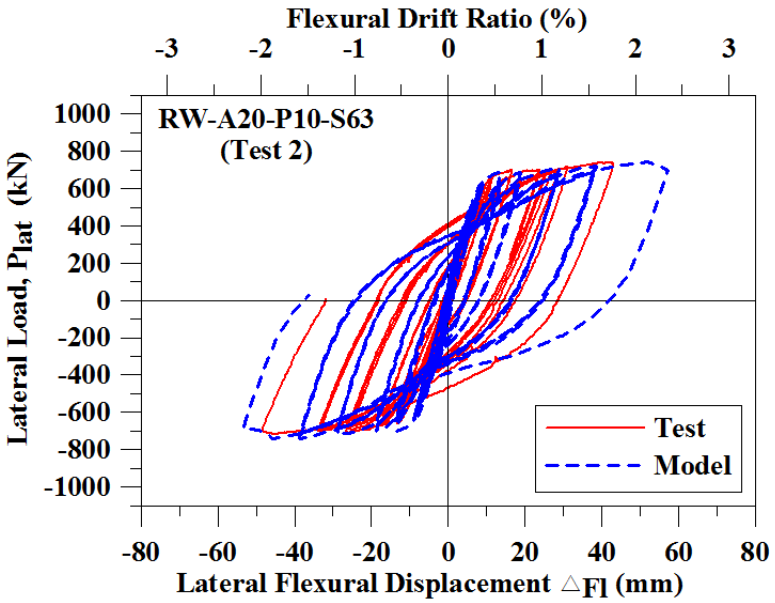

Figure 5.7. Load vs. Flexural Displacement for Specimen RW-A20-P10-S63.

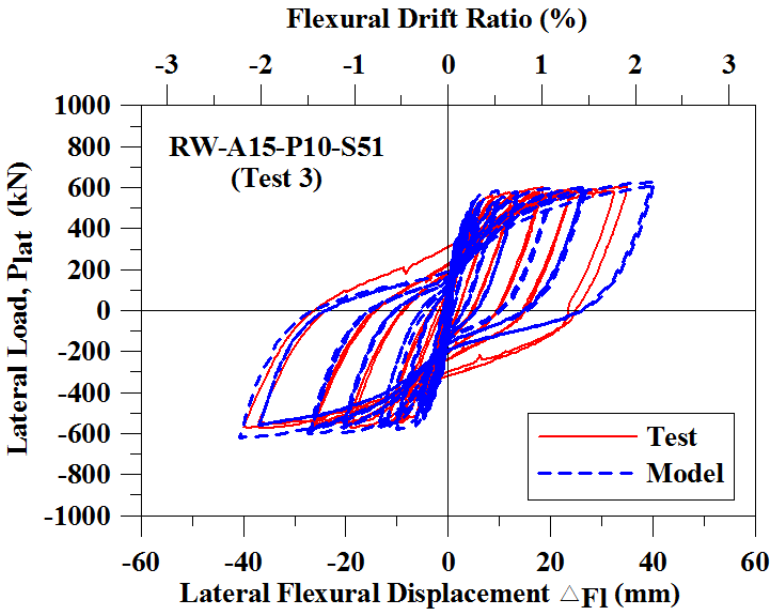

Figure 5.8. Load vs. Flexural Displacement for Specimen RW-A15-P10-S51.

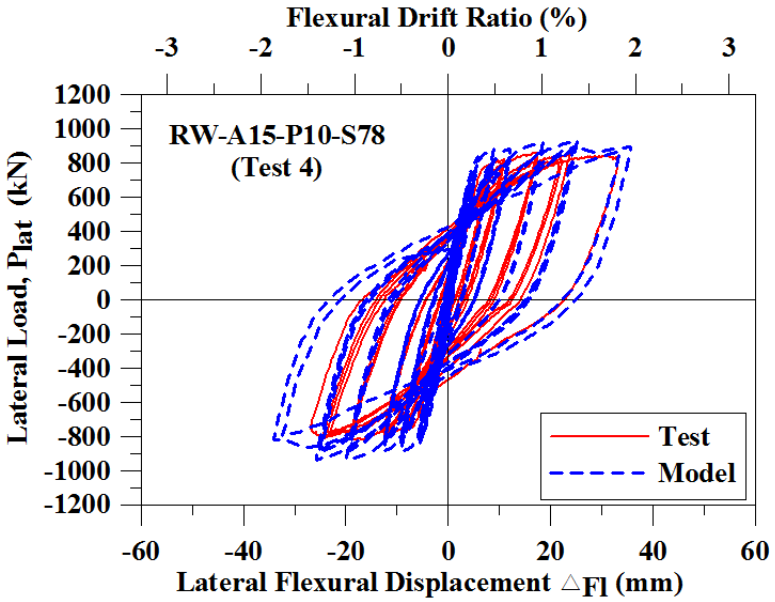

Figure 5.9. Load vs. Flexural Displacement for Specimen RW-A15-P10-S78.

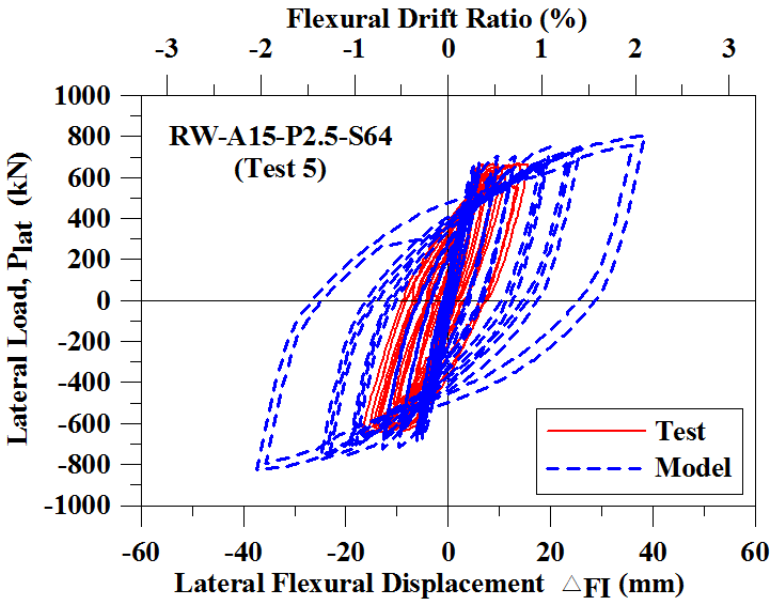

Figure 5.10. Load vs. Flexural Displacement for Specimen RW-A15-P2.5-S64.

5.3.2. Lateral Load versus Shear Displacement Relations

The experimental shear displacement measurement method was described in Section 4.3.3. Analytically-predicted shear displacements were calculated by using average shear strain values of all the individual model elements that are lined up at the same vertical level multiplied by the element height, and these average shear displacement values are summed over the wall height for obtaining the cumulative shear displacement. Experimental and analytical lateral load vs. top shear displacement relations for Tests 1 to 5 are presented in Figure 5.11 to Figure 5.15. The results indicate that the shapes of shear load-deformation responses are highly pinched for all wall specimens, and that the magnitudes of shear deformations are larger for specimens with lower aspect ratio. Comparisons of results for specimens with aspect ratio of 1.5 indicate that shear displacements in Test 5 were far greater than those in Tests 3 and 4, suggesting that axial stress had a significant impact on the magnitude of the shear displacement, i.e., sliding shear displacements may increase significantly as axial stress decreases.

It can be observed from Figure 5.11 to Figure 5.15 that the analytical model captures the highly-pinched shape of the load vs. shear displacement relationships

for all specimens, and that the magnitudes of shear deformations are reasonably well-predicted by the model. For specimens with aspect ratio of 2.0 (Tests 1 and 2), the model underestimates the shear displacements during the last loading cycle in positive direction. For specimens with an aspect ratio of 1.5 (RW-A15-P10-S51, RW-A15-P10-S78 and RW-A15-P2.5-S64), the model captures the overall hysteretic shape for specimens RW-A15-P10-S51 and RW-A15-P10-S78. However, as seen in Figure 5.15, the analytical model cannot predict the measured shear deformations of specimen RW-A15-P2.5-S64, which suffered unexpectedly large shear deformation due to a premature sliding shear failure. In addition, for all five wall specimens, shear stiffness is not accurately predicted by the model at lower drift levels.

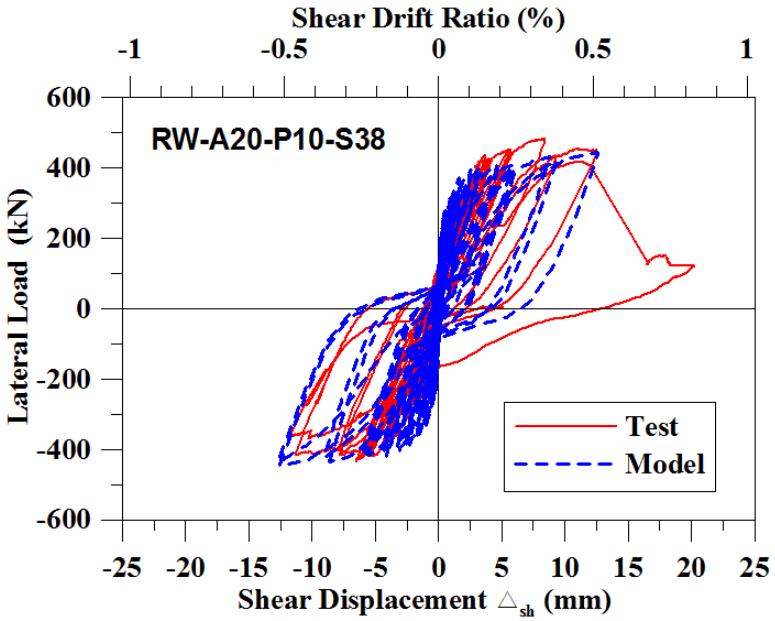

Figure 5.11. Load vs. Shear Displacement, Specimen RW-A20-P10-S38, Test 1.

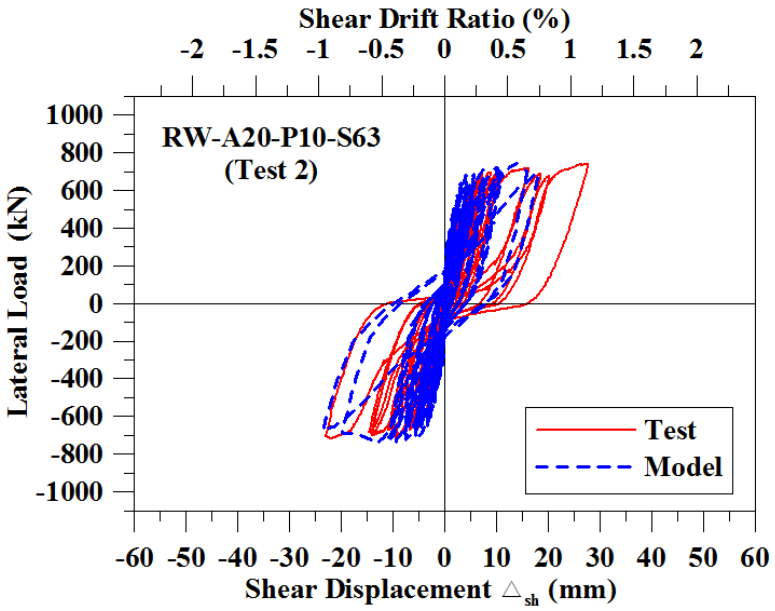

Figure 5.12. Load vs. Shear Displacement, Specimen RW-A20-P10-S63, Test 2.

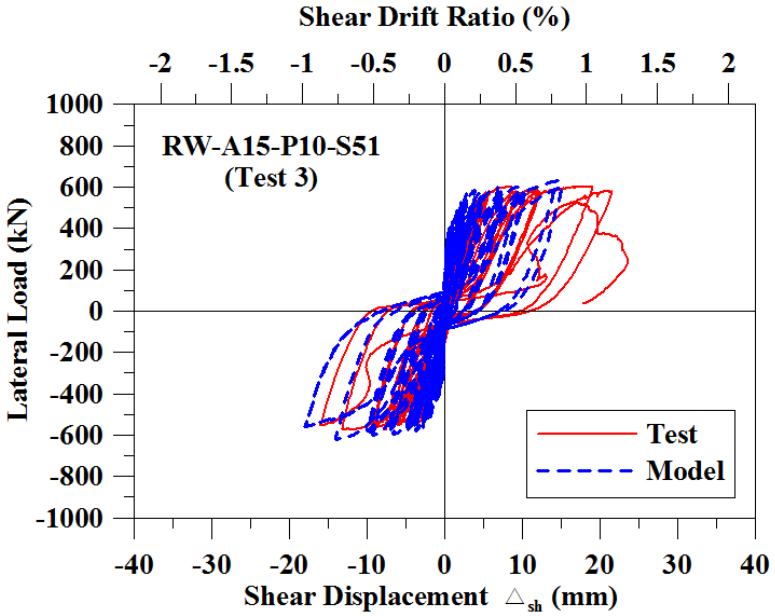

Figure 5.13. Load vs. Shear Displacement, Specimen RW-A15-P10-S51, Test 3.

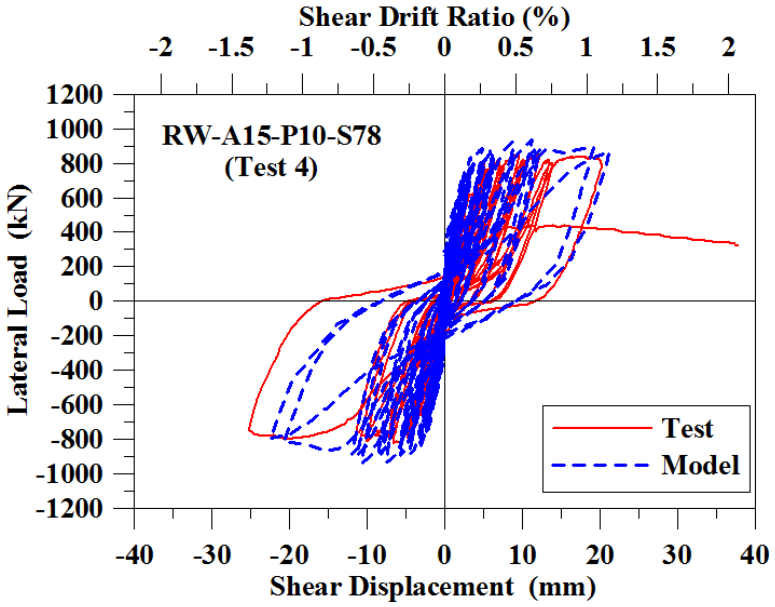

Figure 5.14. Load vs. Shear Displacement, Specimen RW-A15-P10-S78, Test 4.

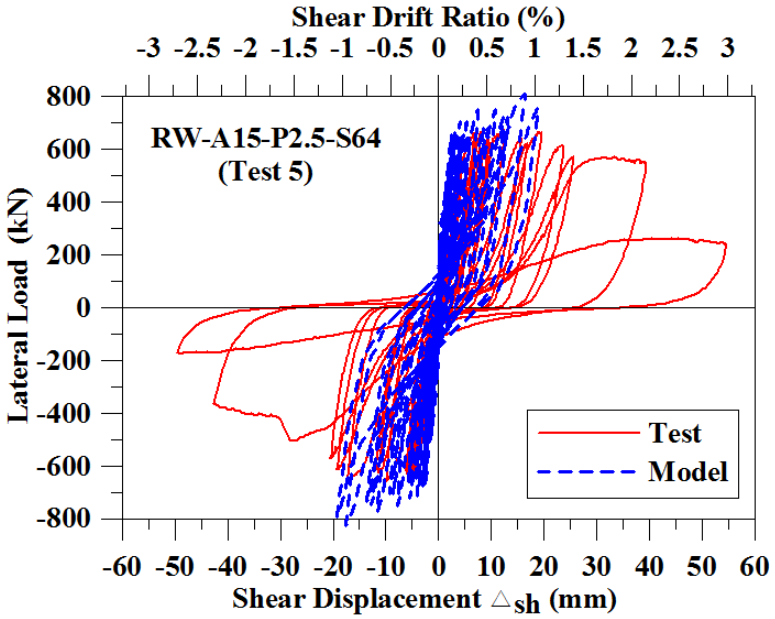

Figure 5.15. Load vs. Shear Displacement, Specimen RW-A15-P2.5-S64, Test 5.

5.4. Wall Vertical Growth

5.4.1. Vertical Growth versus Top Lateral Displacement Relations

Wall vertical growth (upward vertical displacement at wall centroid) vs. lateral displacement at the top of the wall specimens for Tests 1 to 5 are compared in Figure 5.16 to Figure 5.20, respectively. The experimentally-measured relations indicate that vertical growths of the wall specimens during Tests 1 to 4, which had the same design axial load of $0.10A_g f'_c$, were very similar during cycles up to 2.0% drift, whereas the vertical growth of the wall with low axial load (Test 5) was larger than that of the other walls for cycles up to 2.0% drift. For Tests 4 and 5, during subsequent cycles to 3.0% drift, wall vertical growth rate was slower or no vertical growth was experienced, due to buckling of longitudinal reinforcement at both wall boundaries.

The comparisons indicate that the analytical model is adequate in capturing the vertical growth of four of the wall specimens (Test 1 to Test 4). However, the analytical model tends to keep the growth rate observed during the previous cycles for specimen RW-A15-P2.5-S64, the experimentally-observed growth of which was subdued at larger drifts. The analytical model well-predicts the residual vertical growth at zero lateral displacement for specimens RW-A20-P10-S38 and RW-A15-P10-S78 at all drift levels. On the other hand, the model reasonably predicts the residual vertical growth for the other specimens at all drift levels, except 3%.

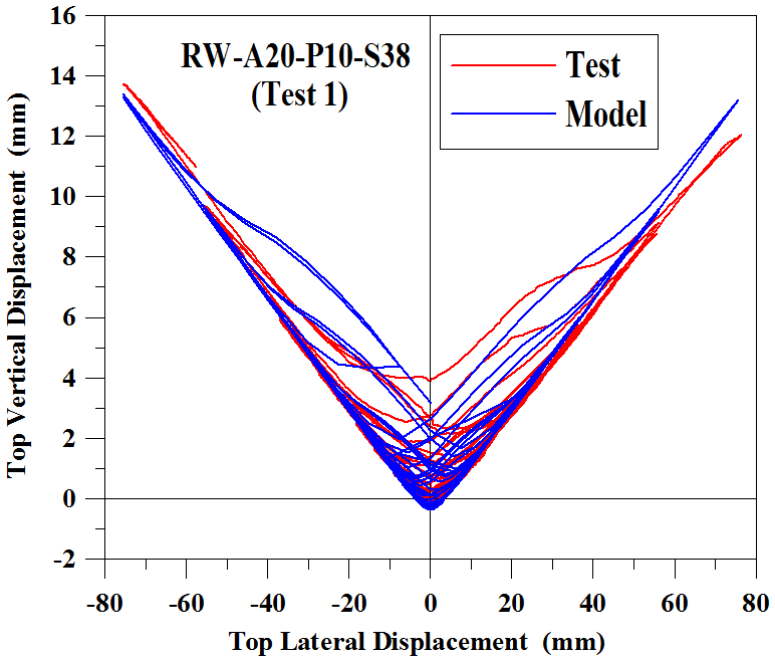

Figure 5.16. Vertical Growth vs. Lateral Displacement for RW-A20-P10-S38.

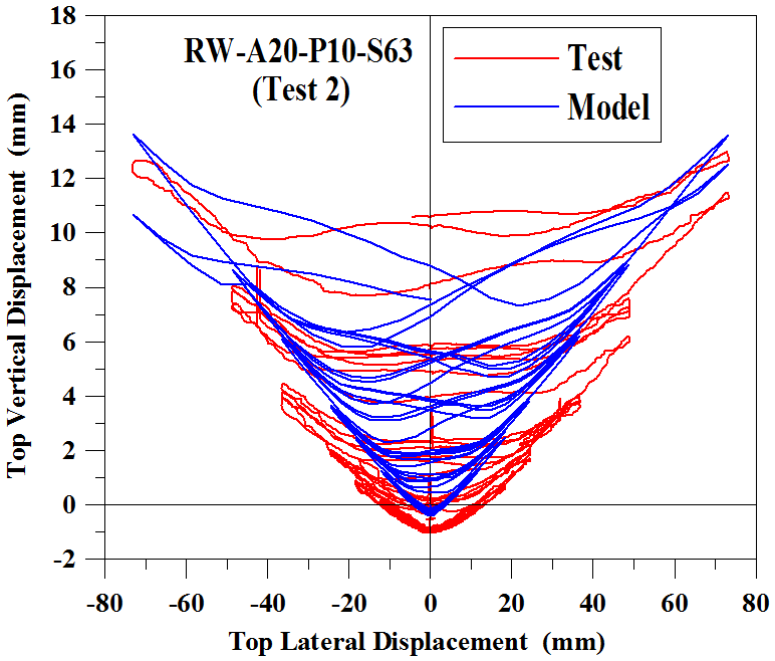

Figure 5.17. Vertical Growth vs. Lateral Displacement for RW-A20-P10-S63.

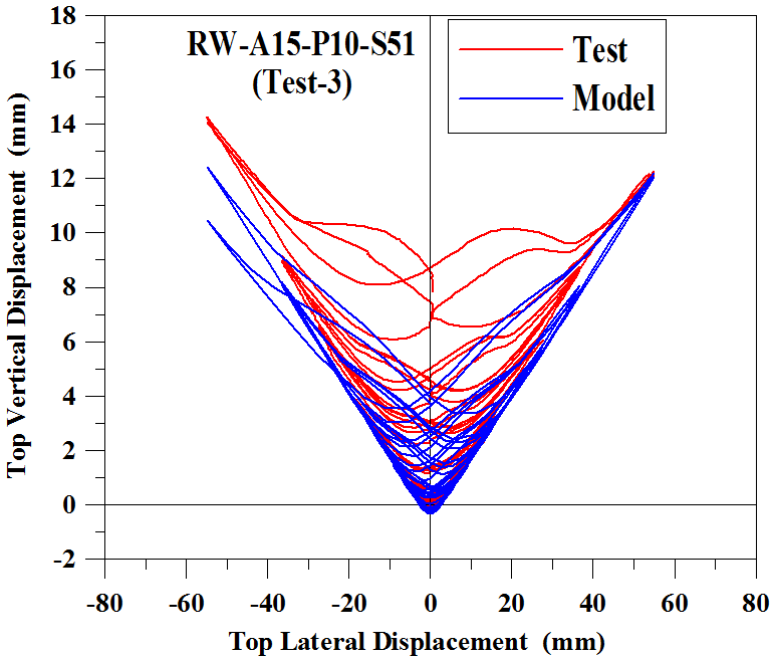

Figure 5.18. Vertical growth vs. lateral displacement for RW-A15-P10-S51.

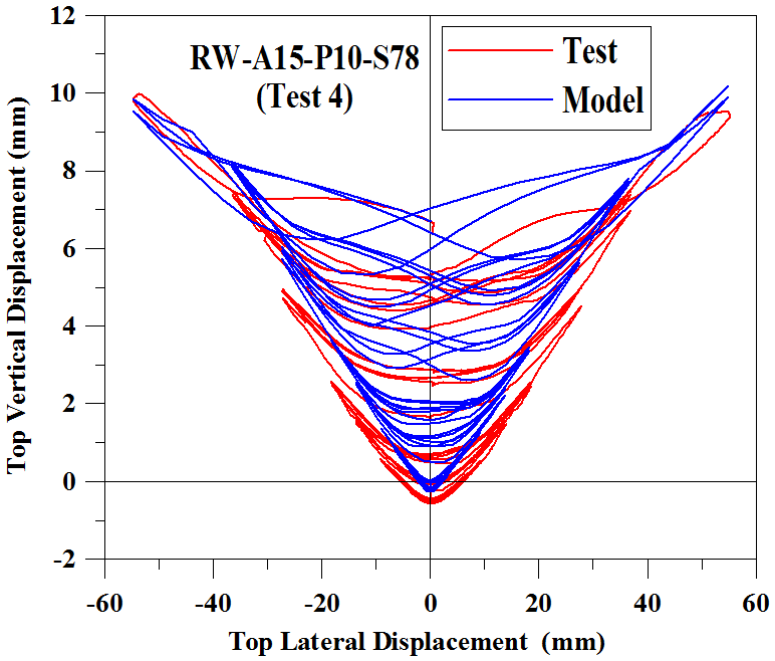

Figure 5.19. Vertical growth vs. lateral displacement for RW-A15-P10-S78.

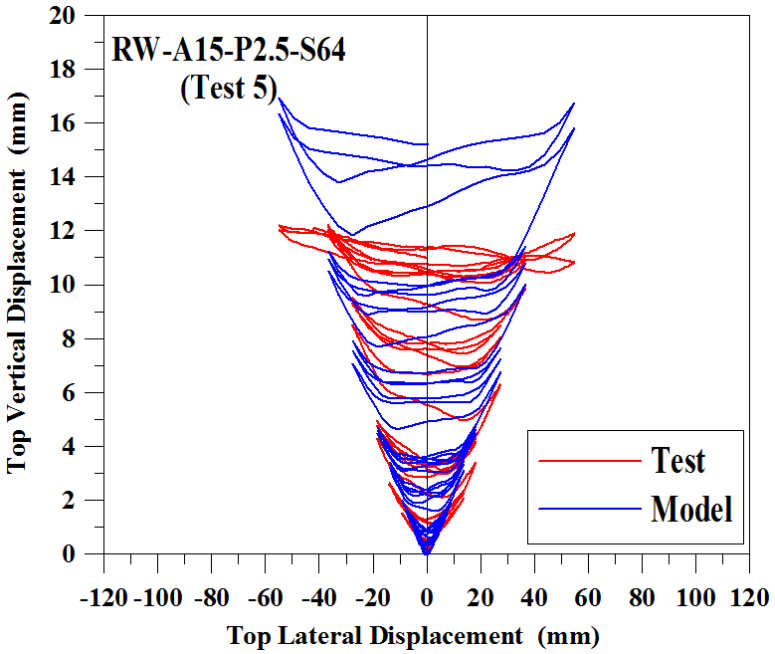

Figure 5.20. Vertical growth vs. lateral displacement for RW-A15-P2.5-S64.

5.5. Lateral Displacement Profiles

5.5.1. Total Displacement Profiles

The total lateral displacement measurement method used during the experiments was presented in Section 4.3.1. Analytically-predicted profiles of total lateral displacement, were obtained by using the horizontal degrees of freedom at the nodes of the analytical model. The experimentally-measured and analytically-predicted lateral displacement profiles are compared for Tests 1 to 5 in Figure 5.21 to Figure 5.25, respectively. Experimentally-measured profiles for wall specimens in Tests 1 to 4, which had the same design axial load levels of 0.10Agf'c, are almost linear over the wall height at all applied lateral drift levels. The analytical model estimates reasonably well the displacement profiles for these wall specimens. The analytical model predicts almost linear displacement profiles for all drift levels except the highest drift level. The model slightly underestimates wall lateral displacements at a height of lw/2 (610 mm) from the wall base, by approximately 10-15% for specimen RW-A15-P10-S78. For RW-A15-P2.5-S64, with a low axial load level of $0.025A_g f'_c$, experimentally-measured displace-

ment profiles are almost linear at all lateral drift levels except 3.0%, where lateral displacements at low elevations are much larger than expected, due to the premature sliding shear failure experienced by this specimen. For this specimen, the correlation between the analytical and experimental lateral displacement profiles is satisfactory at lower drift levels of 0.5% and 0.75%, whereas the analytical model tends to significantly underestimate wall lateral displacements at lower wall elevations at higher drift levels.

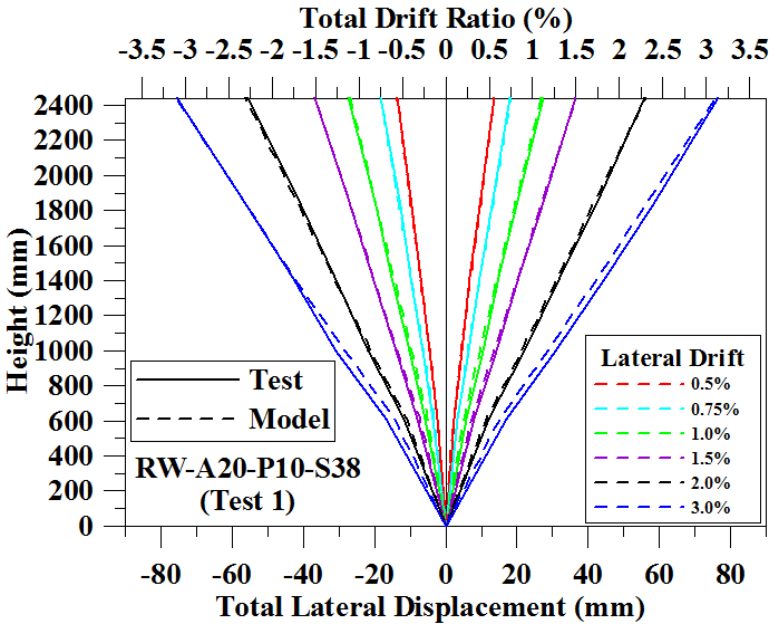

Figure 5.21. Total Lateral Displacement Profile for Specimen RW-A20-P10-S38.

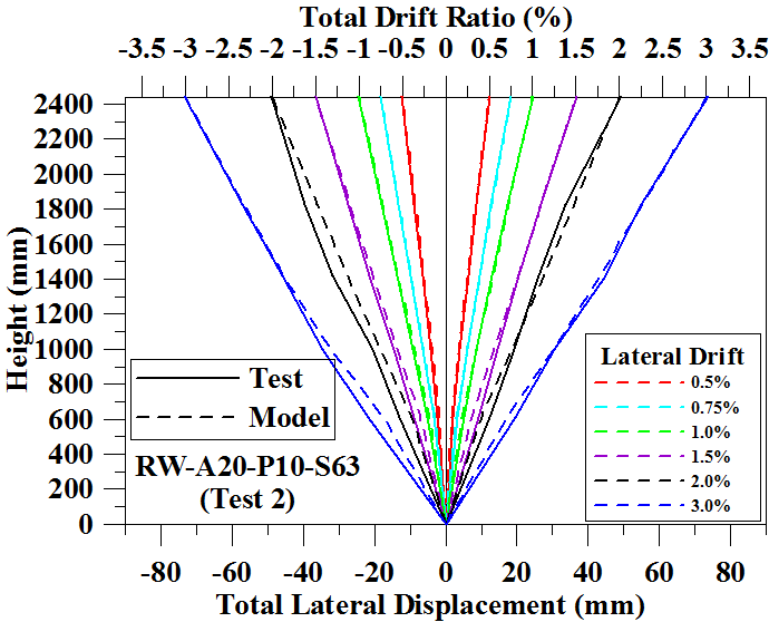

Figure 5.22. Total Lateral Displacement Profile for Specimen RW-A20-P10-S63.

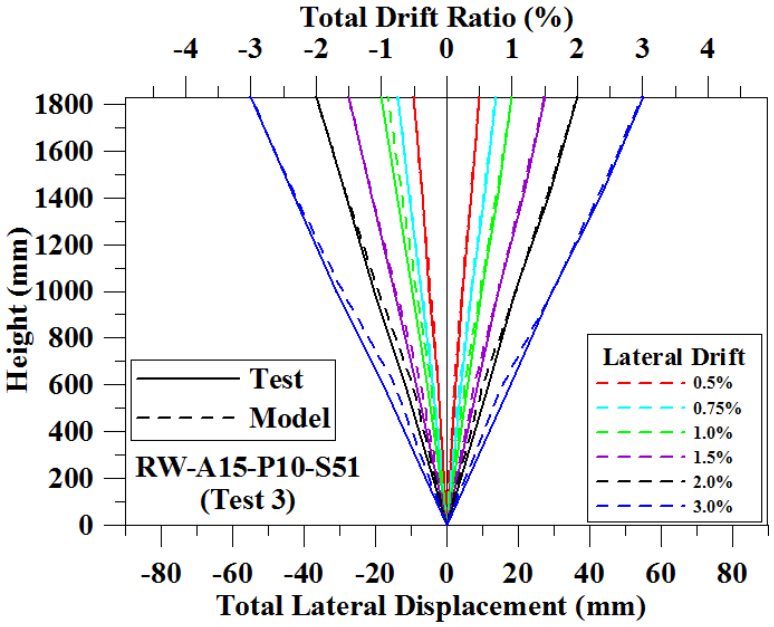

Figure 5.23. Total Lateral Displacement Profile for Specimen RW-A15-P10-S51.

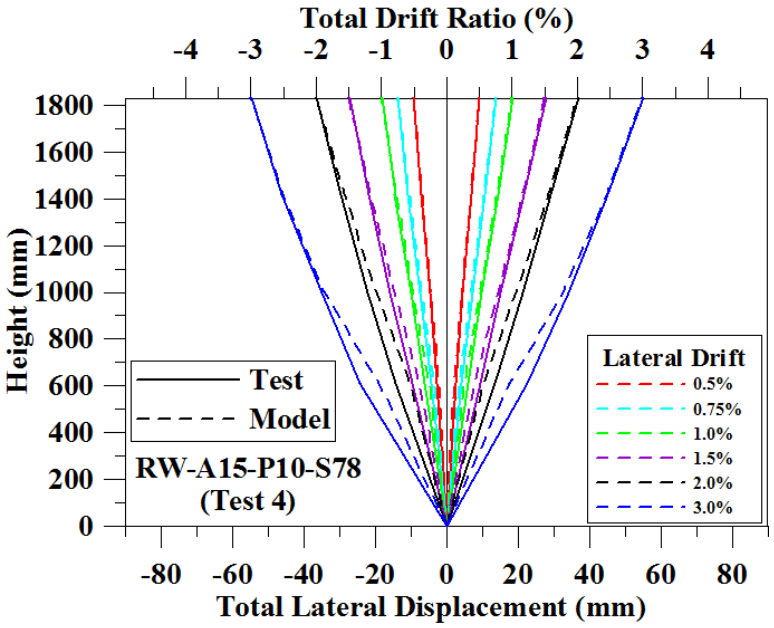

Figure 5.24. Total Lateral Displacement Profile for Specimen RW-A15-P10-S78.

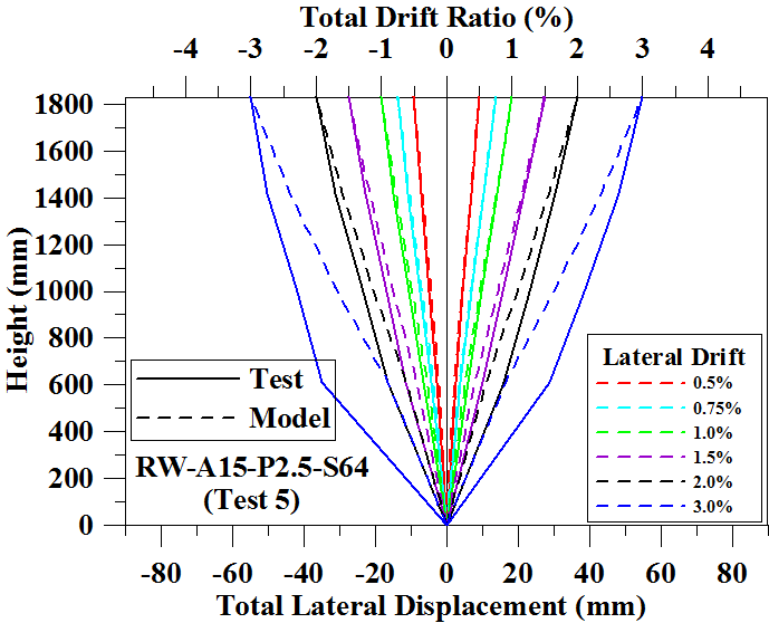

Figure 5.25. Total Lateral Displacement Profile for Specimen RW-A15-P2.5-S64.

5.5.2. Flexural Displacement Profiles

In this section, experimentally-measured and analytically-predicted flexural lateral displacement profiles of the wall specimens are compared. In both analytical and experimental results, flexural displacement profiles were calculated at peak displacements in positive and negative loading direction, during the first loading cycle to each drift level. The number of vertical model elements was adjusted so as to agree with the locations of sensors placed on the wall specimens during the tests in order to perform consistent comparisons between analytically-predicted and experimental-measured displacement profiles, at elevations of 610 mm, 1000 mm, 1420 mm and 1830 mm (for aspect ratio of 1.5) and 2440 mm (for aspect ratio of 2.0) from wall base.

The flexural displacement profiles are compared for Tests 1 to 5, in Figure 5.26 to Figure 5.30, respectively. For all specimens, the flexural displacement profiles follow a nonlinear trend up to $l_w/2$(610 mm), and beyond $l_w/2$ the flexural displacement profiles are almost linear over the wall height. It can be clearly seen that estimated profiles of flexural deformations by the analytical model capture the distribution of the nonlinear flexural deformations along the wall height for all test specimens, except RW-A15-P2.5-

S64, which suffered premature shear sliding failure. As seen in Figure 5.26, accurate predictions of flexural displacement profiles were obtained for specimen RW-A20-P10-S38. It can be observed in Figure 5.27 that the analytical model overestimates the experimental results for RW-A20-P10-S63 at high drift levels such as 1.5%, 2.0% and 3.0%, and for RW-A15-P10-S51 the model predicts flexural displacement profiles with reasonable accuracy at all drift levels except positive 3.0%. In addition, as depicted in Figure 5.29, for RW-A15-P10-S78, the analytical model agrees with the trend of the experimental results at all drift levels. For specimen RW-A15-P2.5-S64, at all drift levels, flexural displacement was significantly overestimated.

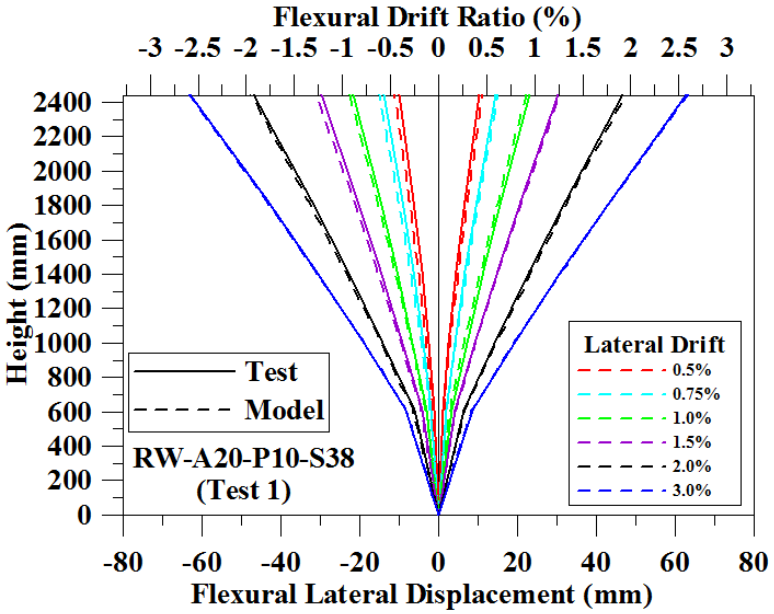

Figure 5.26. Flexural Displacement Profile for Specimen RW-A20-P10-S38.

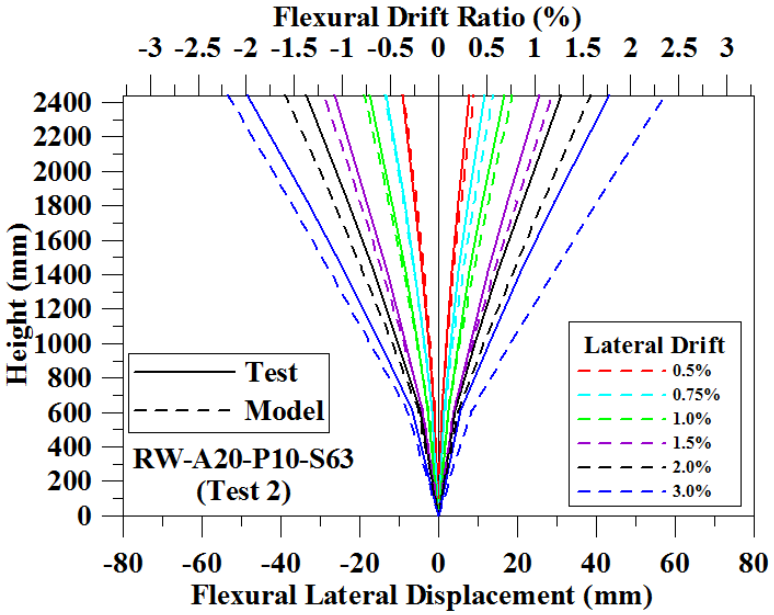

Figure 5.27. Flexural Displacement Profile for Specimen RW-A20-P10-S63.

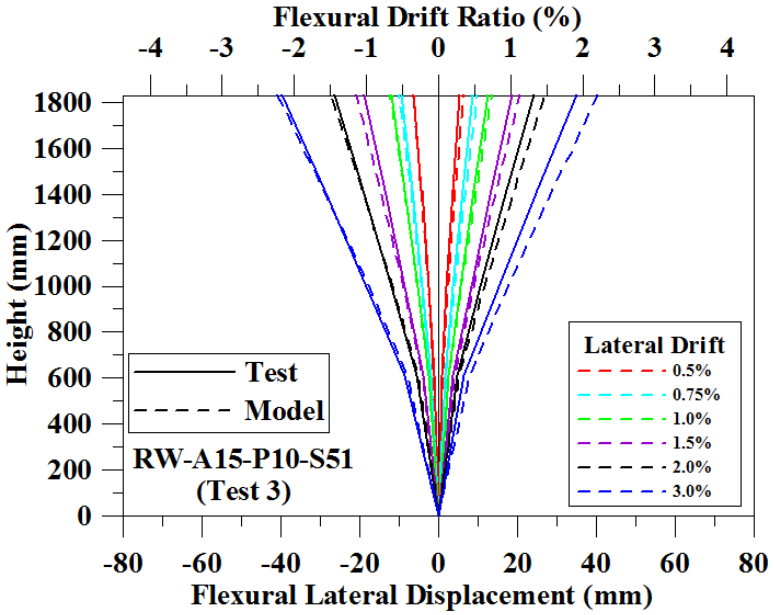

Figure 5.28. Flexural Displacement Profile for Specimen RW-A15-P10-S51.

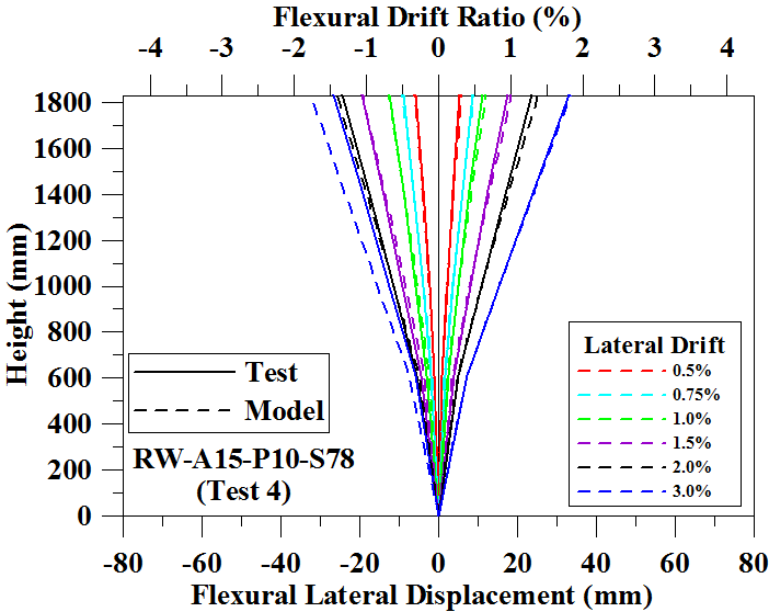

Figure 5.29. Flexural Displacement Profile for Specimen RW-A15-P10-S78.

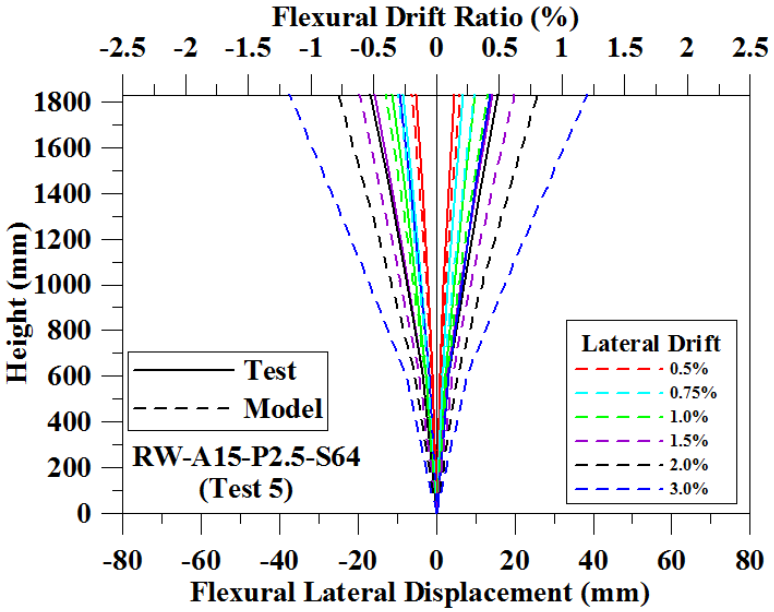

Figure 5.30. Flexural Displacement Profile for Specimen RW-A15-P2.5-S64.

5.5.3. Shear Displacement Profiles

The experimental and analytical shear displacement profiles of the specimens are compared in this section. In both analytical and experimental results, shear displacement profiles were obtained at peak lateral displacement points in positive and negative

loading direction for the first loading cycle to each drift level.

The experimentally-measured and analytically-estimated shear displacement profiles are compared for Tests 1 to 5 in Figure 5.31 to Figure 5.35, respectively. The shapes of the shear deformation profiles obtained experimentally and analytically agree reasonably well, meaning that the model captures the experimentally-observed concentration of shear deformations over the plastic hinge region (up to height of approximately $l_w/2$ = 610 mm). Moreover, the magnitudes of shear deformations increase with increasing shear stress demand at flexural capacity, especially for walls with high shear stress demand levels such as RW-A20-P10-S63 (Test 2), RW-A15-P10-S78 (Test 4), and RW-A15-P2.5-S64 (Test 5). The analytical model provides reasonable estimations for the shear deformation profiles at low and moderate drift levels for Test 3 and Test 4. The analytical results underestimate and overestimate the experimentally-measured shear displacement profiles at larger drift levels for Test 1 and Test 2, respectively. For Test 5, the shear displacement profiles are underestimated by the analytical model, due to the unexpected shear sliding failure experienced during that particular test.

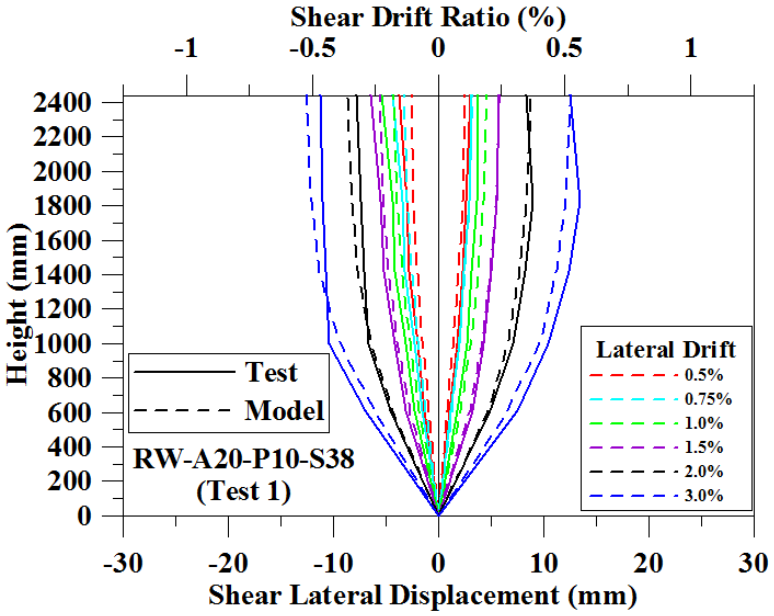

Figure 5.31. Shear Displacement Profile for Specimen RW-A20-P10-S38.

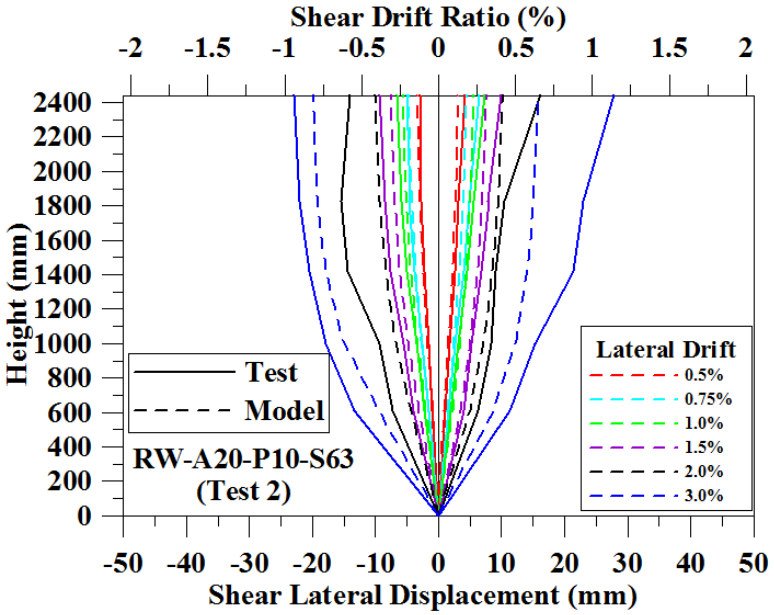

Figure 5.32. Shear Displacement Profile for Specimen RW-A20-P10-S63.

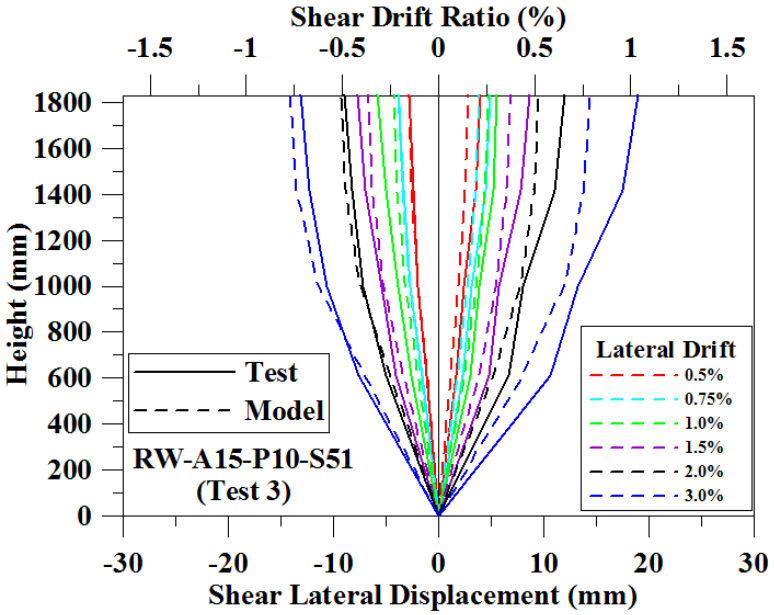

Figure 5.33. Shear Displacement Profile for Specimen RW-A15-P10-S51.

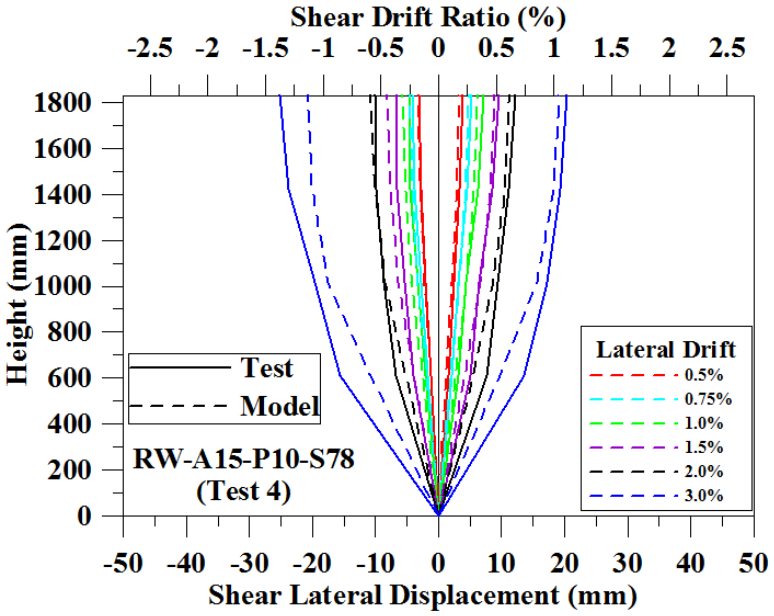

Figure 5.34. Shear Displacement Profile for Specimen RW-A15-P10-S78.

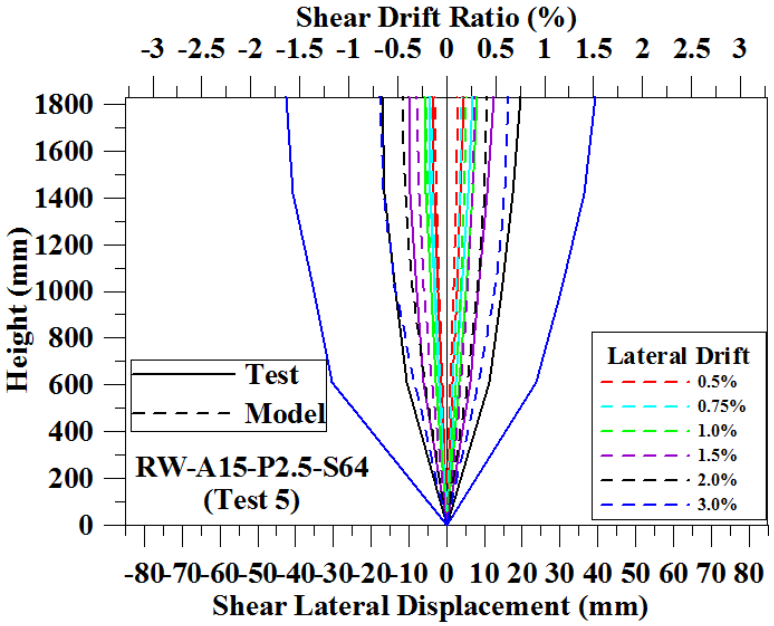

Figure 5.35. Shear Displacement Profile for Specimen RW-A15-P2.5-S64.

5.5.4. Contributions of Flexural and Shear Components to Top Lateral Displacement

Contributions of shear deformations to top lateral displacement obtained from experimental and analytical results for Tests 1 to 5 are compared in Figure 5.1 to Figure

5.5, respectively. Contributions of shear sliding failure deformations to top lateral displacement are also considered in the experimental results. Therefore, sum of the flexural and shear deformation contributions is not equal to 100% in the experimental results. The contribution of each deformation component was calculated during the first loading cycle in both positive and negative loading directions at all applied drift levels. The analytical model accurately predicts the contributions of flexural and shear deformations for Tests 1 to Test 4. For Test 5, the analytical model predicts 14% higher contribution of flexural deformation. As shown in Table 5.1, the average shear and flexural deformation contributions of all drift levels are estimated reasonably well by the analytical model for all specimens except RW-A15-P2.5-S64, which suffered premature shear sliding failure.

Table 5.1. Average Contributions of Flexural and Shear Deformations.

Contributions (%)		Specimen				
		RW-A20-P10-S38	RW-A20-P10-S63	RW-A15-P10-S51	RW-A15-P10-S78	RW-A15-P2.5-S64
Flexure	Test	77	72	63	66	55
	Model	80	76	67	64	69
Shear	Test	21	26	35	32	41
	Model	20	24	33	36	31

5.6. Cracking Patterns

In this section, cracking patterns obtained from experimental observations and analytical predictions are compared at force-controlled and displacement-controlled load cycles. The aim of this comparison is to assess the capability of the analytical model to capture the orientation of cracks, and their propagation with increasing lateral load or displacement.

5.6.1. Specimen RW-A20-P10-S38 - Test 1

This specimen had horizontal and vertical web reinforcement ratios of 0.0027, which are slightly larger than the ACI 318-11 (Section 21.9.2) minimum requirement of 0.0025 for special structural walls. Comparison of the experimentally-observed and analytically-predicted cracking patterns for specimen RW-A20-P10-S38 at lateral drift levels of 0.38%, 0.56% and 1.5% are shown in Figure 5.39. In the experiment, at a lateral drift level of 0.38%, flexural and shear cracks formed closer to the top of the wall specimen and appeared over one half of the wall height prior to reaching the yield load (Figure 5.36a). During this loading cycle, the analytical model reasonably captures the crack orientation but produces more cracks compared to the experiment. When lateral drift was increased to 0.56% (Figure 5.36b), cracking in both experimental and analytical results propagated towards the top of the wall up to the wall height of $3/4h_w$. However, at larger drift levels, up to a lateral drift ratio of 1.5%, the cracking pattern did not change significantly in both the experimental and the analytical results as shown in Figure 5.36c. The orientation of cracks observed in the experiment is estimated reasonably well by the model.

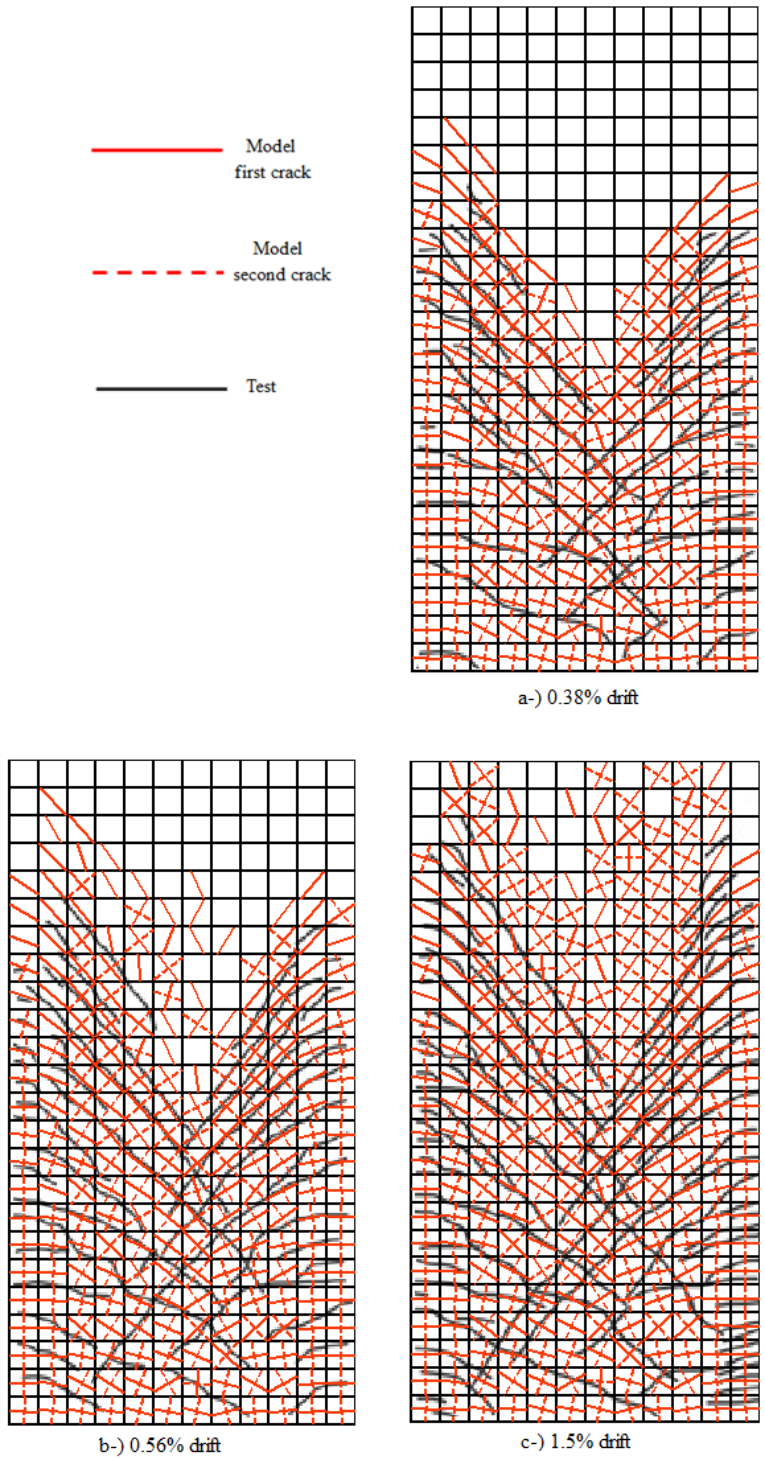

Figure 5.36. Cracking Patterns for Specimen RW-A20-P10-S38, Test 1.

5.6.2. Specimen RW-A20-P10-S63 - Test 2

This specimen was characterized by higher level of shear stress at flexural yielding compared to the previous specimen, which was achieved by approximately doubling the

value of boundary and web reinforcement.

Figure 5.37 compares the experimentally-observed and analytically-predicted cracking patterns for specimen RW-A20-P10-S63 at lateral load level of 389.66 kN (yielding of the boundary reinforcement, V_y)) and lateral drift levels of 0.75% and 1.5%. The initiation of cracking was observed in the experiment during the first cycle of the second force-controlled load level ($V_y/3$; 93 kN), including one or two inclined (shear) cracks on each side of the wall up to the wall height of 0.25lw. With increasing lateral load (force-controlled levels), horizontal flexural cracks developed at the wall boundaries and new inclined cracks formed over the wall height leading to the cracking pattern at the yielding of the boundary reinforcement shown in Figure 5.37a.

It can be observed from the figure that experimentally-measured and analytically-predicted cracking patterns spread approximately up to the wall height of hw/2 (122 cm or 48 in.) and along the wall height, respectively. At this level of lateral load, the analytically-predicted cracking pattern is characterized by flexural cracks at the wall boundaries and shear cracks within the web of the wall, which is consistent with experimentally-observed crack patterns and orientations (Figure 5.37a). With increasing lateral load (force-controlled levels) or lateral displacement (displacement-controlled levels), inclined cracks continued to propagate along the wall height in both experimental and analytical results. Experimental and analytical cracking patterns are very similar at the lateral drift level of 0.75% as shown in Figure 5.37b. In addition, it can be observed in Figure 5.37c that when increasing lateral drift to 1.5%, the cracking patterns did not change significantly since most of the cracks were formed at lower drift levels. The analytical model captures well the propagation of cracks at the drift level of 1.5%.

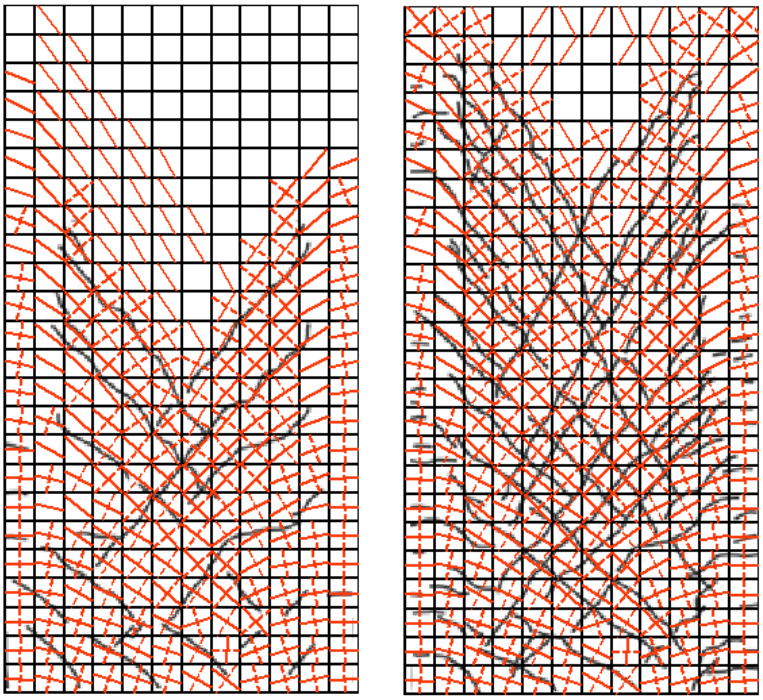

Figure 5.37. Cracking Patterns for Specimen RW-A20-P10-S63, Test 2.

5.6.3. Specimen RW-A15-P10-S51 - Test 3

The third wall specimen had the same longitudinal boundary reinforcement and axial load level as the first wall specimen (RW-A20-P10-S38), but a lower aspect ratio (1.5 versus 2.0) and a slightly higher web reinforcement ratio (0.0032 versus 0.0027); the lateral load corresponding to the nominal moment capacity was larger, leading to a higher design shear stress than for RW-A20-P10-S38 ($5.1\sqrt{f'_c}$ psi versus $3.8\sqrt{f'_c}$ psi or $0.43\sqrt{f'_c}$ MPa versus $0.32\sqrt{f'_c}$ MPa).

Figure 5.38 compares experimentally-observed and analytically-predicted cracking patterns for specimen RW-A15-P10-S51 at lateral drift levels of 0.375%, 1.0% and 3.0%. The initiation of cracking in the experiment occurred during the first cycle of the third force-controlled level ($2/3V_y$; 240 kN). As depicted in the Figure 5.38, the experimental cracking pattern consisted of several horizontal flexural cracks along the wall boundaries and three major inclined (shear) cracks on each side of the wall, propagating from the wall boundaries at the wall-foundation interface towards the wall center up to the height of approximately 0.5hw above the wall-foundation interface.

After increasing the lateral drift to 0.375% (Figure 5.38a), the major diagonal cracks propagating from the wall boundaries towards the top of the wall specimen up to the height of approximately $3/4h_w$ was observed during the experiment as well as in the analytical results; the model predicts the formation of cracks approximately up to elevations of $3/4h_w$. Further crack propagation in the experiment can be observed at the drift level of 1.0% (Figure 5.38b), where diagonal cracks extended to the top of the wall specimen leaving a small uncracked portion in the middle of the wall near the wall top. It can be observed from the Figure 5.38b that the orientation of cracks agrees reasonably well with the experimentally-observed cracking pattern at the lateral drift of 1.0%. The experimentally-observed cracking pattern at lateral drift of 3.0% (Figure 5.38c) does not differ significantly from the cracking pattern at lateral drift of 1.0%, i.e., no new cracks develop at intermediate drift levels. The crack orientations in the model prediction agrees reasonably well with the orientation of cracks observed on specimen RW-A15-P10-S51.

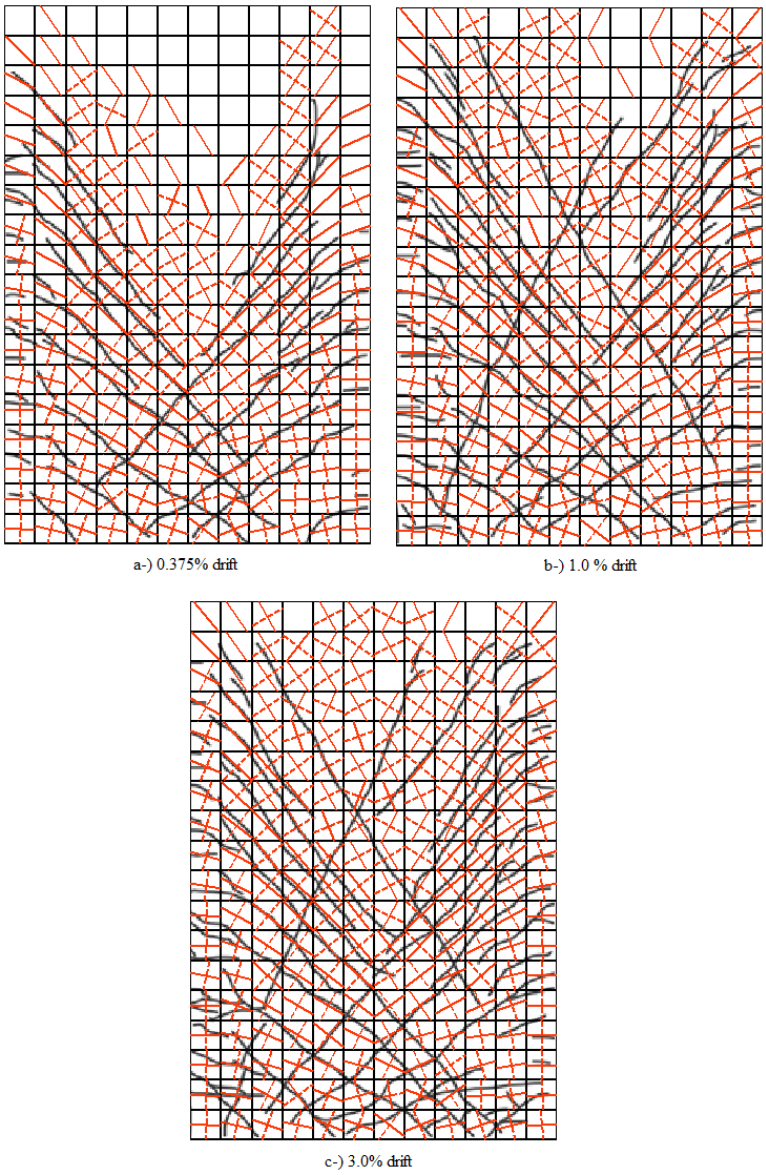

Figure 5.38. Cracking Patterns for Specimen RW-A15-P10-S51, Test 3.

5.6.4. Specimen RW-A15-P10-S78 - Test 4

Specimen RW-A15-P10-S78 had the same level of axial load and aspect ratio (1.5) as Test 3, but much higher average shear stress (7.0 $\sqrt{f'_c}$ psi versus 4.9 $\sqrt{f'_c}$ psi or 0.58 $\sqrt{f'_c}$ MPa versus 0.41 $\sqrt{f'_c}$ MPa). Figure 5.39 compares experimentally-observed and analytically-predicted crack patterns for specimen RW-A15-P10-S78 at lateral drift levels of 0.75% and 2.0%. The initiation of cracking was observed in the experiment during the first cycle of the third force-controlled level, at the lateral load level of 356

kN. The experimentally-observed cracking pattern included horizontal (flexural) cracks between the wall-foundation interface to a height of approximately l_w (1220 mm) at wall edges and three major inclined (shear) cracks on each side of the wall.

Although the cracking pattern of this specimen was similar to that of RW-A15-P10-S51, the propagation of inclined cracks was more extensive in RW-A15-P10-S78. As can be observed in Figure 5.39a, at a lateral drift of 0.75%, the inclined (shear) cracks propagate to the top of the wall specimen; accordingly, the analytical model predicts cracking in all RC panel elements in the wall model. Figure 5.39b depicts that experimental and analytical cracking patterns at the drift level of 2.0% are almost identical to that at 0.75%, suggesting that that for increasing levels of applied lateral drift, the cracking pattern does not change in both experimental and analytical results, but the crack widths increase.

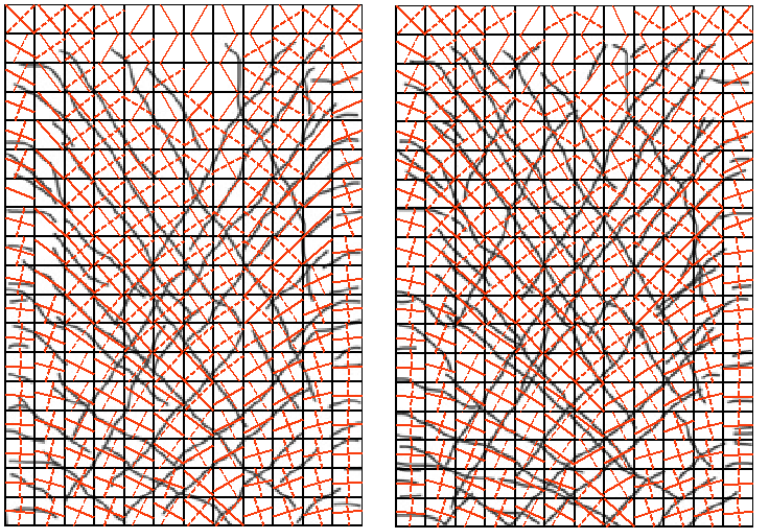

Figure 5.39. Cracking Patterns for Specimen RW-A15-P10-S78, Test 4.

5.6.5. Specimen RW-A15-P2.5-S64 - Test 5

This specimen had the same reinforcement configuration as specimen RW-A15-P10-S78, except a slightly smaller web reinforcement ratio. The main difference between these two specimens was the axial load level; the axial load level of RW-A15-P2.5-S64 was only one-fourth of that of RW-A15-P10-S78 (0.016 $P/A_g f'_c$ versus 0.064

$P/A_g f'_c$).

The comparison of experimentally-observed and analytically-predicted cracking patterns at lateral drift levels of 0.5% and 2.0% are presented in Figure 5.40. First cracking in RW-A15-P2.5-S64 in the experiment is formed during the first cycle of the second force-controlled loading stage ($V_y/4$; 156 kN) and consisted of two short inclined (shear) cracks on each side of the wall. The propagation of cracks in this wall was similar to that of RW-A15-P10-S78; however, the angle of inclined cracks obtained experimentally and analytically were shallower in RW-A15-P2.5-S64; the inclination of inclined cracks increased when they became closer to the opposite boundary zone. At the applied lateral drift of 0.5% (Figure 5.40a), the cracking pattern in the experiment propagated to the top of the wall specimen and this was also predicted by the analytical model. In addition, the model predicted reasonably well the orientation of cracks over the wall height (Figure 5.40b). As shown in Figure 5.40b, the experimentally-observed cracking pattern at the lateral drift of 2.0% is not significantly different from the pattern observed at 0.5% drift (i.e., cracks are slightly denser, but their orientation remains the same), whereas the cracking pattern predicted by the analytical model at 2.0% drift is identical to that of 0.5%.

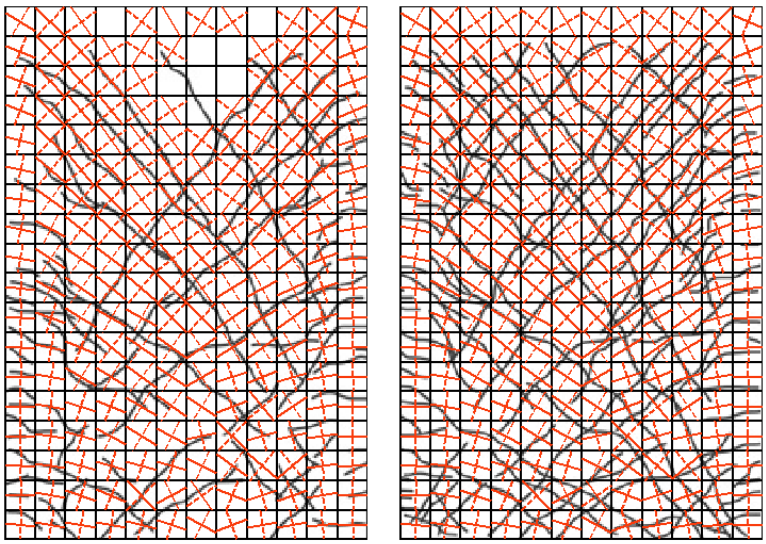

Figure 5.40. Cracking Patterns for Specimen RW-A15-P2.5-S64, Test 5.

5.7. Local Responses

5.7.1. Vertical Strains

Comparisons between experimentally-measured and analytically-predicted profiles of vertical strains at the bottom of the wall specimens, corresponding to the first loading cycle in the positive direction to lateral drifts of 0.5%, 0.75%, 1.0%, 1.5% and 2.0% for Tests 2-5 are presented through Figures 5.41-5.44, respectively. Vertical strain profile comparisons for Test 1 are not presented due to unreliable readings from the LVDTs encountered during that particular test. For the rest of the tests, similar strain profile trends were observed at other drift levels, as well, for loading cycles in the negative direction. Therefore, limited yet representative results are presented. Experimentally-measured vertical concrete strains were obtained from four vertical LVDTs located at 102 mm, 330 mm, 889 mm and 1180 mm along the length of the wall specimens, over the LVDT gauge length of 356 mm, whereas analytically-predicted strain profiles were obtained from strains in at 0 mm, 102 mm, 203 mm, 305 mm, 406 mm, 508 mm, 609 mm, 711 mm, 813 mm, 914 mm, 1016 mm, 1117 mm and 1220 mm along the length of the wall models, along a gauge length of 406 mm from the wall base (along the height of bottom four model elements).

It can be observed in the figures that the analytical model accurately represents the vertical strain profiles at drift levels of 0.5%, 0.75%, 1.0% and 1.5% for all four specimens considered. Both tensile and compressive strains at wall boundaries are predicted with approximately 85% accuracy. However, at the drift level of 2.0%, vertical strain profiles were relatively poorly predicted. At this drift level, analytical results reasonably capture the experimentally-measured tensile strains at the wall boundary for Tests 2 and 4, whereas compressive strains are relatively well-predicted for Tests 2 and 3.

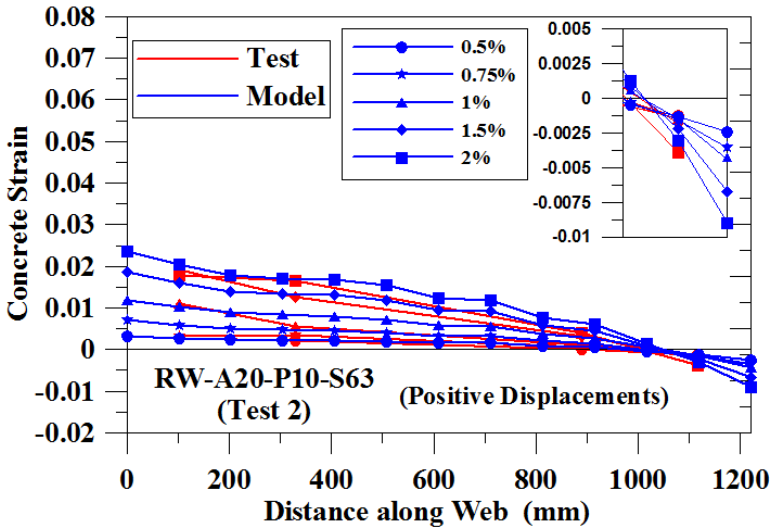

Figure 5.41. Vertical Strain Profiles for Specimen RW-A20-P10-S63, Test 2.

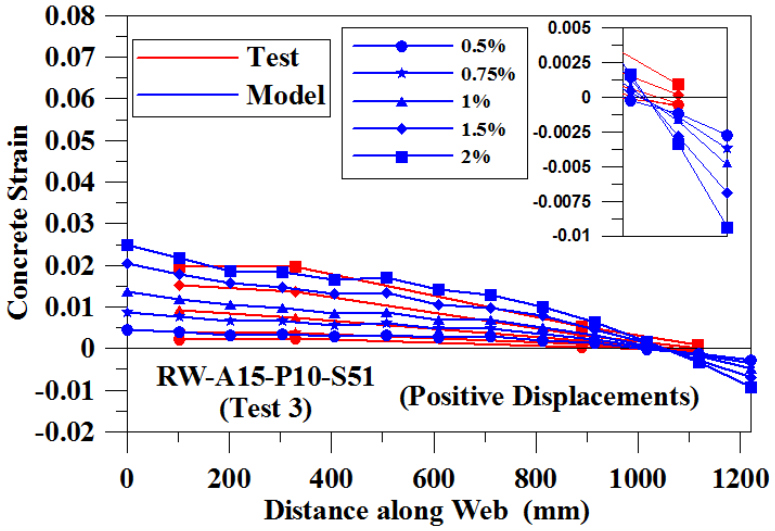

Figure 5.42. Vertical Strain Profiles for Specimen RW-A15-P10-S51, Test 3.

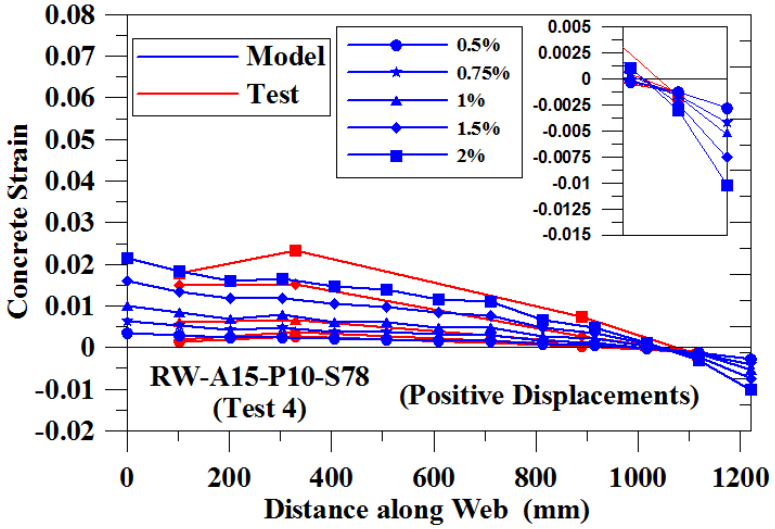

Figure 5.43. Vertical Strain Profiles for Specimen RW-A15-P10-S78, Test 4.

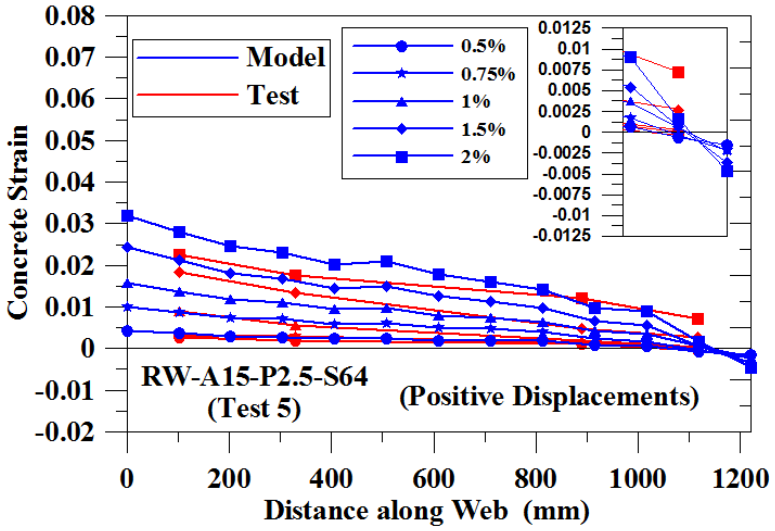

Figure 5.44. Vertical Strain Profiles for Specimen RW-A15-P2.5-S64, Test 5.

5.7.2. Base Rotations

Experimentally-measured and analytically-predicted rotations over the bottom 610 mm of the wall specimens (i.e., lw/2, assumed plastic hinge length) corresponding to peak positive and negative drift levels of 0.5%, 0.75%, 1.0%, 1.5%, 2.0% and 3.0% for Tests 2 to 5 are compared in Figure 5.45 to Figure 5.48, respectively. Comparison of rotations for Test 1 is not presented due to unreliable readings from the displacement sensors during that test. Experimental rotations were measured using two vertical wire

potentiometers mounted to wall ends by use of Equation 4.2, whereas corresponding rotations for the analytical model were derived from vertical displacement differences between boundary nodes of the model at a height of 610 mm from the bottom of the wall, divided by length of the wall. Experimentally-measured rotations are in reasonable agreement with analytically-predicted rotations at the selected drift levels for specimens RW-A20-P10-S63, RW-A15-P10-S51 and RW-A15-P10-S78. For specimen RW-A15-P2.5-S64, analytical predictions were not able to capture the experimental rotations even at low drift levels. A probable reason for this discrepancy is that premature shear sliding observed at the base of this wall specimen resulted in unreliable readings from the vertical boundary sensors (wire potentiometers) that were used for calculation of the experimental rotations.

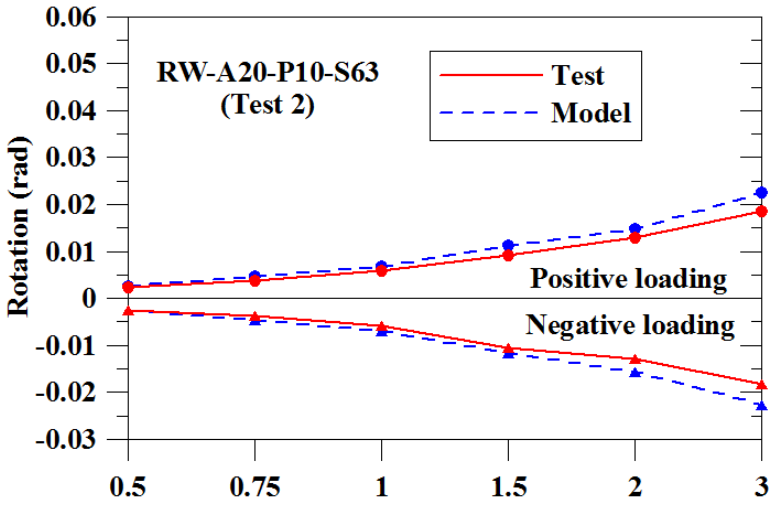

Figure 5.45. Base Rotations for Specimen RW-A20-P10-S63, Test 2.

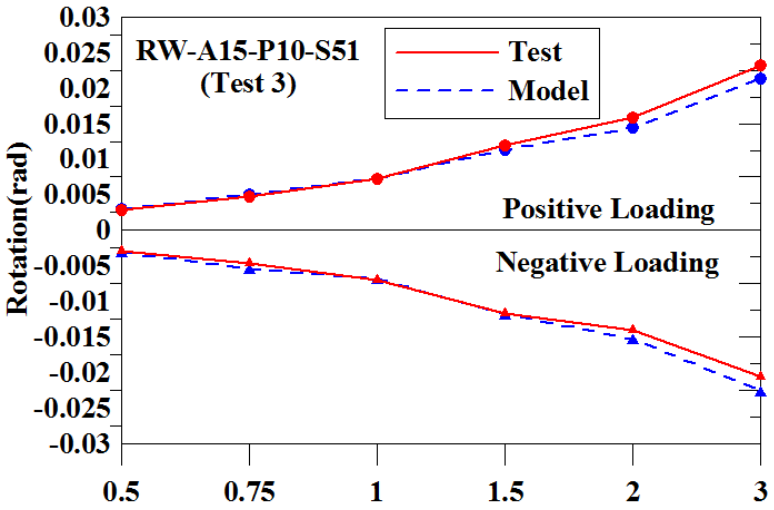

Figure 5.46. Base Rotations for Specimen RW-A15-P10-S51, Test 3.

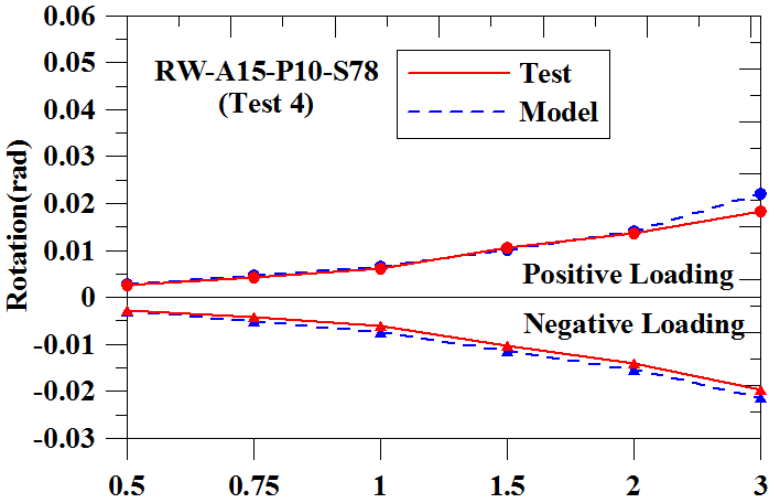

Figure 5.47. Base Rotations for Specimen RW-A15-P10-S78, Test 4.

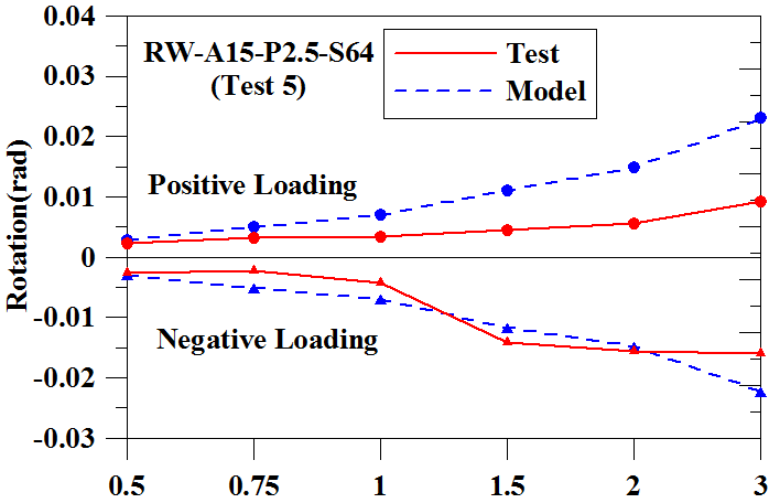

Figure 5.48. Base Rotations for Specimen RW-A15-P2.5-S64, Test 5.

5.8. Overview

The aim of this chapter was to present the results of detailed correlation studies conducted between the analytically-predicted and experimentally-observed responses of the wall specimens investigated in this study, at various behavioral levels. The analytical model was subjected to the same loading conditions applied during testing (e.g., loading protocol, applied axial load). A refined discretization was used for the model in order to predict the responses at specific locations where instrumentation was provided in the tests. The correlation of the experimental and analytical results was investigated in detail, at various response levels (both global and local) and locations.

Response comparisons with the test results on the medium-rise wall specimens revealed that the model provides reasonable predictions of the lateral load capacity, stiffness degradation, hysteretic shape, ductility, and pinching characteristics of the wall specimens investigated. Wall stiffness was not accurately captured by the analytical model at drift levels lower than 0.5%, but the model provides accurate stiffness predictions at higher drift levels. The lateral load capacity of the walls was adequately estimated by the analytical model. Cyclic stiffness degradation and pinching behavior in the load-displacement response was also reasonably captured. Overall, important characteristics of the global load-displacement response was accurately represented by the analytical model for all specimens except RW-A15-P2.5-S64, which suffered premature shear sliding failure.

The analytical model also provided reasonably accurate estimates of the relative contribution of flexural and shear deformations to wall lateral displacements. For specimen RW-A15-P2.5-S64 (Test 5), flexural deformations were significantly overestimated by the analytical model. The reason for the discrepancies observed for that particular wall specimen is the unexpected formation of a premature horizontal crack close to the bottom of the specimen, resulting in shear sliding behavior dominating the overall response, which could not be predicted by the model. The total, flexural and shear displacement profiles along the height of the remaining four wall specimens were also predicted by the analytical model with reasonable accuracy. The The analytical

model accurately captured the vertical growth and the residual growth (at zero lateral displacement) at the top of the four specimens (Test 1 to Test 4), at all drift levels.

In terms of local response comparisons (i.e. crack orientations, vertical strain profiles along the base of the wall, and wall rotations at the base), the analytical model provides adequate results, except for specimen RW-A15-P2.5-S64. The vertical strain profiles along the base of the wall at various drift levels were particularly well-predicted. As discussed in Section 3.3.4, the model provides better vertical strain profile predictions by increasing the number of constitutive model elements used, without altering their square-like geometry. As aforementioned in Section 5.1.2, for better prediction of the response and failure mode of walls experiencing shear sliding failure and buckling of longitudinal boundary reinforcement, these failure modes should be implemented into the model formulation.

6. SUMMARY AND CONCLUSIONS

6.1. Summary

The aim of this study was to adopt and experimentally-validate a finite element modeling methodology for simulating the in-plane hysteretic lateral load response of moderate aspect ratio RC walls, involving significant shear flexure interaction behavior and significant contribution of nonlinear shear deformations in the wall response. The behavior of the constitutive panel (membrane) elements in the finite element model is described by the Fixed-Strut-Angle Panel Model. The constitutive model elements also incorporates behavioral response characteristics including compression softening, tension stiffening, hysteretic biaxial damage, and shear stress transfer across cracks. Improvements were made on the constitutive panel model formulation for better representation of the shear-aggregate-interlock effects in concrete and dowel action in reinforcing bars, constituting the shear stress transfer mechanism across the cracks of the constitutive panel elements.

Sensitivity studies were performed to investigate the variation in the model results with changes in various modeling parameters (aggregate interlock parameters and model discretization), wall configuration parameters (wall aspect ratio, boundary and web reinforcement ratios) and loading parameters (axial load level).

The model was extensively calibrated for five moderately-slender RC wall specimens tested by Tran and Wallace (2012), and model predictions were compared with the experimentally-observed responses all five of the rectangular, moderate-aspect-ratio wall specimens. Model results were compared with test results not only at the global lateral load - displacement response level, but also at various deformation levels at different locations.

6.2. Conclusions

The following conclusions can be reached in light of the results obtained using the analytical modeling approach adopted in this study:

- From a purely analytical point of view, the model results showed behaviorally-consistent and systematic sensitivity to variations in wall configuration. Increasing the wall aspect ratio caused the model response to become more flexure-dominant. Decreasing the reinforcement ratio on the web and boundary regions resulted in the increase and decrease of predicted shear deformation contributions, respectively, together with decrease in the predicted lateral load capacity. By increasing the axial load level, larger lateral load capacity and more pronounced pinching behavior was observed.
- Varying the parameters of the constitutive shear aggregate interlock models (within reasonable range) did not noticeably alter the model predictions. However, changing the number of model elements resulted in significant variation in the predicted vertical strain profiles at the base of a wall, indicating that a reasonably fine model discretization must be used in order to obtain reliable local deformation predictions. As well, using model elements with approximately square geometry were observed to give better response estimates.
- Response comparisons with the test results on the medium-rise wall specimens revealed that the model provides reasonable predictions of the lateral load capacity, stiffness degradation, hysteretic shape, ductility, and pinching characteristics of the wall specimens investigated. The lateral load capacity of the walls was adequately estimated by the analytical model. Cyclic stiffness degradation and pinching behavior in the load-displacement response was also reasonably captured. Overall, important characteristics of the global load-displacement response were accurately represented by the model.
- The analytical model also provided reasonably accurate estimates of the relative contributions of flexural and shear deformations to wall lateral displacements, and also captured vertical growth behavior of walls associated with yielding of longitudinal reinforcement and neutral axis migration. In terms of local response

comparisons (i.e. crack orientations, vertical strain profiles along the base of the wall, and wall rotations at the base), the analytical model provided adequate results. The vertical strain profiles along the base of a wall at various drift levels were particularly well-predicted.

- The model was incapable of simulating experimentally-observed failure modes and degradation in wall lateral load capacity associated with buckling of reinforcement and shear sliding failure, since these behavioral modes are not considered in its constitutive formulation.
- The modeling approach implemented in this study is believed to be a significant improvement towards reliable prediction of the coupled shear-flexural response of reinforced concrete structural walls under cyclic loading conditions.

6.3. Recommendations for Future Studies

Based on the outcomes of this study, the following recommendations can be made for future research on improvement of the present modeling approach for walls:

- The model should be further calibrated experimentally-validated against a wider range of experimental data on wall specimens with various geometries and reinforcement characteristics.
- More refined constitutive models representing shear aggregate interlock effects in concrete and dowel action on reinforcing steel bars can be implemented in the constitutive model formulation.
- For better prediction of the response and failure mode of walls experiencing shear sliding failure and buckling of longitudinal boundary reinforcement, these failure mechanisms should be implemented into the constitutive model formulation.
- The model can be used for conducting system analyses on coupled wall or wall-frame systems subjected to quasi-static and dynamic loading conditions, possibly upon improvement of the finite element model formulation to incorporate rotational degrees of freedom at the nodes.

REFERENCES

Bazant, Z., Y. Xiang and P. Prat, 1996, "Microplane Model for Concrete-Part I: Stress-Strain Boundaries and Finite Strain", *Journal of Engineering Mechanics*, Vol. 122, No. 3, pp. 245-254.

Belarbi, A. and T.C. Hsu, 1994, "Constitutive Laws of Concrete in Tension and Reinforcing Bars Stiffened By Concrete", *American Concrete Institute Structural Journal*, Vol. 91, No. 4, pp. 465-474.

Belarbi, A. and T.C. Hsu, 1995, "Constitutive Laws of Softened Concrete in Biaxial Tension Compression", *American Concrete Institute Structural Journal*, Vol. 119, No. 12, pp. 3590-3610.

Chang, G.A. and J.B. Mander, 1994, "Seismic Energy Based Fatigue Damage Analysis of Bridge Columns: Part I - Evaluation of Seismic Capacity", *Northwestern Center for Engineering Education Research Technical Report No.* NCEER-94-0006, State University of New York, Buffalo.

Clarke, M.J. and G.J. Hancock, 1990, "A Study of Incremental-Iterative Strategies for Non-Linear Analyses", *International Journal for Numerical Methods in Engineering*, Vol. 29, pp. 1365-1391.

Colotti, V. 1993, "Shear Behavior of RC Structural Walls", *American Society of Civil Engineering Journal of Structural Engineering*, Vol. 119, No. 3, pp. 728-746.

Dulacska, H., 1972, "Dowel Action of Reinforcement Crossing Cracks in Concrete", *American Concrete Institute Structural Journal*, Vol. 69, No. 12, pp. 754-757.

Elwood, K.J., 2002, "Shake Table Tests and Analytical Studies on the Gravity Load Collapse of Reinforced Concrete Frames", Ph.D. thesis, University of California.

Filippou, F.C., E.G., Popov and V.V. Bertero, 1983, "Effects of Bond Deterioration on Hysteretic Behavior of Reinforced Concrete Joints", *Energy and Environmental Rerearch Center Report No. 83/19 Earthquake*, Engineering Research Center, University of California, Berkeley, California.

Fischinger, M, T. Vidic, J. Selih, P. Fajfar, H.Y. Zhang and F.B. Damjanic, 1990, "Validation of a Macroscopic Model for Cyclic Response Prediction of RC Walls", in N.B. Bicanic and H. Mang (eds.), "Computer Aided Analysis and Design of Concrete Structures", Vol. 2, pp. 1131-1142.

Fischinger M., K. Rejec and T. Isakovic, 2012, "Modeling Inelastic Shear Response of RC Walls", *Proceedings of 15th World Conference on Earthquake Engineering*, Lisbon, Portugal.

Güllü, M.F., 2013, "Finite Element Modeling Reinforced Concrete Structural Walls", M.S. Thesis, Boğaziçi University.

Güllü, M.F. and K. Orakçal, 2014, "Nonlinear Finite Element Modeling of Reinforced Concrete Structural Walls", Proceedings, 2nd European Conference on Earthquake Engineering and Seismology, İstanbul, Türkiye, No. 1485.

He, X.G. and A.K.H. Kwan, 2001, "Modeling Dowel Action of Reinforcement Bars for Finite Element Analysis of Structures", *Computers and Structures*, Vol.79, No. 6, pp. 595-604.

Hofbeck, J.A., I.O. Ibrahim and A.H. Mattock, 1969, "Shear Transfer in Reinforced Concrete", *American Concrete Institute Structural Journal Proceedings*, Vol. 66, No. 2, pp. 119-128.

Hsu, T.C. 1988, "Softened Truss Model Theory for Shear and Torsion", *American Concrete Institute Structural Journal*, Vol. 85, No. 6, pp. 624-635.

Hsu, T.C. and L. Zhang, 1996 "Tension Stiffening in Reinforced Concrete Membrane

Elements", *American Concrete Institute Structural Journal*, Vol. 93, No. 1, pp. 108-115.

Hsu T.C. and R.H. Zhu, 2002, "Softened Membrane Model for Reinforced Concrete Elements in Shear", *American Concrete Institute Structural Journal* Vol. 99, No. 4, pp. 460-469.

Lefas, I.D. and M.D. Kotsovos, 1990, "Strength and Deformation Characteristics of Reinforced Concrete Walls under Load Reversals", *American Concrete Institute Structural Journal*, Vol. 87, No. 6, pp. 716-726.

Kolozvari, K., T. Tran, K. Orakcal and J. Wallace, 2014, "Modeling of Cyclic Shear-Flexure Interaction in Reinforced Concrete Structural Walls II: Experimental Validation", *Journal of Structural Engineering*.

Mander, J.B., M.J.N. Priestley and R. Park, 1988, "Theoretical Stress-Strain Model for Confined Concrete", *American Society of Civil Engineering Journal of Structural Engineering*, Vol. 114, No. 8, pp. 1804-1826.

Mansour, M.Y. and T.C. Hsu, 2005, "Behavior of Reinforced Concrete Elements under Cyclic Shear", *American Society of Civil Engineering Journal of Structural Engineering*, Vol. 131, No. 1, pp. 44-53.

Mansour, M.Y., T.C. Hsu and J.Y. Lee, 2002, "Pinching Effect in Hysteretic Loops of R/C Shear Elements", *American Concrete Institute Special Publications* , Vol. 205, p.. 293-321.

Massone, L.M.,K. Orakcal and J.W. Wallace, 2006, "Modeling Flexural/Shear Interaction in RC Walls, ACI-SP-236, Deformation Capacity and Shear Strength of Reinforced Concrete Members under Cyclic Loadings", *American Concrete Institute*, Vol. 7, pp. 127-150.

Massone, L.M., and J.W. Wallace, 2004, "Load-Deformation Responses of Slender

Reinforced Concrete Walls", *American Concrete Institute Structural Journal*, Vol. 101, No. 1, pp. 103-113.

Massone, L.M., K., Orakcal and J.W. Wallace,2009, "Modeling of Squat Structural Walls Controlled by Shear", *American Concrete Institute Structural Journal*, Vol. 106, No. 5, pp. 646-655.

Menegotto, M. and E., Pinto, 1973, "Method of Analysis for Cyclically Loaded Reinforced Concrete Plane Frames Including Changes in Geometry and Non-Elastic Behavior of Elements under Combined Normal Force and Bending", *Proceedings, International Association for Bridgy and Structural Engennering Symposium*, Lisbon, Portugal.

Mullapudi, R.T. and A.S., Ayuob, 2009, "Fiber Beam Element Formulation Using the Softened Membrane Model", *American Concrete Institute Special Publication*, Vol. 265, pp. 283-308.

Mullapudi, R.T., P. Charkhchi and A.S. Ayuob, 2009, "Evaluation of Behavior of Reinforced Concrete Shear Walls through Finite Element Analysis", *American Concrete Institute Special Publication*, Vol. 265, pp. 73-100.

Orakcal, K., 2004, "Nonlinear Modeling and Analysis of Slender Reinforced Concrete Walls", Ph.D. Thesis, Los Angeles.

Orakcal, K., J.P. Conte and J.W. Wallace, 2004, "Flexural Modeling of Reinforced Concrete Structural Walls - Model Attributes", *American Concrete Institute Structural Journal*, Vol. 101, No. 5, pp. 688-698.

Orakcal, K. and J.W. Wallace, 2006, "Flexural Modeling of Reinforced Concrete Walls - Experimental Verification", *American Concrete Institute Structural Journal*, Vol. 103, No. 2, pp. 196-206.

Orakcal, K., U. Uluğtekin and L.M. Massone, 2012, "Constitutive Modeling of Rein-

forced Concrete Panel Behavior under Cyclic Loading", *Proceedings of the 15th World Conference on Earthquake Engineering*, Lisbon, Portugal.

Özcebe, G., M. Saatcioglu, 1989, "Hysteretic Shear Model for Reinforced Concrete Members", *American Society of Civil Engineering Journal of Structural Engineering*, Vol. 115, No. 1, pp. 132-148.

Panagiotou M., J.I. Restrepo, M. Schoettler and G. Kim, 2012, "Nonlinear Cyclic Truss Model for Reinforced Concrete Walls", *American Concrete Institute Structural Journal*, Vol. 109, No. 2, pp. 205-214.

Pang, D. and T.C. Hsu, 1995, "Behavior of Reinforced Concrete Membrane Elements in Shear", *American Concrete Institute Structural Journal*, Vol. 92, No. 6, pp. 665-677.

Pang, D. and T.C. Hsu, 1996, "Fixed Angle Softened Truss Model for Reinforced Concrete", *American Concrete Institute Structural Journal*, Vol. 93, No. 2, pp. 197-207.

Petrangeli, M., P.E. Pinto and V. Ciampi, 1999, "Fiber Element for Cyclic Bending and Shear of RC Structures I: Theory", *American Society of Civil Engineering Journal of Engineering Mechanics*, Vol. 125, No. 9, pp. 994-1001.

Saatcioglu M. and S.R. Razvi, 1992, "Strength and Ductility of Confined Concrete", *American Society of Civil Engineering Journal of Structural Engineering*, Vol. 118, No. 6, pp. 1590-1607.

Sayre, B., 2003, "Performance Evaluation of Steel Reinforced Shear Walls", M.S. Thesis, University of California.

Stevens, N.J., M. Uzumeri and M.P. Collins, 1991, "Reinforced Concrete Subjected to Reversed Cyclic Shear-Experiments and Constitutive Model", *American Concrete Institute Structural Journal*, Vol. 88, No. 2, pp. 135-146.

Takeda, T., M.A. Sozen and N.N. Nielsen, 1970, "Reinforced Concrete Response to Simulated Earthquakes", *American Society of Civil Engineering Journal of Structural Division*, Vol. 96, No. 12, pp. 2557-2573.

Terzioglu, T., 2011, *Experimental Evaluation Of The Lateral Load Behavior Of Squat Structural Walls*, MS. Thesis, Boğaziçi University.

Thermou G.E., V.K. Papanikolaou, A.J. Kappos, 2014, Flexural behaviour of reinforced concrete jacketed columns under reversed cyclic loading. Engineering Structures, Vol. 76, pp. 270-282.

Thomsen J.H. and J.W. Wallace, 1995, "Displacement-Based Design of Reinforced Concrete Structural Walls: An Experimental Investigation of Walls with Rectangular and T-Shaped Cross-Sections", *Department of Civil Engineering, Clarkson University*, Postdam, New York.

Thomsen, J.H. and J.W. Wallace, 2004, "Experimental Verification of Displacement-Based Design Procedures for Slender Reinforced Concrete Structural Walls", *American Society of Civil Engineering Journal of Structural Engineering*, Vol. 130, No. 4, pp. 618-630.

Tran T.A., 2012, "Experimental and Analytical Studies of Moderate Aspect Ratio Reinforced Concrete Structural Walls", Ph.D. Thesis, University of California, Los Angeles.

Tran T.A. and J.W. Wallace, 2012, "Experimental Study of Nonlinear Flexural and Shear Deformations of Reinforced Concrete Structural Walls", *Proceedings of the 15th World Conference on Earthquake Engineering*, Lisbon, Portugal.

Ulugtekin, D., 2010, "Analytical Modeling of Reinforced Concrete Panel Elements Under Reversed Cyclic Loadings", M.S. Thesis, Bogazici University.

Vecchio, F.J. and M.P. Collins, 1986, "The Modified Compression-Field Theory for

Reinforced Concrete Elements Subjected to Shear", *American Concrete Institute Structural Journal*, Vol. 83, No. 2, pp. 219-231.

Vecchio, F.J. and M.P. Collins, 1988, "Predicting the Response of Reinforced Concrete Beams Subjected to Shear Using Modified Compression Field Theory", *American Concrete Institute Structural Journal*, Vol. 85, No. 3, pp. 258-268.

Vecchio, F.J. and M.P. Collins, 1993, "Compression Response of Cracked Reinforced Concrete", *American Society of Civil Engineering Journal of Structural Engineering*, Vol. 83, No. 2, pp. 219-231.

Vintzeleou, E.N. and T.P. Tassios, 1987, "Behavior of Dowels Under Cyclic Deformations", *American Concrete Institute Structural Journal*, Vol. 84, No. 1, pp. 18-30.

Vintzeleou, E.N. and T.P. Tassios, 1987, "Concrete-to-Concrete Friction", *American Society of Civil Engineering Journal of Structural Engineering*, Vol. 113, No. 4.

Vulcano, A., V.V. Bertero and V. Colotti, 1988, "Analytical Modeling of RC Structural Walls", *Proceedings of 9th World Conference on Earthquake Engineering*, Vol. 6, pp. 41-46.

Xu, S.Y. and J. Zhang, 2010, "Hysteretic Shear-Flexure Interaction Model of Reinforced Concrete Columns for Seismic Response Assessment of Bridges", *Earthquake Engineering and Structural Dynamics*.

Yankelevsky, D.Z. and H.W. Reinhardt, 1987, "Response of Plain Concrete to Cyclic Tension", *American Concrete Institute Materials Journal*, Vol. 84, No. 5, pp. 365-373.